POLITECNICO DI MILANO

Facoltà di Ingegneria Civile, Ambientale e Territoriale

Corso di Laurea in Ingegneria Civile - Strutture

DIFFERENT TECHNIQUES TO ANALYZE WIND EFFECTS ON CORNER PRESSURES OF A MEDIUM-RISE BUILDING

Relatore (Tutor): Prof. Ing. Perotti Federico (Politecnico di Milano)

Correlatore : prof. Ing. Winam Suaris

Martino Carrettini 735380

Fabio Tradigo 735343

Academic year 2009-2010

1 INTRODUCTION 5

2 WIND PHENOMENON 8

2.1 The study of the wind 8

2.1.1 Mean wind velocity 11

2.1.2 Turbulence of the wind 14

2.1.3 Density of probability 17

2.1.4 Turbulence spctrum 18

2.1.5 Spatial correlation 21

2.1.6 Coherence 23

2.2 Conclusions 25

3 WIND LOADS 26

3.1 Physics phenomena 27

3.2 Streamlines and Bernoulli's Equation 29

3.3 Venturi Effect 31

3.4 Bluff and Streamlined Bodies – Pitot-Static Tube 31

3.5 Pressure and Force Coefficients 34

3.6 Two-dimensional force coefficients 36

3.7 Three-dimensional force coefficients 36

3.8 Reynolds Number and Surface Roughness Effects 37

3.9 Wind Axes and Body Axes 40

3.10 Mean wind effect 42

3.11 Mean and Fluctuating Pressure Coefficients 45

3.12 Mean Pressure Coefficients on Rectangular Buildings in Boundary Layer Flow 46

3.13 Definitions of Mean Force and Moment Coefficients 47

3.14 Drag Force Coefficient on Two-Dimensional Rectangular Prisms 48

4 TEST IN THE WIND TUNNEL 50

4.1 Wind-tunnel layouts 50

4.1.1 Open-circuit type 51
4.1.2 Closed-circuits type 52
4.1.3 Simulation of the natural wind flow 55
4.2 Experimental Set-up 57
4.2.1 The model 57
4.2.2 Wind Tunnel setup 65
4.2.3 Sampling time 69
4.3 Rotation 72
4.4 Pressure coefficients 74
4.4.1 Pressure coefficients C_p 74
4.4.2 Pressure coefficients GC_p 75
4.5 Cladding studies - measurements' problems 77
4.5.1 Tube Transfer Correction 78
4.5.2 Fisher Tippet correction 83
4.5.3 Fitting the Fisher Tippet Type I 88
4.6 Background 89
5 PARTICLE IMAGE VELOCIMETRY (PIV) ANALYSIS 94
5.1 Cross correlation (double frame / double exposure) 96
5.2 Test 96
5.3 Set Up 97
5.4 Calibration 98
5.5 Measurements 100
5.6 Analysis 102
6 COMPUTATIONAL WIND ENGINEERING 103
6.1 Introduction 103
6.2 Equations and theory of fluids 104
6.2.1 Mass conservation 105
6.2.2 Momentum conservation 106
6.2.3 Rate of change of Energy 108

6.2.4 Further hypothesis 108
6.2.5 Momentum equation 109
6.2.6 Shear stress term 110
6.2.7 Viscous effect 111
6.2.8 RANS Reynolds-Averaged Navier-Stokes equations 114
6.3 Turbulence models 117
6.3.1 Turbulence model: $\boldsymbol{k-\varepsilon}$ 117
6.3.2 RANS and $\boldsymbol{k-\varepsilon}$ 121
7 DATA ANALYSIS 124
7.1 Extreme values 124
7.2 Pressure level curves 127
7.3 Comparison with ASCE 131
7.4 C_l, C_d and C_m 139
8 CONCLUSIONS 149
9 APPENDIX A 151
10 APPENDIX B 161
11 BIBLIOGRAPHY 166

1 Introduction

The effect of wind on the structures is a very important topic to consider for building design. Even if in Italy for building design the effects of earthquakes is predominant even for high rise structures, the effects of wind have a big incidence for the project as during the construction period.

Nowadays in Italy wind effects are becoming more and more important with the new high constructions. In fact, wind speed increases with the distance from the ground and becomes a significant factor for the design. Taking as an example the new skyscraper "Palazzo Lombardia", its construction highlighted the importance of wind effects on structures, not only because of the dynamic forces generated by the wind, but also because of some post-construction problems when laying the claddings. The biggest problems have been identified in the leeward side of the building.

This one and many others important effects caused by the wind flow around structures will be explained in this thesis. Of course, the example of the "Palazzo Lombardia" does not mean that wind is the primary aspect of design, but it gives an idea of the incidence of wind related issues in the present structures, while in the common thought they are ignored because of the prevalence of seismic effects.

Generally speaking wind has two kind of effects on structures. The first effect is predominant on high buildings and is the dynamic response to wind variation in time. The second effect causes problems also on intermediate rise structures and is the variation of pressure on the claddings.

In literature many studies have been done on high rise buildings, both on cladding pressure and dynamic response. Some papers also compare experimental data with Computational Fluid Dynamic simulations. In the Bibliography they will be mentioned.

On the other hand, literature on intermediate high buildings is lacking, a part from some studies on the flow of the wind across classic geometries (like the cube). The limits to

classify a building like a medium rise building (or building of intermediate height) is 15 meters (50 feet or 60 like the ASCE said) and more than 35 meters (almost 120 feet). Above the low limit there are the low rise building and over the tall building.

Even in this case, anyway, research lacks of quantitative details, for example in monitoring pressure on the cladding. Moreover, it has to be noticed that in places like the American east coast, wind issues have to be considered also for low-intermediate rise structures because of the particular climate characterized by strong winds and hurricanes.

For those reasons this work focuses on intermediate rise buildings, characterized by really big flow separation at the edges and at the corner zones causing big suctions and air recirculations. Another important factor to be considered is that standard buildings always have classic shapes, which means that they have sharp edges that cause big flow separations. Moreover, many intermediate structures have a flat roof and cause big separation on the top of the building, too.

The present work have the purpose to study pressures and suctions on the edges, on the corner and on the roof zone of a cubic structure of intermediate height . The cubic shape is really helpful because it allows the use of symmetry. The model of the present work in full scale is a little bit higher than 30 meters.

This work presents at first an introduction on how it is possible to study the wind effects from a mathematical point of view, involving statistical analysis to model the unsteady behavior of the flow. It will be followed by a Chapter on the wind loads, that will also explain how the pressure coefficients (that are also used by the codes) are calculated.

For this thesis, the same problem has been considered from different point of view, using three different techniques. The first one is the most classic one and is explained in Chapter 4: the wind tunnel test. It allows to measure pressures on the cladding for a chosen wind profile. The second one is the so called PIV (Particle Image Velocimetry) in the Chapter 5: it is another test in a wind tunnel, but the measures are made thanks to

a high frequency camera and allows to calculate the wind speed for a chosen plane. At last, it is interesting to compare the previous results with a CFD test that was run with the aid of Fluent in Chapter 6.

At last the results from the three tests are put together to describe the wind flow and effects on the structure.

To introduce this problem it is important to make two fundamental observations. First the opportunity to access so many different instrument for research allows to have a better understanding of the problem and to validate the results from different point of view. Secondly the detail of the information from the wind tunnel is without precedent: 504 taps were placed on one octave of the structure and, rotating the model, allow to recreate the entire pressure pattern on the whole structure with a higher density on corners and edges.

2 Wind phenomenon

The study of wind behavior and the determination of its intensity is extremely complicated mainly because we are unable to represent physically the magnetic field.

Whereas for the representation of almost every load acting on the structure is possible to use vectors or distributed load, for wind is necessary to analyze it a priori.

Even the regulation code requests a precise description of wind strength considering its dependence on a large amount of parameters and statistically analyzing the collected data.

We will consider the horizontal load of wind on the vertical side structure; it is difficult to establish the feedback of a structure to this load due to the trouble in defining univocally the force for it is unknown in every time t.

The modal analysis and the dynamic's study of building requests the knowledge of the force and of its behavior in time. Those are the deterministic forces (periodic or non-periodic ones). In the appendix there is a statistical approach to the study of this kind of deterministic forces.

2.1 The study of the wind

We will now face the main characteristics of real turbulent wind. The complex wind behaviour requires a statistical explanation.

Wind is caused by a difference in atmospheric pressure. At great heights the air movement is not influenced by earth surface, whereas below a certain height, called delta gradient height (or boundary layer), surface's friction modifies wind flux, creating turbulence. The boundary layer changes according to the ground underneath. Approximately we suggest considering its value 300 meters on the ocean and 600

meters above towns (some studies suggest to put the level even higher, up to 1000 meters according to Jonh Holmes, for skyscrapers are growing higher and higher).

Time story of longitudinal speed is:

$$U(t) = \bar{U} + u(t)$$

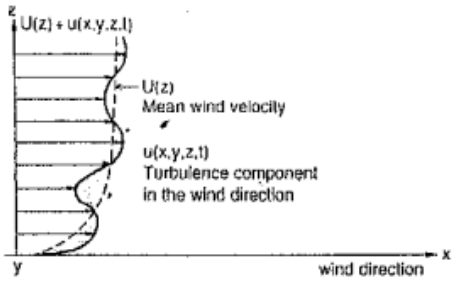

Figure 1 - Longitudinal speed

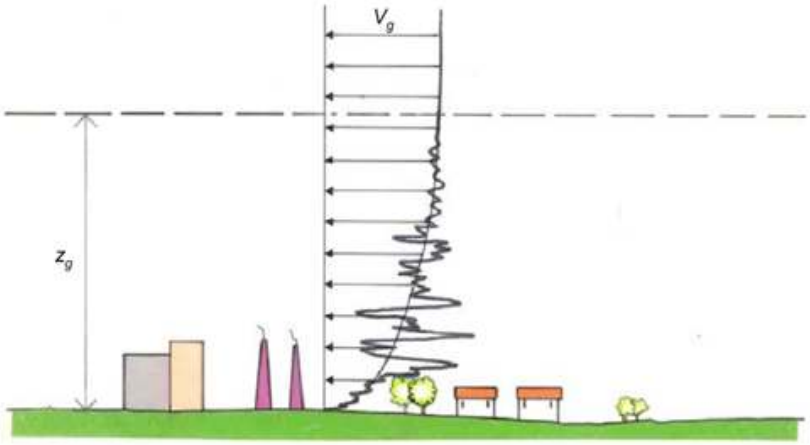

Figure 2 - Mean speed wind profile and atmospheric turbulence

The first term is the speed mean value on period that goes from 10 minutes to 1 hour according to the reference codes; the u(t) is the dynamic waving part, which causes the turbulence.

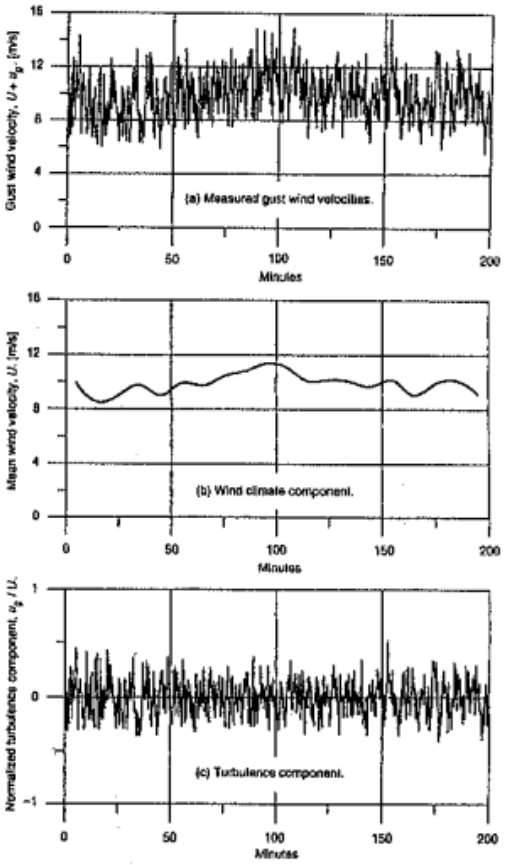

Figure 3 - Composition of the measured gust wind velocities

Such a distinction allows separating our study in two: the boundary layer is characterized by the mean speed in a way, and by a turbulence part, which can be added.

Furthermore real wind has a vertical and transversal component, but their mean value is none. A precise mathematical description, which uses a Cartesian system, requires the three directions together (longitudinal, transversal and vertical one):

$$U(x,y,z,t) = \overline{U}(z) + u(x,y,z,t)$$

$$V(x,y,z,t) = v(x,y,z,t)$$

$$W(x,y,z,t) = w(x,y,z,t)$$

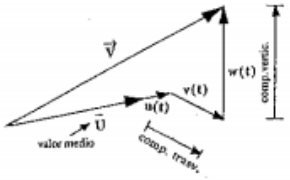

-

Figure 4 - Generic components of wind speed

We can therefore split wind behaviour into mean wind velocity, wind profile and wind turbulence.

2.1.1 Mean wind velocity

Il valor medio della velocità del vento dipende dall'altezza z a cui si misura la velocità stessa come mostra, per differenti tipi di terreno la figura. La figura riporta i risultati delle misurazioni comprensivi della parte turbolente: si nota ugualmente la dipendenza della media dall'altezza.

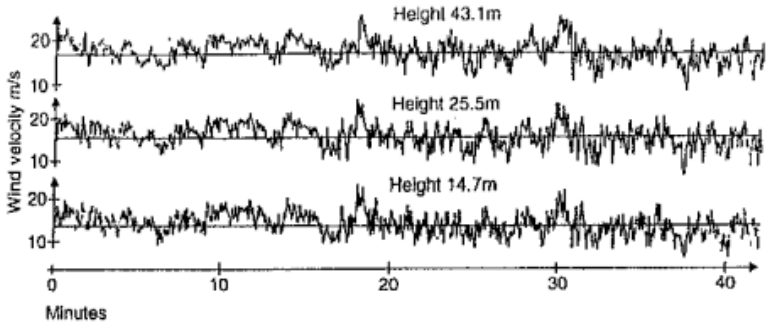

Figure 5 - Examples of wind speed measurements at different heights

Lo strato limite ha come grandezze decisive, la rugosità del terreno soprattutto nella parte bassa e l'altezza nella parte più prossima al libero regime di flusso. Matematicamente parlando la più accurata espressione matematica è la legge logaritmica ("logaritmic law"); essa a velocità maggiori si 20 m/s dà risultati corretti fino a 300 metri. I codici preferiscono introdurre l'andamento esponenziale (power law) che è risultato di studi empirici ed è comunque di più facile utilizzo. L'EC1 usa l'andamento logaritmico per altezze fino ai 200 m. Non ci soffermiamo sul calcolo dei parametri rugosità del terreno dei codici. Riportiamo per l'interesse la formulazione teorica più appropriata dell'andamento logaritmico del wind profile, (ottenuta per integrazione):

$$U(x,y,z,t) = \bar{U}(z) = \frac{u_*}{k} \ln \frac{z}{z_0}$$

$$u_* = \sqrt{\frac{\tau_0}{\rho}}$$

Dove tau0 è la sollecitazione tangenziale al livello della superficie, ro è la densità dell'aria, z0 è il parametro legato alla rugosità (altezza della rugosità) e k è la costante di Von Karman. La dipendenza dalla rugosità è evidente dalla seguente schematizzazione in figura.

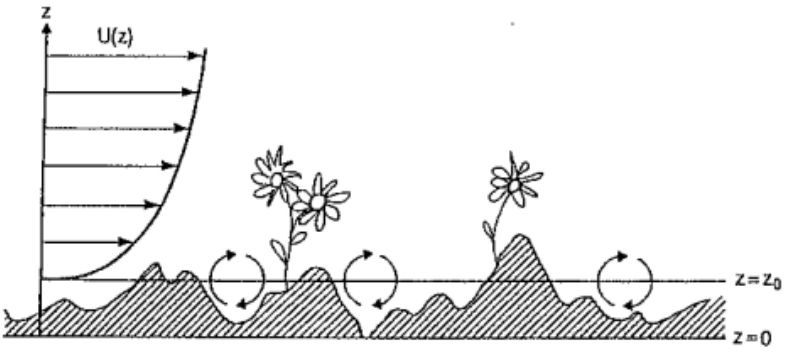

Figure 6 - Dependence on the roughness

U* è la cosiddetta velocità di frizione (friction velocity) che ha le dimensioni di una velocità, ma fisicamente non corrisponde a una velocità.

A titolo di esempio riportiamo l'Eurocodice 1 che si riferisce a tale espressione matematica per il profilo medio del vento (anche se poi per ogni zona riporta tramite tabelle i valori di riferimento).

La power law è invece la seguente e utilizzata dal codice canadese e americano.

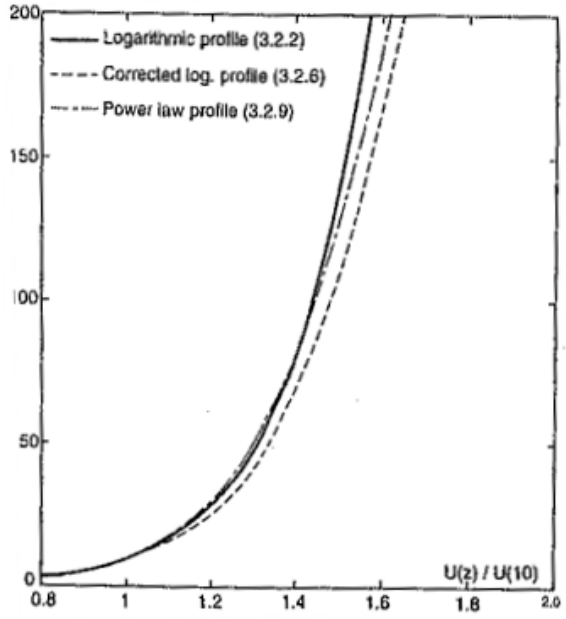

Figure 7 - Different functions to define wind profile

La variazione del valor medio della velocità, riportata nella figura, può essere espressa in funzione dell'altezza da una legge esponenziale del tipo:

$$\overline{U}(z) = \overline{U_g}\left(\frac{z}{z_g}\right)^{\alpha}$$

Essendo Ug la velocità media definita in corrispondenza dell'altezza gradiente zg=delta: il coefficiente alfa è funzione del tipo di terreno e è all'interno di un range di valori da 0.16 per zone in mare aperto a 0,40 all'interno di grandi città.

2.1.2 Turbulence of the wind

La figura mostra in maniera chiara la natura turbolenta del vento con alcune caratteristiche statistiche prima illustrate. Essa illustra una misurazione vicino al livello

superficiale del terreno con velocità modesta. È evidente come la velocità è tutt'altro fuorché ferma. Le quantità come la velocità media (già ampiamente trattata) e la RMS possono essere calcolate per la variabile random, cioè la turbolenza. Per quanto riguarda le equazioni del moto del fluido, esse cambiano tenendo conto della componente di turbolenza presente. In uno studio approfondito andranno tenute in conto.

La parte fluttuante, responsabile della turbolenza nello strato limite, è meno sensibile alla variazione con l'altezza ed è una grandezza random variabile sia nello spazio sia nel tempo. Le principali grandezze statistiche che caratterizzano le fluttuazioni della vena sono: l'intensità di turbolenza It, la densità di potenza spettrale Gv(f), la corss-correlazione tra velocità misurate in diversi punti dello spazio Rxy(csi) e la distribuzione di probabilità della velocità. Per essere preciso come è specificato nella descrizione matematica la parte turbolenta comprende tre componenti, u, v e w. Dovranno essere ricavate le tre deviazioni standard delle tre componenti. I risultati sperimentali di Davenport (1967), Harris (1970) e Armitt (1976) mostrano che le tre deviazioni standard decrescono con l'altezza molto piano fino all'altezza di ordinari edifici. Addirittura Armitt (1976) sostiene che esse sono quasi costanti fino a metà dell'altezza dello strato limite. Fino all'altezza di circa 100-200 metri sopra il terreno omogeneo, la deviazione standard delle tre componenti di turbolenza sono approssimativamente:

$$\sigma_u = Au_*$$

$$\sigma_v \approx 0.75\sigma_u$$

$$\sigma_w \approx 0.5\sigma_u$$

Dove A è una costante di valore 2.5 se z0=0.05 e A 1,8 se z0=0.3.

L'intensità di turbolenza It è definita come:

$$I_u = \frac{\sigma_u}{\bar{U}}$$

Essendo la sigma la deviazione standard della velocità della vena. Questa formula vale per tutte le tre dimensione, quindi longitudinale, laterale e verticale. Tenendo conto che sigma è riferito alla oscillazione intorno alla velocità media, quindi essa ha una media nulla ovviamente.

GRAFICI

L'indice It viene fatto normalmente dipendere dal coefficiente di drag del terreno k tramite la relazione:

$$I_t = \beta\sqrt{k}$$

Il cui valore k varia da un valore di 0,005 per terreni in mare aperto, fino a un valore di 0,05 per le aree centrali delle grosse città.

Il coefficiente beta per la componente per la componente orizzontale è normalmente pari a 2,45. L'indice di turbolenza reale varia tra il 5 e il 25%.

Utilizzando le forme fino ad adesso utilizzate, si può definire l'andamento dell'intensità di turbolenza:

$$I_u = \frac{\sigma_u}{\overline{U}} = \frac{2.5u_*}{\frac{u_*}{0.4}\ln\frac{z}{z_0}} = \frac{1}{\ln\frac{z}{z_0}}$$

In tal modo essa è semplicemente legata alla rugosità superficiale. Stesso ragionamento si può protrarre per le altre due direzioni, anche se di minore interesse.

Questo tipo di studio è assai importante perché nella simulazione che verrà effettuata nel test in galleria del vento e nella simulazione una parte iniziale sarà dedicata alla accurata descrizione delle modalità di simulazione del comportamento del vento anche per quel che riguarda il comportamento proprio del boundary layer, cioè la turbolenza. Per quanto riguarda la galleria del vento che è stata utilizzata, essa, diversamente da altre a disposizione della stessa Università di Miami, è in grado di studiare accuratamente lo strato limite e riprodurre le sue caratteristiche.

2.1.3 Density of probability

Come mostrato nella figura iniziale le variazioni del vento nello stato limite sono generalmente random e non si ripetono nel tempo. Esse sono causate da vortici che si creano e che fanno variare la effettiva velocità attorno al profilo medio prima identificato. La densità di probabilità è definita e le misurazioni hanno mostrato come le componenti della velocità del vento nello strato limite seguono la distribuzione normale Gaussiana (caratterizzata dal valor medio Usegnato e dalla deviazione standard sigmau. In tal modo conoscendo il valor medio e la deviazione standard la probabilità di ogni tipo di velocità del vento può essere stimata.

$$f_u(u) = \frac{1}{\sigma_u\sqrt{2\pi}} exp\left[-\frac{1}{2}\left(\frac{u-\overline{U}}{\sigma_u}\right)^2\right]$$

Tale studio descrive la grandezza del fenomeno ventoso, ma niente su come velocemente o lentamente esso varia nel tempo. Per descrivere la distribuzione della turbolenza con la frequenza, si utilizza la densità di potenza spettrale o semplicemente spettro.

In molti codici, tra cui quello americano, per i carichi da vento, è utilizzata la peak gust wind speed, cioè la velocità di picco dovuta alle raffiche da vento. Tenendo conto delle premesse di variabile random, si può però valutare approssimativamente il valore, considerando la distribuzione gaussiano delle velocità.

$$\hat{U} = \overline{U} + g\sigma_u$$

Dove g è il peak factor pari a 3,5.

Più interessante e più usato è invece il gust factor, G, cioè il rapporto tra la massima velocità di raffica in un periodo specificato e la velocità media del vento.

$$G = \frac{\widehat{U}}{\overline{U}}$$

Assegnare un valore fisso a tale coefficiente non è facile; diversi studi sperimentali sono stati fatti e a seconda della zona ovviamente si trovavano valori differenti. Deacon per altezza 10 metri, basata su la velocità media di 10 minuti, ha trovati valori di 1.45 per terreni in aperta campagna e 1,96 in città.

Ovviamente in caso di uragani e tempeste tropicale tale valore è destinato a crescere. Più autori utilizzando diverse formulazioni l'hanno legato alla intensità di turbolenza. Soprattutto per quanto riguarda lo studio dei carichi da vento il codice americano fa riferimento a dei coefficienti di pressione, come sarà chiaro nel seguito, non spuri, ma considerando tale effetto di picco, nella fase di progetto. Non saranno i Cp come per l'Eurocodice, ma piuttosto i GCp.

2.1.4 Turbulence spctrum

L'energia associata alle fluttuazioni della vena è distribuita su un ampio campo di frequenze: tale distribuzione in funzione della frequenza viene descritta attraverso la funzione "densità di potenza spettrale" Gv(f) che, ricordiamo, è correlata alla varianza attraverso la relazione:

$$\int_0^{+\infty} G_v(f)df = \sigma^2$$

Spesso tale funzione viene rappresentata in forma adimensionale, come mostra la figura, dove:

f è la frequenza in Hz,

sigma quadro la varianza, ricavabile dall'indice di turbolenza tramite la formula vista prima (ossia dal tipo di terreno),

delta è l'altezza gradiente (funzione anch'essa del tipo di terreno)

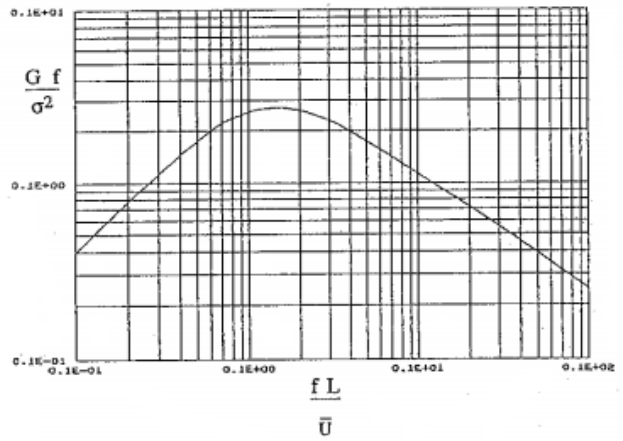

Figure 8 - Power spectrum density of the wind

Il rapporto frequenza e velocità media viene definito come inverso della lunghezza d'onda, associata alle dimensioni dei vortici atmosferici. Tale lunghezza può essere poi rapportata a una dimensione caratteristica, detta scala integrale L, definita come la lunghezza d'onda dei vortici in corrispondenza del picco dello spettro (tale grandezza viene anche definita come baricentro dell'autocorrelazione): normalmente L è dell'ordine del centinaio di metri.

È possibile in tal modo definire una frequenza adimensionale (detto anche numero di Stroudhal o frequenza ridotta):

$$\bar{f} = \frac{fL}{\bar{U}}$$

Il numero di Stroudhal è utilizzato per valutare la vibrazione per quanto riguarda il distaccamento dei vortici. Infatti ns, la frequenza del distaccamento dei vortici, è proporzionale alla frequenza del vento che soffia, e inversamente proporzionale alla profondità del corpo (St=nsb/Usegnato).

Ovviamente tale relazione può essere specificate per tutte le direzioni come già prima è stato fatto:

$$\int_0^{+\infty} S_v(f)df = \sigma^2{}_u$$

$$\int_0^{+\infty} S_v(f)df = \sigma^2{}_v$$

$$\int_0^{+\infty} S_w(f)df = \sigma^2{}_w$$

La funzione di densità di potenza spettrale Gv(f)=Gv(fsegnato) viene ricavata, attraverso la misura del vento, con le metodologie definite nel paragrafo precedente ed è possibile interpolare la stessa tramite una formula detta di Von Karman:

$$G(\bar{f}) = 4k\overline{U}\frac{\frac{L}{\overline{U}}}{\left(2+\bar{f}^2\right)^{\frac{5}{6}}}$$

Dove fsegnato è la frequenza adimensionale, Usegnato è il valor medio della velocità (m/s) e L la scala integrale (m).

In letteratura sono presenti variabili di tale formula di Von Karman con coefficienti differenti, ma di identica forma; questo perché, evitando di entrare nel dettaglio della trattazione teorica, si tratta di un comportamento asintotico dello spettro della densità. Harris ha riportato al caso del vento gli studi di Von Karman e a queste formulazioni faremo riferimento. Inoltre Davenport, Busch and Panofsky, Kaimal, Simiu e Scanlan e altri hanno analizzato e testato questo problema:

$$\frac{fS_u}{\sigma^2{}_u} = \frac{4\frac{fl_u}{\overline{U}}}{\left[1+70.78\left(\frac{fl_u}{\overline{U}}\right)^2\right]^{\frac{5}{6}}}$$

Riportiamo solo lo spettro della velocità longitudinale perché gli altri sono meno interessanti per quanto riguarda il problema che andremo a studiare. Per esempio per strutture orizzontali quali i ponti la componente verticale gioca un ruolo importante.

La figura seguente mostra diverse soluzioni presenti in letteratura per quanto riguarda lo spettro di densità di frequenza della componente turbolenta dell'azione ventosa.

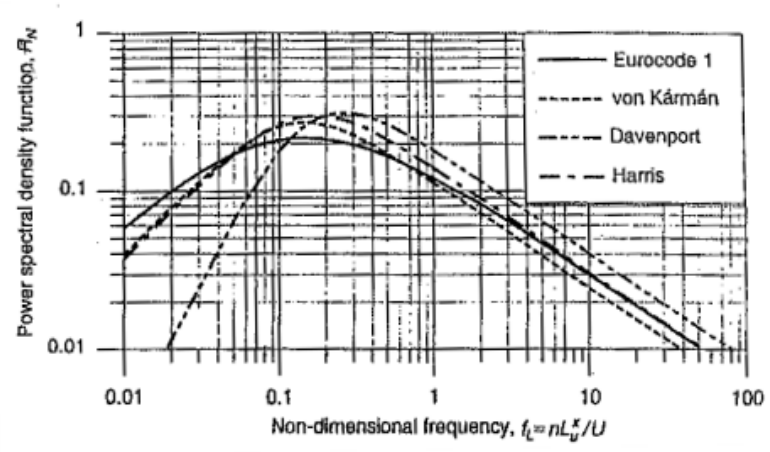

Figure 9 - Frequency spectrum density of the turbulent component of the wind

2.1.5 Spatial correlation

La correlazione spaziale delle velocità del vento misurate in due differenti punti "x" e "y" è descritta dalla funzione di coerenza:

$$\gamma^2{}_{xy}(f) = \frac{\left|G_{yx}(f)\right|^2}{G_{xx}(f)G_{yy}(f)} \, con \; 0 \leq \gamma^2{}_{xy}(f) \leq 1$$

Dove Gxy è il cross-spettro e Gxx e Gyy sono la densità di potenza spettrale Gv ricavate, come già spiegato, dai segnali dei due punti di misura attraverso la trasformata di Fourier della auto e cross-correlazione.

Se per esempio considero la velocità del vento a due differenti punti di una torre (misurazioni x e y), posso determinarne senza difficoltà la covarianza; con essa poi posso tramite la relazione soprascritta calcolare la correlazione tra le due misurazioni. A questo punto la correlazione potrà essere piena se le due altezze sono le stesse.

A titolo di esempio, nella figura, si riporta la funzione di autocorrelazione Rxx(tau) valutata a partire da una generica storia temporale della velocità del vento misurata da un anemometro. L'andamento caratteristico dell'autocorrelazione Rxx(tau) mostra chiaramente (si veda a titolo chiarificatore, gli esempi riportati nella parte precedente (paragrafo e figura)) come il fenomeno della turbolenza del vento sia caratterizzato da una banda larga di frequenze. Nella figura si riporta invece la funzione di cross-correlazione Rxy(tau) relativa alla velocità del vento misurata in due punti posti a una distanza tale per cui le due storie risultano poco correlate.

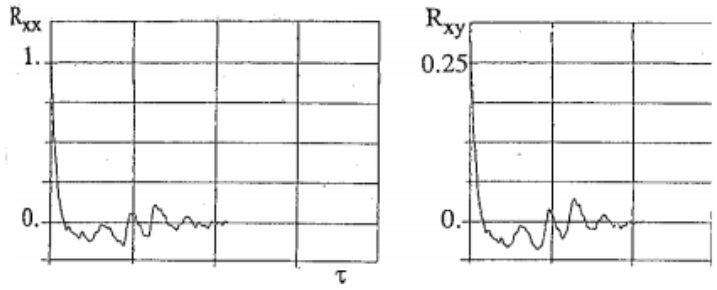

Figure 10 – Auto and Cross-correlation function

Covarianza e correlazione sono molto utili nel calcolo delle fluttuazioni di carico soprattutto per quanto riguarda gli edifici alti e lo studio delle coperture

2.1.6 Coherence

La funzione di coerenza dipende dal parametro (fdx/Usegnato) essendo delta x la distanza tra i due punti e Usegnato la velocità media: un'approssimazione adeguata a rappresentare tale funzione può essere la seguente:

$$\gamma^2{}_{xy}(f) = e^{-C\left(\frac{f\Delta x}{\bar{U}}\right)}$$

Essendo C una costante (C=7 per la componente verticale della turbolenza, C=15 per la componente orizzontale).

A differenza della precedente tale funzione ha a che vedere con le frequenze; soprattutto per quanto riguarda la correlazione delle fluttuazioni della velocità del vento di due punti posti a una differente frequenza. È una sorta di correlazione dipendente dalla frequenza.

Nella figura si riporta l'andamento della funzione di coerenza in funzione della frequenza adimensionalizzata (delta/usegnato): come si può notare, a parità di frequenza f e di valor medio Usegnato, la coerenza diminuisce all'aumentare della distanza deltax tra due punti di misura; gamma quadroxy(f) aumenta invece all'aumentare del valor medio Usegnato, mentre diminuisce all'aumentare della frequenza f (ossia al diminuire delle dimensioni del vortice associato a tale frequenza).

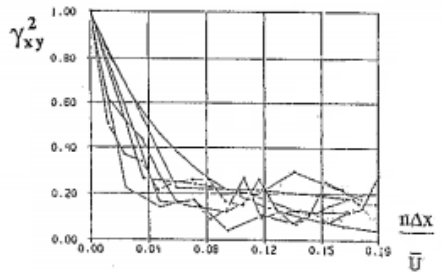

Figure 11 – Coherence function

Non è interesse di questa tesi calcolare la risposta dinamica di una struttura al vento turbolento, dato che la rigidezza che prendiamo ipoteticamente è infinita. Lo studio statistico fin qui fatto del comportamento del vento permette di proseguire con il calcolo delle sollecitazioni a cui la struttura rigida che andiamo ad analizzare è soggetta. Tale calcolo fin qui mostrato avrà delle ripercussioni sulla misurazione delle pressioni.

2.2 Conclusions

Lo studio statistico dell'azione del vento proseguirà nel seguito per quanto riguarda il trattamento dei dati nella galleria del vento. Ma l'obiettivo di questo capitolo era di dare una trattazione analitica, teorica e reale di quel fenomeno complesso che è il vento. Interessante capire come nella fase di input nel software saranno create le condizioni di boundary layer, così come nella galleria del vento stessa.

3 Wind loads

Wind acts dynamic forces on the overall building, and localized aerodynamic forces on each single element of the building, structural or not. These forces depend on the shape, dimension and orientation of the building and its elements with respect to wind direction. Moreover these force are strictly related to the Reynolds number and surface roughness, especially for those buildings or parts of with rounded surfaces.

With respect to a general theoretical study that will be exposed later, the pressures that will be taken into account are these we will take into account peak pressures referred to wind's most unfavorable direction. Nevertheless, some analysis related to the mean wind behavior using code's coefficients for design use will be done too. The local aerodynamic forces acted by the wind on single elements, both structural and not structural, which are part of the building, are evaluated considering those directions which, among all wind directions, cause the most intense forces. Those forces are often much greater than those applied to single elements in order to evaluate the overall wind action on the building, especially near edges and corners. Local aerodynamic forces must never be added to overall aerodynamic forces.

To summarize the practical protocol used, with respect to the European code (the same could be done for the US ASCE code), we could say that the study of the wind force is mainly evaluated referring to surface pressures. Moreover, codes also tell coefficient for concentrated momentum and forces, which can be used for "pre-designing", especially in a preliminary step. In the final stage of the project, computing and sizing of each element (both structural and not structural) require to use those pressures. The pressures' study, after all the statistical analysis of wind, is necessary in order to evaluate the forces actually stressing on. Nevertheless, the study we are about to develop has a notable structural implication, even though we are going through an analytical and theoretical approach.

We call peak aerodynamic forces on the building (object of our work), the expected values of the maximum wind (both overall and singularly) forces, evaluated over a time interval T=10 minutes, ignoring the reducing effects due to the different time distribution between peak local pressures and structural vibrations' amplifying effects. These forces are proportional to peak wind kinetic pressure, according to different laws related to different cases. A brief description of wind loads will follow, which is necessary to understand the successive analysis of test data.

3.1 Physics phenomena

Commento [F1]: phenomenon

We consider a fixed and unshrinkable body into the wind flow. Two linked effects could be noticed: on one hand the body modifies the flow changing the local configuration; on the other hand, on body's surface there is a pressure P, different from static pressure P_0, which is the pressure of the undisturbed flow. Thus there is an aerodynamic action, linked to the variation of the pressure on the surface, $P = P - P_0$ and these pressures act directly on the surface of the body. The description of the physic phenomenon change with the characteristics of the flow: it could be a three-dimensional flow or, in external zone, it is possible to use a bi-dimensional flow (in cross-section plane).

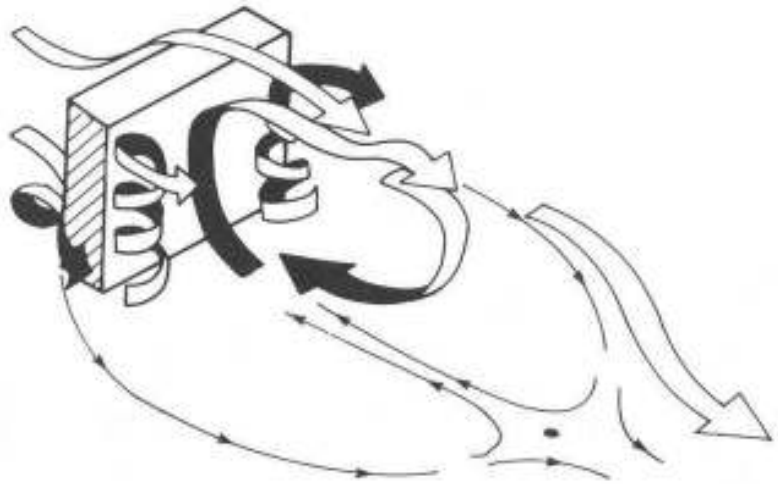

Figure 12 - Wind flow on a 3D body

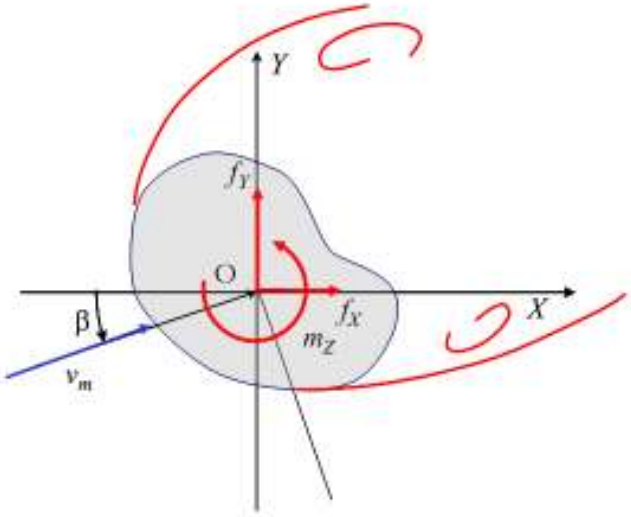

Figure 13 - Wind flow on a 2D body

In both the situations, on body's surface exposed to the incident flow, there is a thin boundary layer with a laminar or turbulent nature, depending on Reynolds number and on the superficial roughness of the building.

We try to describe physically how the wind loads are and the reason of them, in order to know how is the link between the wind characteristics and the pressures values.

3.2 Streamlines and Bernoulli's Equation

A streamline is a line that is parallel to the local velocity vector. The following figure (Figure 14 - Streamlines and Stream Tube) shows two streamlines in a two dimensional flow, the space between them being called a stream tube. At location 1 the cross-sectional area of the stream tube is A_1 and at location 2 it is A_2. The velocities at locations 1 and 2 are respectively U_1 and U_2, and the pressures are P_1 and P_2.

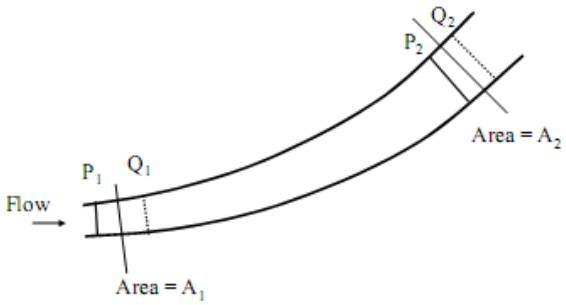

Figure 14 - Streamlines and Stream Tube

In wind engineering applications the air may be treated as incompressible. So we know that if a small volume $dV = P_1 Q_1 A_1$ of air crosses the line at location 1, since by

definition there is no flow across the streamlines, an equal volume must pass out across the line at location 2. Hence

$$P_1 Q_1 A_1 = P_2 Q_2 A_2 = dV \qquad (1)$$

The small amount of work done on pushing the elemental volume of air through the stream tube is

$$dW = (p_1 - p_2)dV \quad (2)$$

Also the kinetic energy dE_1 entering the stream tube at location 1 is

$$dE_1 = \frac{1}{2}\rho {U_1}^2 dV \qquad (3)$$

where ρ = air density, while that leaving at location 2 is

$$dE_2 = \frac{1}{2}\rho {U_2}^2 dV \qquad (4)$$

Therefore the change in kinetic energy between stations 1 and 2 is

$$dE = \frac{1}{2}\rho({U_2}^2 - {U_1}^2)dV \qquad (5)$$

But, by the principle of the conservation of energy,

$$dE = dW \qquad (6)$$

Therefore, from Equations 2 and 5

$$p_1 + \frac{1}{2}\rho {U_1}^2 = p_2 + \frac{1}{2}\rho {U_2}^2 \quad (7)$$

Note that since the locations 1 and 2 are arbitrary, Equation 7 applies anywhere along a streamline and may be stated as

$$p_1 + \frac{1}{2}\rho U^2 = costant\ along\ a\ streamline = H \quad (8)$$

This is Bernoulli's Theorem, as applied to flow without any "body" forces (i.e. no externally applied forces on the air particles themselves). What it tells us is that if the flow velocity goes up then the local pressure must go down. The constant in Equation 8 is often called the total pressure or total head, H.

3.3 Venturi Effect

The continuity equation, which follows from the law of conservation of mass implies that the rate of inflow of mass across location 1 in Figure 14 equals the rate of outflow at location 2. Hence

$$\rho U_1 A_1 = \rho U_2 A_2$$

or

$$\frac{U_2}{U_1} = \frac{A_1}{A_2} \qquad (9)$$

Therefore if $\frac{A_1}{A_2} > 1$, i.e. the streamlines become closer to each other at location 2, then the velocity at location 2 must increase compared with that at location 1.

Thus, if the airflow is forced between two obstacles, as depicted in Figure 15, and the streamlines are squeezed together, this results in an increased flow velocity and a lowering of the pressure between the two obstacles.

3.4 Bluff and Streamlined Bodies – Pitot-Static Tube

The flow depicted in Figure 15 is that around a pair of bluff bodies. The flow is unable to stay attached to the body around the sharp corners and so separates. The flow within the separated region is highly turbulent, as is the wake downstream of the bodies.

Figure 16 illustrates the flow around a very streamlined body (an airfoil). The streamlines stay attached the body and there is no flow separation. The only turbulence

generated by the body is confined to a very thin layer near the surface, the surface boundary layer.

For both bluff bodies and streamlined shapes the flow outside the turbulent regions is effectively inviscid, meaning that the effects of viscosity are negligible. In the inviscid flow regions Bernoulli's equation applies, i.e. Equation 8. Assuming the oncoming flow has uniform velocity then outside of the influence of the bodies the total pressure or total head H is everywhere the same. Where the flow comes to a complete halt on the front face of each body the velocity U is zero and so the pressure at that point becomes

$$P_{stagnation} = H \qquad (10)$$

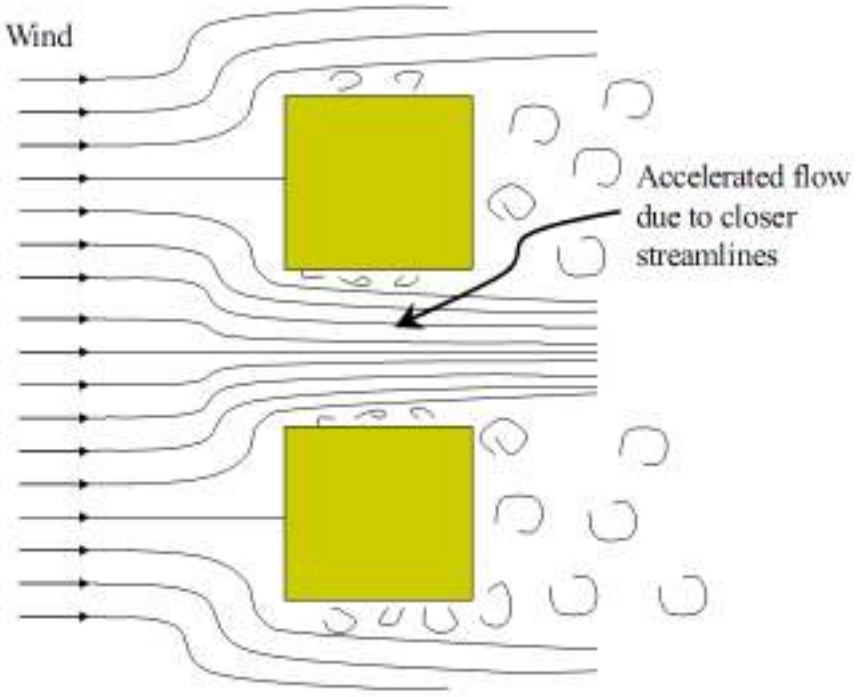

Figure 15 - Venturi Effect and Bluff Bodies

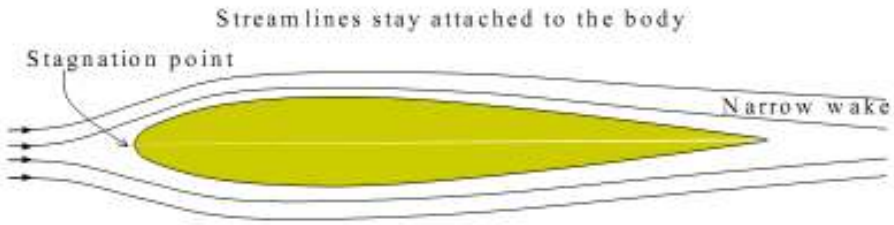

Figure 16 - Streamlined Body

The principle of the Pitot Static tube, (Figure 17), for measuring wind velocity is based on Bernoulli's equation. The open end of the tube faces into the wind and, since the flow comes to a complete halt inside the open end, it registers the total pressure H. The pressure from the open end is transmitted by an internal passage and additional tubing to one side of a pressure transducer, which is a device for measuring pressure differences.

On the side of the Pitot Static tube is another pressure tap that registers the static pressure p and this tap is connected to the other side of the pressure transducer. With the aid of Bernoulli's equation the wind velocity U is then calculated from the measured difference between these two pressures.

$$\frac{1}{2}\rho U^2 = H - p$$

$$U = \sqrt{\frac{H-p}{\frac{1}{2}\rho}} \qquad (11)$$

The quantity $\frac{1}{2}\rho U^2$ is called the dynamic pressure of the wind.

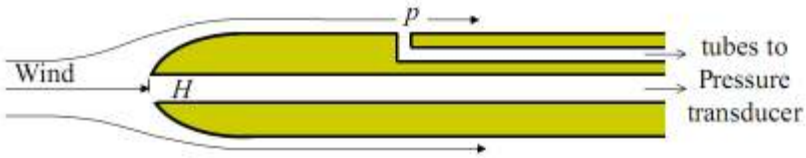

Figure 17 - Pitot-Static Tube

In the test this one will be the technology we use to calculate dynamic pressure and according to the devices of the wind tunnel we will have two Pitot tubes. This is very useful because, as will be clarified in the next paragraphs, the dynamic pressure is necessary to calculate the pressure coefficients, allowing to compare different situation and obviously all the codes refer to these coefficients.

3.5 Pressure and Force Coefficients

As discussed earlier, the effects of Reynolds number differences on flow patterns are in many situations negligible. In these situations, when a pressure difference, $p - p_0$, between the pressure on the surface of a body and the free stream static pressures, as depicted in Figure 17, is measured it will be proportional to the dynamic pressure $\frac{1}{2}\rho U^2$ of the wind in the free stream. If you double the dynamic pressure you simply double $p - p_0$. Thus a useful key parameter to measure is the pressure coefficient

$$C_p = \frac{p-p_0}{\frac{1}{2}\rho {U_0}^2} \quad (12)$$

Once C_p has been measured at one speed, in the absence of Reynolds number effects, the same value can be assumed to apply to all other speeds.

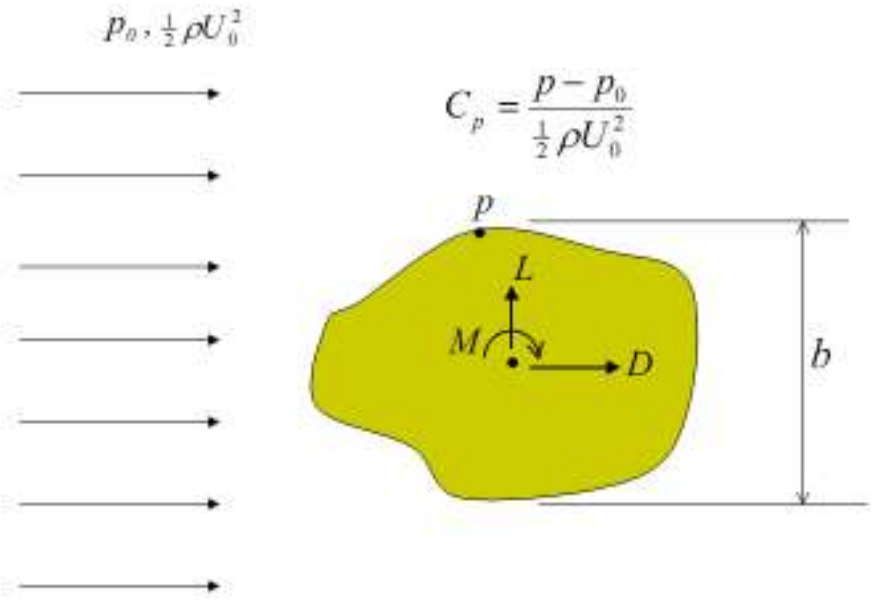

Figure 18 - Pressure Coefficient, Cp, on a Body, and Aerodynamic Forces and Moment

Integration of the complete pressure distribution over the surface of the body will give the overall aerodynamic forces and moments on the body. For a two dimensional body, such as shown in Figure 18 there will be a drag force D, a crosswind (or lift) force L, and a pitching moment, M, per unit length of the body. If the pressure coefficient at each point of the body's surface is proportional to the dynamic pressure of the wind, then so will be the aerodynamic forces and moment per unit length. Therefore it is convenient to express the aerodynamic forces in the form of non-dimensional coefficients, just as we did for the pressure. If the body is two dimensional as in Figure 18 then the forces will also be proportional to the size, or width dimension, b, of the body. Therefore the forces and moment per unit length are expressed in non-dimensional form as follows.

3.6 Two-dimensional force coefficients

Drag coefficient:

$$C_D = \frac{D}{\frac{1}{2}\rho {U_0}^2 b} \qquad (13)$$

Lift coefficient:

$$C_L = \frac{L}{\frac{1}{2}\rho {U_0}^2 b} \qquad (14)$$

Moment coefficient:

$$C_M = \frac{M}{\frac{1}{2}\rho {U_0}^2 b^2} \qquad (15)$$

If the body is three-dimensional and D, L and M are now defined as total forces and total moment on the body then the forces become proportional to the area of the body, rather than the length dimension, and the moment becomes proportional to the length dimension as well as the area. Thus for a three dimensional body we have 3-dimensional force coefficients

.

3.7 Three-dimensional force coefficients

Drag coefficient:

$$C_D = \frac{D}{\frac{1}{2}\rho {U_0}^2 A} \qquad (16)$$

Lift coefficient:

$$C_L = \frac{L}{\frac{1}{2}\rho {U_0}^2 A} \qquad (17)$$

Moment coefficient:

$$C_M = \frac{M}{\frac{1}{2}\rho {U_0}^2 Ab} \qquad (18)$$

where A is a reference area for the body, e.g. area in elevation or area in plan. In three dimensions the "lift" coefficient could refer either to a horizontal force or a vertical force, in both cases the force being normal to the wind direction. Likewise, the moment coefficient could correspond to a "rolling" moment about an axis aligned with the wind, or a "pitching" or "yawing" moment about the horizontal and vertical axes, respectively, normal to the wind direction.

3.8 Reynolds Number and Surface Roughness Effects

It has been mentioned that the usefulness in pressure, force and moment coefficients as defined above lies in the fact that for many situations the airflow behavior is insensitive to Reynolds number, $Re \equiv \frac{Ub}{v}$ where v = kinematic viscosity of air. Therefore the coefficients are independent of wind speed and the size of the body. With respect to scale model tests in a wind tunnel, this is very useful since the coefficients on the model are the same as full scale even though the model is vastly different in size and the wind speed in the wind tunnel may be very different from full scale.

For prismatic shapes with sharp edges, the assumption of Reynolds number insensitivity is valid over a wide range of Reynolds numbers from about 10^4 and higher. However, for shapes with curved surfaces like a circular cylinder the flow behavior can depend on Reynolds number. Figure 19 shows a plot of drag coefficient of a circular cylinder versus Reynolds number, with b set equal to the diameter. Focusing on the curve for the smooth surfaced cylinder, it can be seen that it shows a constant drag coefficient equal to about 1.2 up for Reynolds numbers up to about Re = 2 x 10^5 but then it drops precipitously to a value less than 0.4 at Re = 5 x 10^5. For Re above 5 x 10^5 the drag coefficient gradually climbs again, reaching a value of about 0.7 at very high Reynolds numbers.

The sudden drop in drag coefficient at the critical Reynolds number of 2 x 10^5 is connected with the behavior of the boundary layer on the surface of the cylinder. Close to the surface a boundary layer forms, starting from the stagnation point on the front.

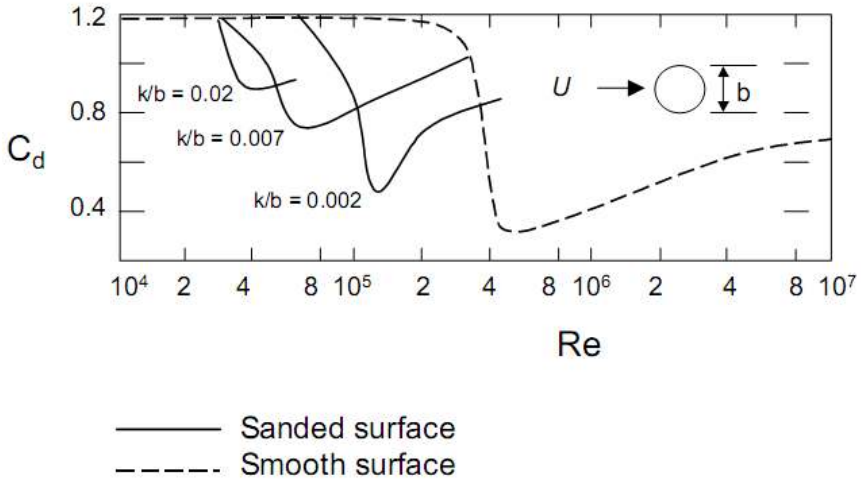

Figure 19 - Effect of Reynolds number and surface roughness on drag coefficient

The flow in the boundary layer is initially laminar, i.e. has no turbulence in it, and at Reynolds numbers below remains laminar until it has traversed to about the 90 degree angle around the circumference, see Figure 20. At that point the pressure gradient on the surface changes from positive to negative and the laminar boundary layer has difficulty flowing into the positive pressure gradient without separating. Therefore flow separation occurs at about the 90 degree point, see Figure 20. In the case of supercritical Reynolds numbers, i.e. above, the boundary layer on the cylinder transitions to turbulence before reaching the change in pressure gradient. Turbulent boundary layers are much more efficient at replenishing the momentum close to the surface than laminar

boundary layers, and so separation is delayed until further round the circumference, Figure 20. The result is that the wake at supercritical Reynolds numbers is narrower than at subcritical and the drag is less.

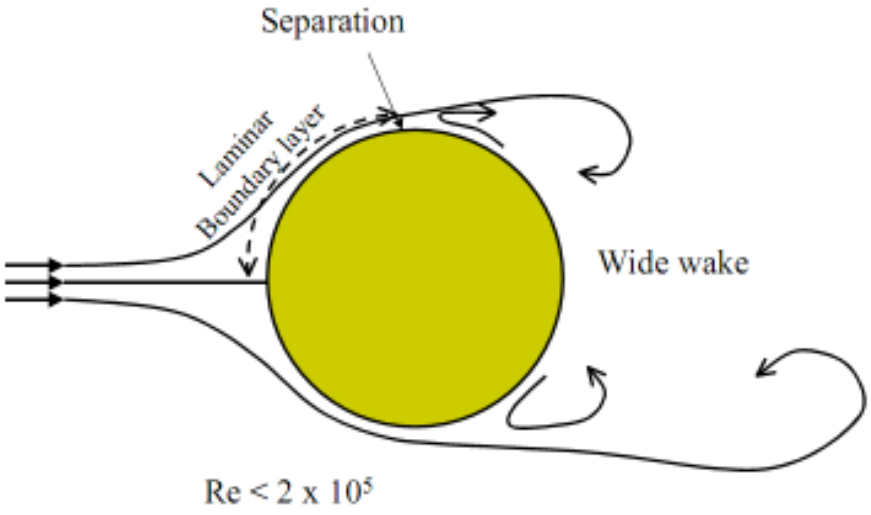

Figure 20 - Flow around circular cylinder at sub-critical Reynolds number

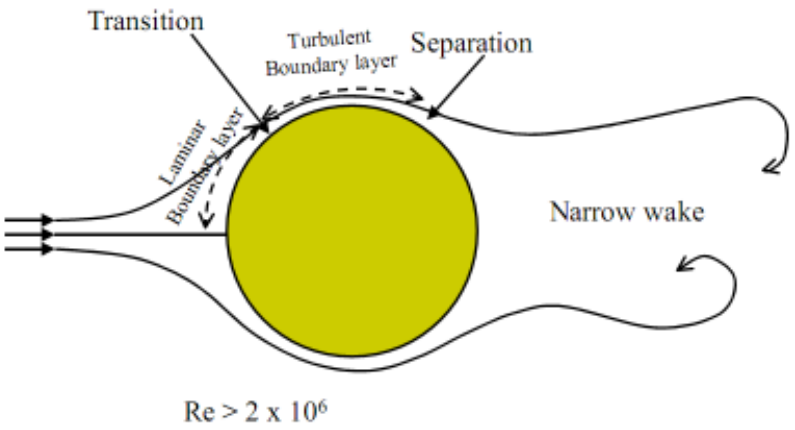

Figure 21 - Flow around circular cylinder at supercritical Reynolds number

Figure 21 also shows the effect of surface roughness on the drag of the circular cylinder. The roughness height is k and the results are shown for various values of k/b. It can be seen that the effect of roughness is to reduce the critical Reynolds number and also to reduce the drop in drag coefficient at the critical Reynolds number. Again, this is explainable in terms of the boundary layer development. The presence of the roughness triggers earlier boundary layer transition from laminar to turbulent. This initially allows the boundary layer to negotiate the positive pressure gradient further round the circumference but the roughness does reduce the ability of the turbulent boundary layer to resist separation. Therefore the flow still separates and does not go as far around the cylinder as for the smooth case at $Re = 2 \times 10^5$.

3.9 Wind Axes and Body Axes

Frequently the axis system that is convenient for wind loading on a structure is linked closely to the structure's geometry, whereas the axis system for the wind itself is more

conveniently aligned so that one axis, the x axis usually, is in the direction of the mean wind velocity. Figure 22 shows the difference between wind axes and body axes for a square building for which the chosen body axes are aligned with the sides, with the wind direction at an angle α relative to the body axes. Figure 22 shows the geometric relationship between the forces in the body axes and the lift and drag forces (which are aligned normal to and with the wind direction). From the geometric relationships depicted in Figure 23 it can be deduced that

$$F_x = Dcos\alpha - Lsin\alpha \qquad (19a)$$

$$F_y = Dsin\alpha + Lcos\alpha \qquad (19b)$$

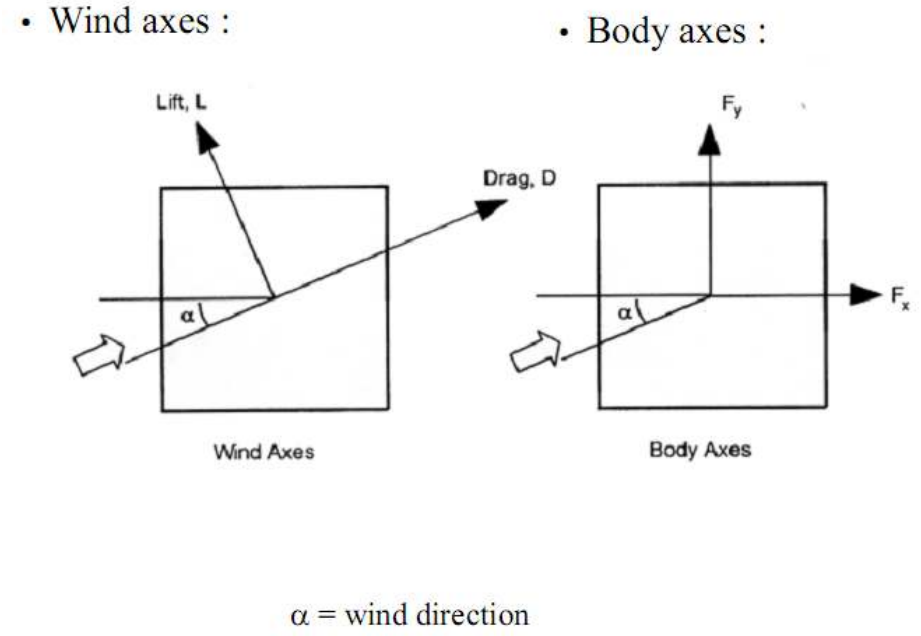

Figure 22 - Wind and Body Axis Systems

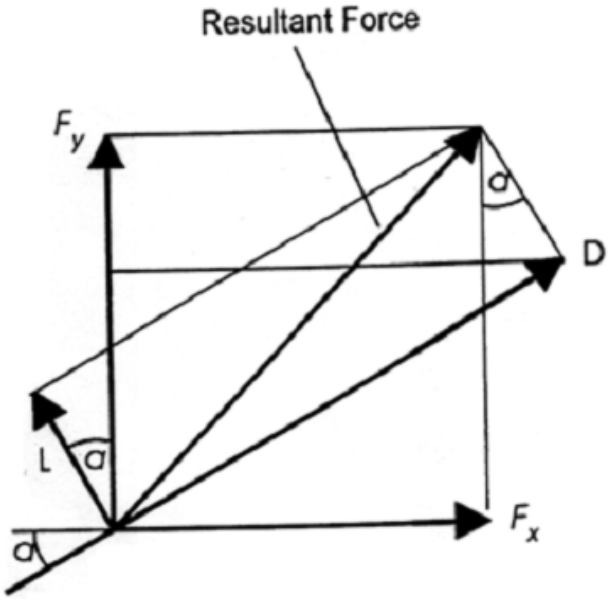

Figure 23 - Relationship Between Wind and Body Axis Forces

3.10 Mean wind effect

So far we defined pressure and force coefficients. These parameters are used extensively in building codes and standards as a means of determining wind loads on structures and are primarily determined through wind tunnel tests. The description in the previous paragraph was for the situation where the body or structure was in a smooth uniform stream of air. However buildings are located in the planetary boundary layer, which is highly turbulent and has a velocity that increases with height. In the early years of wind engineering the tendency was to ignore the effects of the planetary boundary and to treat buildings as though they were in smooth uniform flows, i.e. the wind tunnel tests were done in smooth uniform flow. However, in 1958 Jensen1 recognized the importance of the planetary boundary layer and found that the pressure distributions could be significantly different from those in smooth uniform flow.

Close to the ground, i.e. for low-rise buildings, all the properties of the wind tend to be largely dictated by the roughness length (witness the logarithmic mean velocity profile, the constant shear stress and its relation to the turbulence intensities, all of which are dominated by z_0). Therefore he proposed that to obtain the correct coefficients it was necessary to simulate the terrain roughness in the wind tunnel and that this could be done by matching the ratio $\frac{H}{z_0}$ to the full-scale value using appropriate roughness in the wind tunnel.

More generally the pressure and force coefficients on large structures will be influenced by a variety of factors, particularly if the terrain is non-uniform. Adopting the methods of dimensional analysis, we expect the exterior pressures on a rigid building of a given shape for a given wind direction to be a function of

- Reference mean wind speed U_{ref}
- Building dimension H
- The position coordinates on the building surface x, y, z
- RMS Turbulence velocity σ_u
- Air densityρ
- The integral scale of turbulence L_u
- Wind speed profile $\frac{U}{U_{ref}}$
- Kinematic viscosity ν
- Surface roughness length z_0

In the list of variables, we have used L_u as a surrogate for the complete power spectrum S_u on the assumption that the general shape of the spectrum can be made the same as at full scale, so that the main remaining task is to ensure the scale of the eddies is correct in relation to the wind tunnel model. In this list there are 12 nominally independent variables, including the position coordinates (x, y, z), and the Pi Theorem of dimensional analysis states that since we have three fundamental units (mass, length and

time), there should be 9 (i.e. 12 – 3) non-dimensional quantities to describe the problem. We know that the pressure coefficient is one,

$$\frac{p - p_0}{\frac{1}{2}\rho {U_{ref}}^2} \qquad \textbf{Equation 1}$$

We have Jensen's number $\frac{H}{z_0}$ and we have the Reynolds number, $Re = \frac{U_{ref}H}{\nu}$, which are the second and third. The integral scale of the turbulence can be paired with z_0 to obtain the fourth, i.e. $\frac{L_u}{z_0}$. The wind speed profile $\frac{U}{U_{ref}}$ is already non-dimensional and forms the fifth. The turbulence intensity $\frac{\sigma_u}{U_{ref}}$ forms the sixth. The remaining three involve the position coordinates, which can be put into non-dimensional form as $(\frac{x}{z_0}, \frac{y}{z_0}, \frac{z}{z_0})$. So we can write the relationship for the pressure coefficient as

$$C_p = \frac{p-p_0}{\frac{1}{2}\rho {U_0}^2} = function\left(\frac{H}{z_0}, \frac{U_{ref}H}{\nu}, \frac{U}{U_{ref}}, \frac{x}{z_0}, \frac{y}{z_0}, \frac{z}{z_0}, \frac{xL_u}{z_0}, \frac{\sigma_u}{U}\right) \qquad (1a)$$

The relationship could include more terms since we have implicitly assumed that if we obtain the right value of $\frac{\sigma_u}{U}$ that we automatically have obtained the right $\frac{\sigma_w}{U}$ for example. In some situations this may not be the case and we would need to consider more non-dimensional parameters. Likewise we have assumed that if $\frac{L_u}{z_0}$ is matched then $\frac{L_v}{z_0}$ and $\frac{L_w}{z_0}$ would also be matched. If the terrain is very uniform over a good distance then $\frac{U}{U_{ref}}$ and $\frac{\sigma_u}{U}$ become functions only of $\frac{z}{z_0}$. Also, $\frac{L_u}{z_0}$ will become a function only of $\frac{z}{z_0}$. If Reynolds number effects are also negligible then the pressure coefficient does then indeed come to depend only on Jensen number $\frac{H}{z_0}$ and location on the building as specified by non-dimensional coordinates $(\frac{x}{z_0}, \frac{y}{z_0}, \frac{z}{z_0})$, or since $\frac{H}{z_0}$ is a fixed ratio, by $(\frac{x}{H}, \frac{y}{H}, \frac{z}{H})$. Hence, in uniform terrain, and with an isolated building, we have

$$C_p = \frac{p-p_0}{\frac{1}{2}\rho {U_0}^2} = function\left(\frac{H}{z_0}, \frac{x}{H}, \frac{y}{H}, \frac{z}{H}\right) \qquad (1b)$$

One implication to be taken from the above discussion is that when pressure and force coefficients are specified for a particular shape, they are only strictly valid for the terrain conditions and nearby surroundings in which they were originally determined. If the building is surrounded by other buildings or other natural obstacles such as trees, rocks slopes etc, that alter the velocity and turbulence field from the idealized conditions of uniform terrain then the pressure coefficients will be significantly affected.

3.11 Mean and Fluctuating Pressure Coefficients

Since in wind engineering we are dealing almost exclusively with turbulent flows, we need to define the pressure coefficient in a way that makes sense for this situation. In the discussion above we defined the pressure coefficient for the smooth uniform flow case as $C_p = \frac{p-p_0}{\frac{1}{2}\rho {U_{ref}}^2}$ it being tacitly assumed that the pressure p was a mean value. In turbulent boundary layer flow it is necessary to define where we measure the reference velocity U_{ref} and what we mean by the reference static pressure, p_0. Also, since the local pressure p is fluctuating also we need to become more definite in exactly what we are measuring. In turbulent flows the reference location for measuring U_{ref} and p_0 needs to be away from the influence of the building itself, or any other buildings for that matter. For low-rise buildings it is customary to have the reference location at the roof level far upwind of the building or well off to one side. For tall buildings a similar approach can also be used or, in wind tunnel tests it is frequently taken to be high above the building at a fixed reference height of say 500 or 600 m. The reference velocity U_{ref} is usually a mean value, or in some codes and standards it may be defined as a statistically determined peak gust of a given duration. The reference static pressure is without exception taken to be a mean value. However they are defined,

$$C_p = \frac{p(t)-p_0}{\frac{1}{2}\rho {U_0}^2} \quad (2)$$

where p is a function of time t, and the we define mean, peak and root-mean-square pressure coefficients as follows.

Mean coefficient:

$$\overline{C_p} = \frac{\bar{p} - p_0}{\frac{1}{2}\rho {U_{ref}}^2} = \qquad (3)$$

Peak positive coefficient:

$$\widehat{C_p} = \frac{\hat{p} - p_0}{\frac{1}{2}\rho {U_{ref}}^2} \quad (4)$$

Peak negative coefficient:

$$\widecheck{C_p} = \frac{\check{p} - p_0}{\frac{1}{2}\rho {U_{ref}}^2} \quad (5)$$

RMS coefficient:

$$C_{p,RMS} = \frac{\sqrt{\overline{(p(t) - \bar{p})^2}}}{\frac{1}{2}\rho {U_{ref}}^2} \quad (6)$$

Here $\bar{p}$ is the mean pressure, $\hat{p}$ is the peak positive pressure and $\check{p}$ is the peak negative pressure.

3.12 Mean Pressure Coefficients on Rectangular Buildings in Boundary Layer Flow

Figure 24 illustrates the mean flow patterns around a tall building in boundary layer flow. The stagnation point near the top of the building coincides with the region of high mean positive pressure coefficient. The lower positive pressures low down on the building result in a flow down the front face that curls up into a vortex near the base. This core of the vortex then wraps around the sides of the building causing high velocities at ground level around the corners and downwind of the corners. These winds

can be problematic for pedestrians. Strong backflows at ground level may also occur at the bottom of the front face.

The pressures on the rear of the building are all suctions. If there is a passage linking the front face to the rear face as shown in Figure 24, the large difference between the positive front face pressure and the negative rear face pressure leads to accelerated wind flows in the passage, which may result in pedestrian discomfort and potential problems with doors opening into the passage.

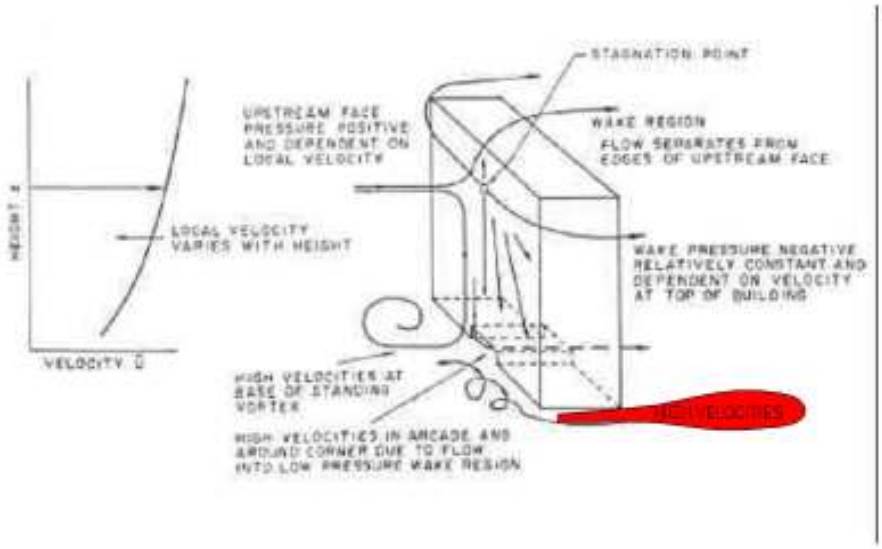

Figure 24 - Flow Patterns Around a building

3.13 Definitions of Mean Force and Moment Coefficients

In turbulent flow, just as the pressure coefficient will fluctuate so will the force and moment coefficients. We can define the mean force and moment coefficients in the same way as we did before except that we replace the drag, lift and moment by their mean values, $\overline{D}$, $\overline{L}$ and $\overline{M}$. Thus

Mean Drag coefficient:

$$C_{\bar{D}} = \frac{\bar{D}}{\frac{1}{2}\rho {U_{ref}}^2 A} \quad (7)$$

Mean Lift coefficient:

$$C_{\bar{L}} = \frac{\bar{L}}{\frac{1}{2}\rho {U_0}^2 A} \quad (8)$$

Mean Moment coefficient:

$$C_{\bar{M}} = \frac{\bar{M}}{\frac{1}{2}\rho {U_0}^2 A b} \quad (9)$$

The above are the definitions for the three-dimensional coefficients. For two-dimensional situations similar definitions apply except that the reference area A is replaced by the reference width b.

3.14 Drag Force Coefficient on Two-Dimensional Rectangular Prisms

The drag force on two-dimensional rectangular cross-sections depends on their length to width ratio $\frac{d}{b}$ as depicted in Figure 25, which applies to smooth flow. At very small $\frac{d}{b}$ the drag coefficient is essentially the same as a two-dimensional plate, i.e. close to 2.0. The 10 flow separates at the two upwind corners and at small $\frac{d}{b}$ stays separated over the length d of the after-body. However, as d/b increases the streamlines marking the edge of the separated zone become more highly curved and this makes the base pressure more negative. At about $\frac{d}{b} = 0.6\ to\ 0.7$ the flow is able to re-attach to the top and bottom surfaces of the prism, which then reduces the width of the wake and reduces the drag. Hence, the maximum drag at $\frac{d}{b} = 0.6\ to\ 0.7$.

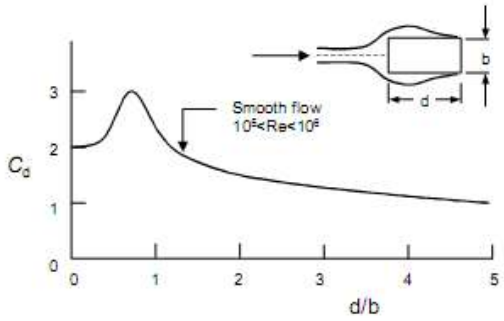

Figure 25 - Drag Coefficient of Rectangular Prisms in Smooth Flow

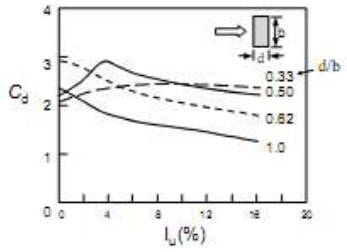

Figure 26 - Effect of Turbulence Intensity of Maximum Drag Coefficient on Rectangular Prisms

When turbulence is present in the wind it affects the behavior of the separated shear layers coming off the front corners, resulting in more efficient mixing and earlier reattachment, Figure 25. It can be seen in Figure 26 that in 4% turbulence intensity a similar drag coefficient of about 0.3 is obtained at $\frac{d}{b} = 0.62$ as is obtained in smooth flow for $\frac{d}{b} = 0.62$.

4 Test in the wind tunnel

4.1 Wind-tunnel layouts

The first use of a wind tunnel to measure wind forces on buildings is believed to have been made by Kernot in Melbourne Australia (1893). A sketch of the apparatus, which he called a "blowing machine", is given in Figure 27. This would now be described as an "open- circuit, open-test section" arrangement. With this equipment, Kernot studied wind forces on a variety of bluff bodies – cubes, pyramids, cylinders, etc. and on this roofs of various pitches. At about the same time, Irminger (1894) in Copenhagen, Denmark, used the flow in a flue of a chimney to study wind pressures on some basic shapes (Larose and Franck, 1997).

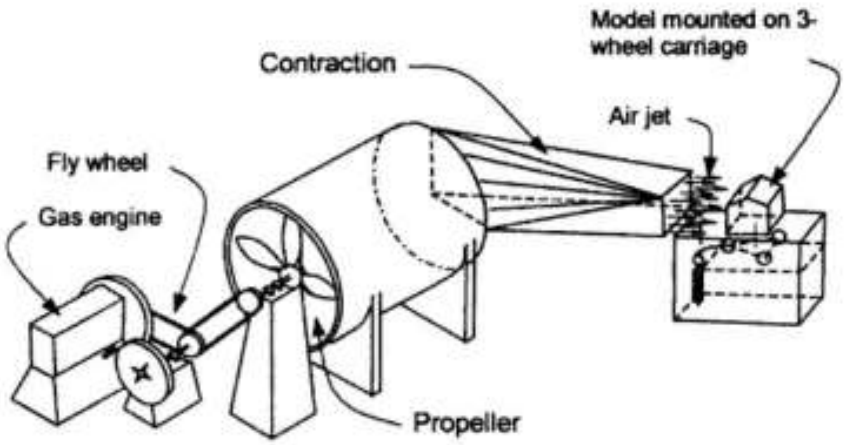

Figure 27 - Scheme of a blowing machine

Wind tunnels for aeronautical applications developed rapidly during the first half of the twentieth century, especially during and between the two World Wars. The two basic wind-tunnel layouts – the open circuit or "NPL (National Physical Laboratory) type" and the closed circuit or "Gittingen type" – were developed during this period, named

after the research establishment in the United Kingdom and Germany where they originated. These two types are outlined in the following sections.

4.1.1 Open-circuit type

The simplest type of wind-tunnel layout is the open-circuit or NPL type. The main components are shown in Figure 28.

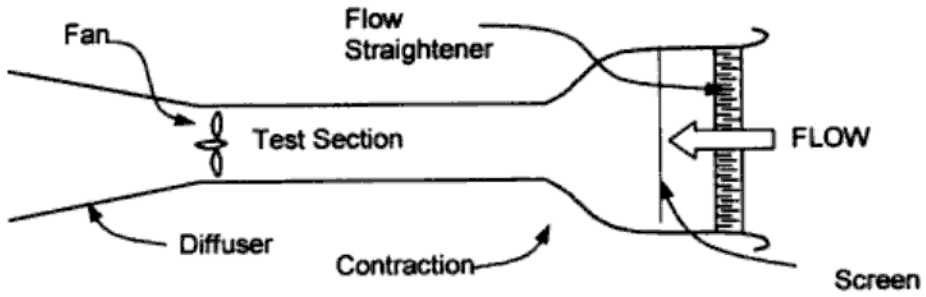

Figure 28 - Open circuit scheme

The contraction, usually with a flow straightener and fine mesh screens, has the function of smoothing out mean flow variations and reducing turbulence in the test section. For modeling atmospheric boundary-layer flows, which are themselves very turbulent, it is not essential to include a contraction, although it is better to start with a reasonably uniform and smooth flow before commencing to simulate atmospheric profiles and turbulence. The function of the diffuser is to conserve power by reducing the amount of kinetic energy that is lost with the discharging air. Again this is not an essential item, but omission will be at the cost of higher electricity charges.

Figure 28 shows an arrangement with an axial-flow fan downstream of the test section. This arrangement is conducive to better flow, but, as the function of the fan is produce a pressure rise to overcome the losses in the wind tunnel, there will be a pressure drop

across the walls and floor of the test section that can be a problem if leaks exist. An alternative is a "blowing" arrangement in which the test section is downstream of the fan. Usually a centrifugal blower is used, and a contraction with screens is essential to eliminate the swirl downstream of the fan. However, in the arrangement the test section is at or near atmospheric pressure.

Both the arrangements described above have been used successfully in the wind engineering applications.

4.1.2 Closed-circuits type

In the closed-circuit, or Gittingen-type, wind tunnel, the air is continually recirculated, instead of being expelled. The advantages of this arrangement are as follows:

- It is generally less noisy then the open-circuit type.
- It is usually more efficient. Although the longer circuit gives higher frictional losses, there is no discharge of kinetic energy at exit.
- More than one test section with different characteristics can be incorporated.

However, this type of wind tunnel has a higher capital cost and the air heats up over a long period of operation before reaching a steady-state temperature, this can be a problem when operating temperature-sensitive instruments, such as hot-wire or other types of thermal anemometers, which use a cooling effect of the moving air for the operation.

For example, the wind tunnel at Politecnico of Milan (Figure 29) is a closed-circuits type developed vertically.

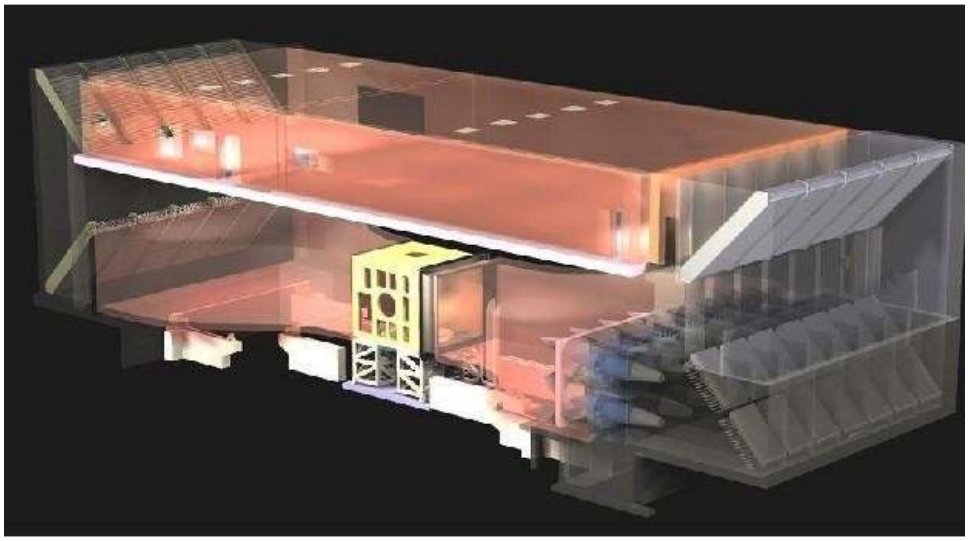

Figure 29 - The wind tunnel in Politecnico of Milan

In order to run the main test for this work, a wind tunnel which belongs to the RWDI company at Miramar in Florida (Figure 30) has been used. It is a closed-circuit wind tunnel, like the one in Politecnico, and it is a boundary layer wind tunnel. Also the dimensions of the tunnel are very similar to each other.

Figure 30 - Miramar wind tunnel

Some tests were also run in the smaller wind tunnel in the laboratories of the University of Miami (Figure 31). This was an open-circuit type.

Figure 31 – University of Miami wind tunnel

4.1.3 Simulation of the natural wind flow

Primarily, the simulation of the atmospheric boundary layer in gale, or large-scale synoptic conditions, is discussed. This type of large-scale storm is dominant in the temperate climates for latitudes greater than 40° (and Miami is like 25°). Even in large-scale synoptic wind storms, flows over sufficiently long homogeneous fetch lengths, so that the boundary layer is fully developed, are relatively uncommon. They will occur over open sea with consistent wave heights, and following large fetches of flat open country or desert terrain. However, buildings or other structures, which are exposed to these conditions, are few in number. Urban sites, with flat homogeneous upwind roughness of sufficient length to produce full development of the boundary layer, are also relatively uncommon. However, there have been sufficient measurements in conditions that are close to ideal to produce generally accepted semi-theoretical models of the strong wind atmospheric boundary layer for engineering purposes. These models

have been validly used as the basis for wind-tunnel modeling of phenomena in the atmosphere.

In the case of the wind loading and response of structures, such as buildings, towers, bridges, etc…, gales produced by large, mature, extra-tropical depressions are adequately described by these models, and they form a benchmark by which wind-tunnel flows are usually assessed. However, there are significant differences of opinion regarding some turbulence properties, such as length scales and spectra, which are important in determining wind forces and dynamic response. These uncertainties should be considered when assessing the reliability of wind-tunnel tests as a predictor of wind effects on real structures.

These models are also not good ones for storm winds produced by localized thermal mechanisms, namely tropical cyclones (hurricanes, typhoons), thunderstorms (including tornadoes) and monsoons. Wind produced by these storms are the dominant ones for design of structures in latitudes within about 40° from the equator. In fact the object of this thesis is the normal effect caused by high wind velocity, not considering these kind of phenomena.

The most important matters for wind tunnel tests are the reproduction of the turbulence, how to treat the data with the aid of statistic, and how to compare the results with reality as far as time, frequencies, and velocity.

4.2 Experimental Set-up

Testing was conducted at the RWDI Boundary layer wind Tunnel at Miramar, Florida. The building studied had a cubic shape with full scale dimensions of 30.48m (100ft) x 30.48m (100ft) x 30.48m (100ft). The reason why a cubic model of these dimensions was chosen has already been mentioned in the introduction.

4.2.1 The model

First of all the scale of the model has to be chosen. It has been already explained the reason of the shape and the focus on the edges. Furthermore the literature hasn't so much data about wind pressure on this kind of intermediate height building. A scale of 1:60 was chosen: it leaves enough room around the model allowing the wind flow to flow around without problem. From the common practice a ratio between the cross-section of the model and the one of the wind tunnel greater than 10% allows this requirement to be satisfied. The length scale is:

$$\lambda_l = \frac{D_{model}}{D_{prototype}} = \frac{1}{60}$$

The model was made with Plexiglas to a scale of 1:60. A photograph of the building model placed in the wind tunnel is in Figure 32.

Figure 32 - Model set down in the wind tunnel

Five hundred and four (504) pressure taps were provided on one quadrant of the roof, and concentrated on the edge of the vertical facades as shown in Figure 33, Figure 34, and Figure 35.

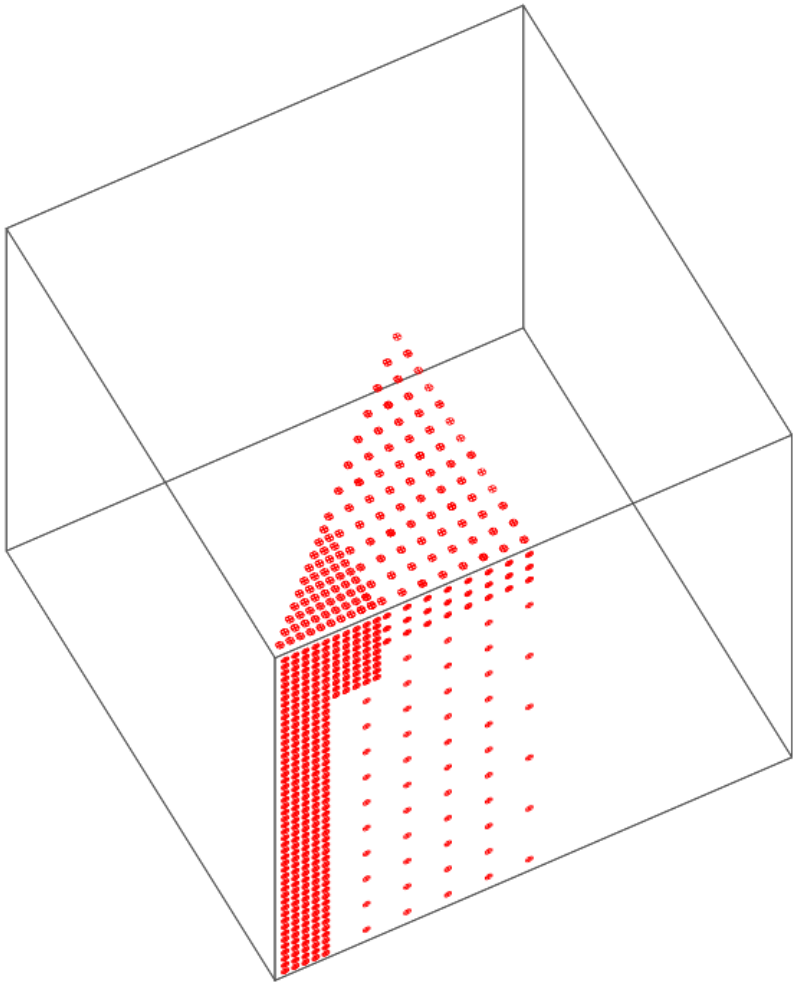

Figure 33 - 3D taps visualization

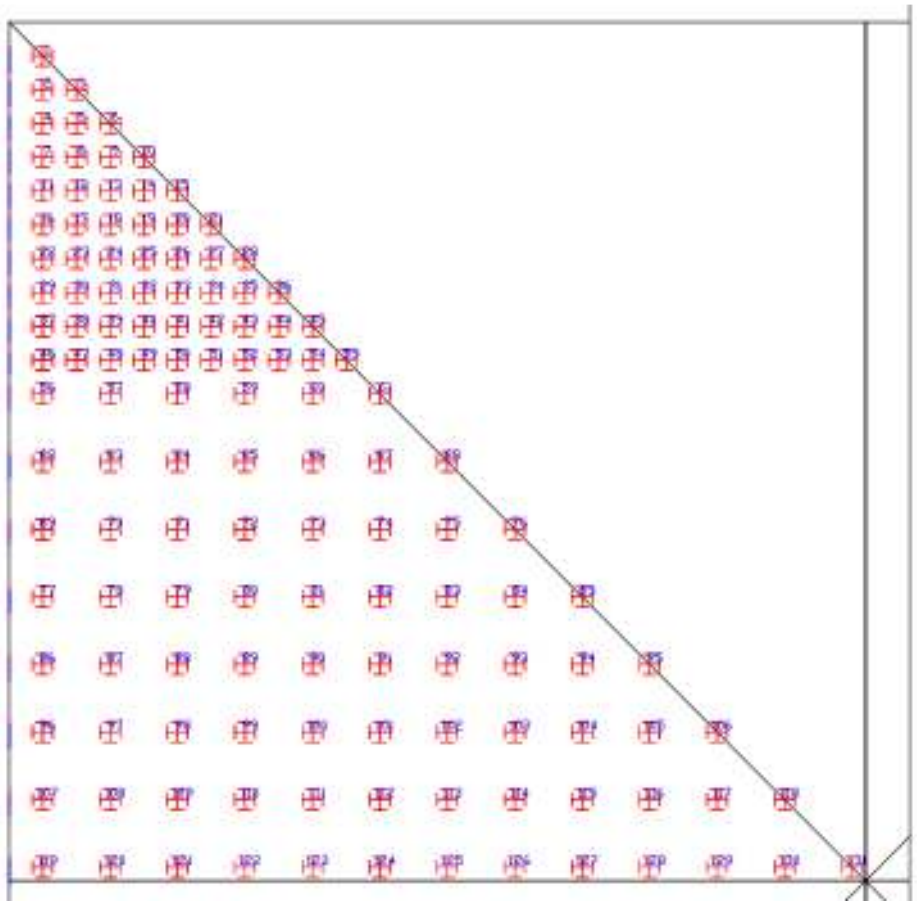

Figure 34 - Roof taps

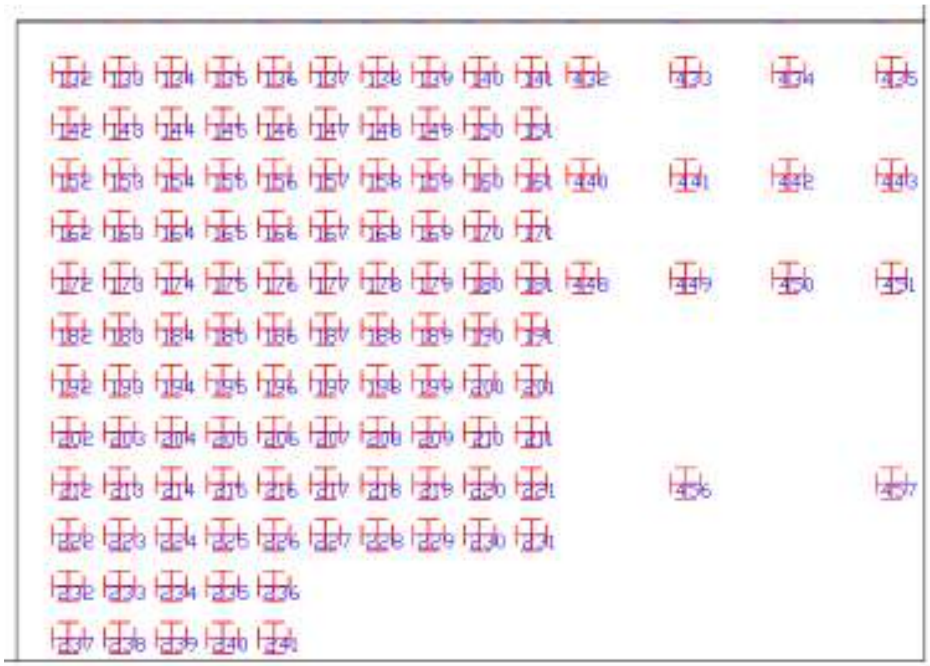

Figure 35 - Corner taps on the wall side

This type of building has been chose for many reasons. First of all, in order to focus on edge effect and roof effect, following the proportions of the effective area of the ASCE, measurements are concentrated in a reduced part of the structure. The use of symmetry, on the other hand, is fundamental to be mentioned because it allows to mirror the pressure measurements in many directions, building the pressure behavior on the whole building. This is why it is possible to focus only on a octave of the structure. In this way with the same wind tunnel technology it is possible to take advantage of symmetry in order to have more precise measurements. This very theoretical model is very common and easy to study, but with this focus, this scale and the aim of this study, it is not very frequent in the literature.

The structure is divided in three areas: the first one with the distance among the tap of 1 cm, the second one of 2 cm and the third one 4 cm (the third one only to monitor the value range).

The first area has 55 pressure taps on the roof part, 100 in the corner zone of one lateral side and other 200 (40 rows of 5 pressure taps each) along the edge. The second is the rest of the roof (76 pressure taps) and the superior edge of the side (24 pressure taps), designed in order to cover more than a strip of 1/10 of the dimension of the cube, as it is written on ASCE. The last 54 pressure taps are spread all over the lateral surface.

The model used was built in the lab of the University. The thickness of the sheets of Plexiglas is ¼ inches (6.35 millimeters). Therefore, in order to obtain a cube, the sheet was cut in 5 pieces, while the bottom part was left open in order to mount it in the wind tunnel. The first part was the top surface of the cube and was 20 x 20 inches (0.508x0.508 meters). The left 4 equal pieces were 19 and ¾ inches x 19 and ¾ inches (0.502x0.502 meters) each and these created the four side surfaces. These parts are smaller because they used the thickness of the roof and of the next side to reach the external dimension of 20 inches.

Figure 37 - Cutting the plexiglass

Figure 36 - Drilling the holes

After the cutting, the surface was sanded a little bit in order to create the same conditions of the real building. Then holes of #44 were drilled, following the

disposition of taps just discussed. Later, with the aid of a particular chlorine glue, the box was built. Than every single pressure tube was glued using superglue and accelerator. Particular attention is needed during this procedure: it is important to fix the tubes so that they stick out of the surface and to cut them off when the glue is dry. This allows the holes to be perfect. At last all the surfaces were sanded again.

Figure 38 - Gluing the taps

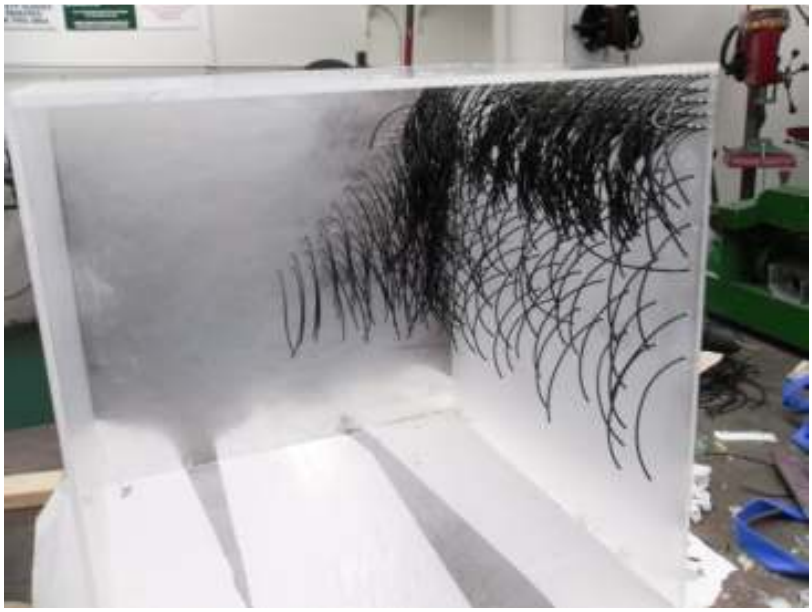

Figure 39 - Interior visualization of the tubes

Figure 40 - Sanding the surface of the box

4.2.2 Wind Tunnel setup

The second necessary factor to pay attention to is the velocity. At first the full scale velocity and then also the prototype velocity. The test was carried on in Miami, Florida, so the interest is focus on the climate characteristic of that zone. Referring to the ASCE and to Irwin formula, a full scale velocity from the code need to be fixed.

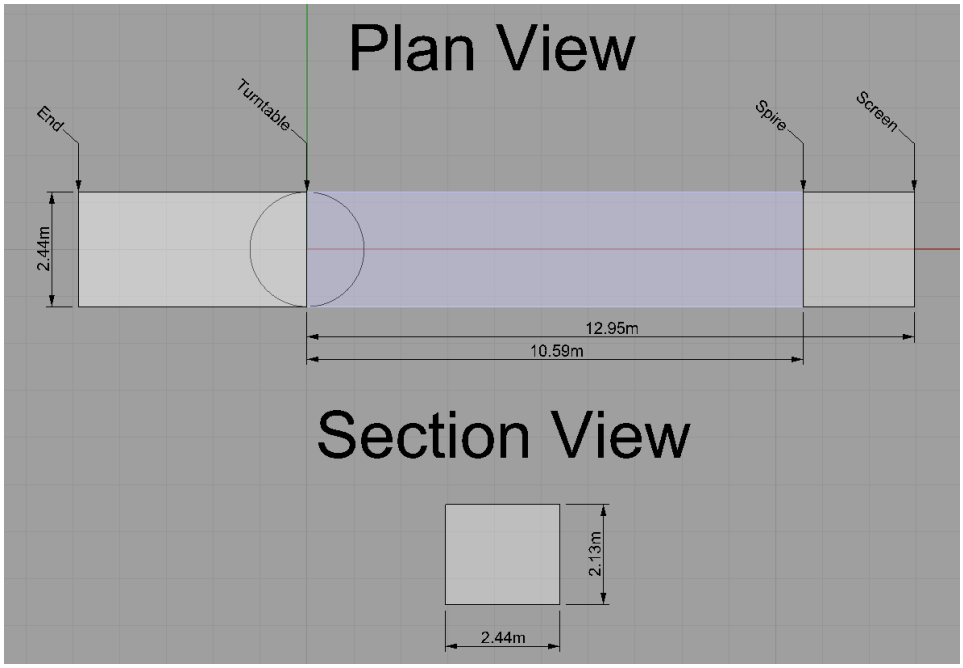

Figure 41 - Plan view of the Wind Tunnel in Miramar, FL

The Figure 41 represent the basic wind speed for the Florida in ASCE, and Irwin suggests a formula to find the U from the values on the code. It not the regular formula for the wind profile, because the ASCE 7 Standard bases its wind calculation on the 3-second gust velocity in standard open terrain at 10 meters height, which is called the

basic wind speed, and because it selected z_{ref} = 10 meters, the actual formula for mean velocity profile is given as

$$\frac{U}{U_{basic}} = \bar{b}\left(\frac{z}{10}\right)^{\bar{\alpha}}$$

Where U_{basic} is basic wind speed, the value of b is taken as 0.8 for Exposure D and z is measured in meters. Choosing the value of 63 m/s, obviously for Exposure D, and maintaining the reference at 10 meters the velocity to compare is 50 m/s.

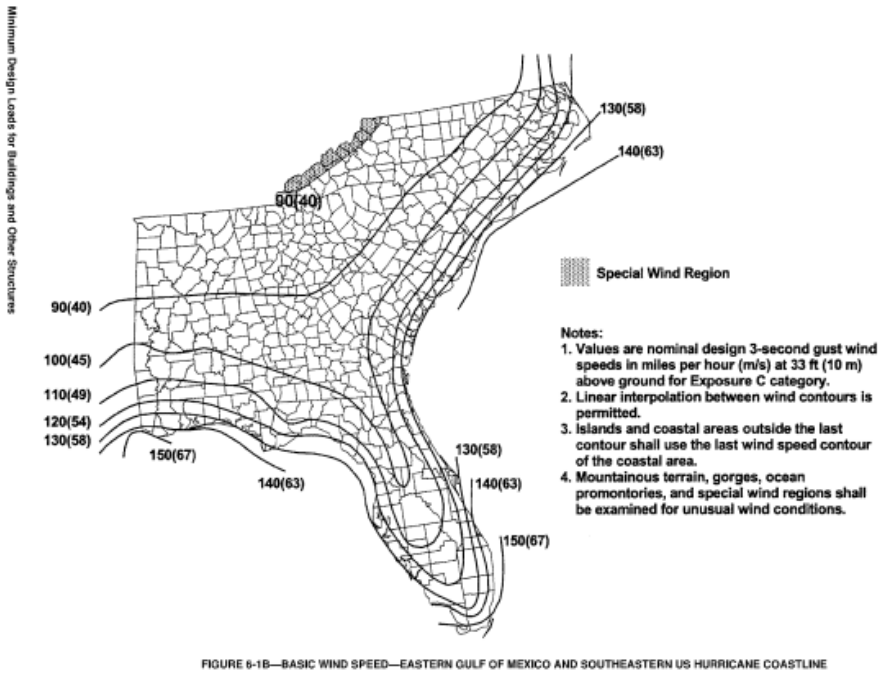

Figure 42 - Wind ASCE map

The model velocity at the same height (scaled height) is around 11 m/s, referring to the experimental profile wind tunnel's technicians gave to us. In fact they decided to have for this scale the reference pressure with the Pitot tube at the real height of 60 inches

(1,52 meters and 91 meters in full scale) with a speed of 15 m/s. At the end using the experimental values of the wind tunnel during the set up of the simulation it is possible to define the speed scale factor.

$$\lambda_u = \frac{U_{model}}{U_{prototype}} = \frac{50{,}40\ m/s}{11{,}25\ m/s} = 4{,}48$$

The floor roughness and the spires were adjusted to obtain the mean velocity profile and turbulence intensity analogous to exposure D in ASCE-7. The calibration was made thanks to previous results by the RWDI technicians.

The mean velocity profile obtained from the wind tunnel measurements compared well with the velocity profile corresponding to exposure D given by

$$\frac{\overline{U}}{\overline{U}_{ref}} = \left(\frac{z}{z_{ref}}\right)^{\overline{\alpha}}$$

As already mentioned, in the present study the reference height is 60 inches (91.4 meters), which is the height where the pitot tube was placed in the wind tunnel. Therefore, knowing from the ASCE that for this class of exposure α = 1/9, the profile will be given by

$$\frac{\overline{U}}{\overline{U}_{91.4}} = \left(\frac{z}{91.4}\right)^{\overline{\alpha}}$$

The comparison between the wind speed profile of the setup and from the code is reported in the following graph:

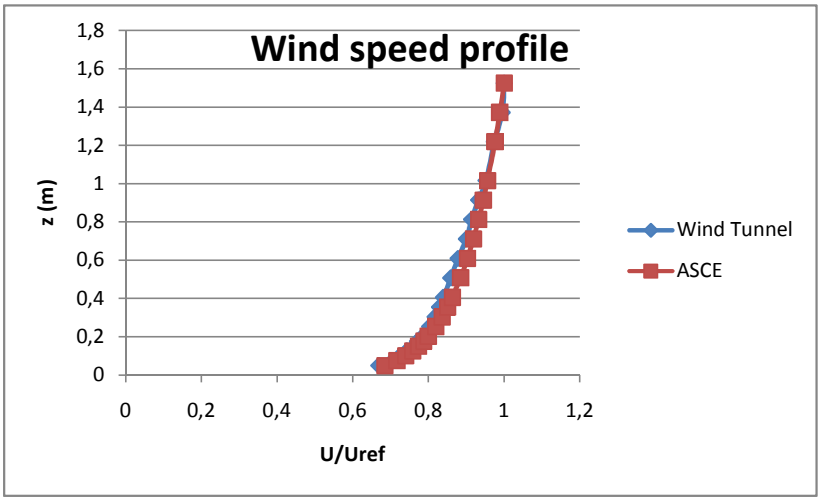

Graph 1 - Wind speed profile

Z,meters	U/Uref Wind Tunnel	U/Uref ASCE
0,05	0,67	0,69
0,08	0,71	0,72
0,10	0,73	0,74
0,13	0,74	0,76
0,15	0,76	0,77
0,18	0,77	0,79
0,20	0,79	0,80
0,25	0,80	0,82
0,30	0,82	0,84
0,36	0,83	0,85
0,41	0,84	0,86
0,51	0,86	0,89
0,61	0,88	0,90
0,71	0,90	0,92
0,81	0,91	0,93
0,91	0,93	0,94
1,02	0,95	0,96
1,22	0,97	0,98
1,37	1,00	0,99
1,52	1,00	1,00

Table 1 - Wind speed values in the Wind Tunnel and from the Code

The turbulence profile was also given by the RWDI company. This profile compared well with the ASCE formulation only up till 1 meter model scale height, using a z_0=0.0015. The formulation from the ASCE is the following

$$I_u = \frac{1}{\ln \frac{z}{z_0}}$$

The comparison is shown in the following graph:

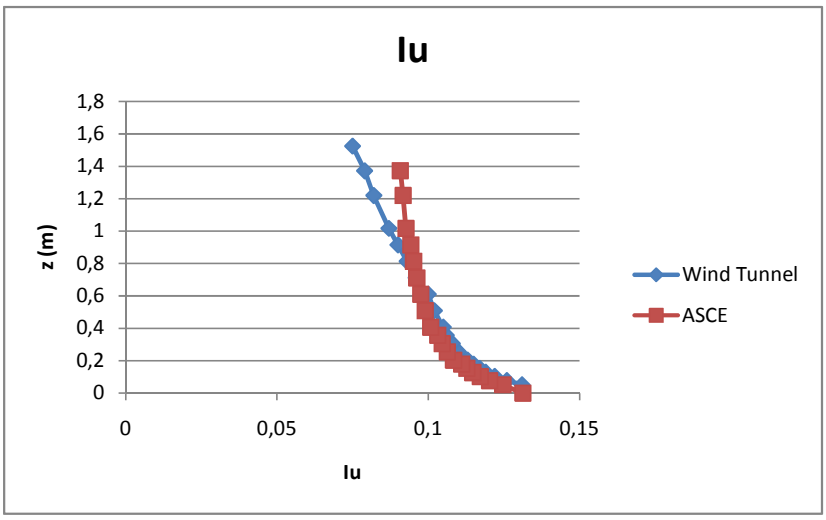

Graph 2 - Wind Turbulence values in the Wind Tunnel and from the Code

4.2.3 Sampling time

It is really important to be able to relate model time to full scale time. Looking for a non-dimensional grouping including time we can see that time can be made non-dimensional by combining it with a length and velocity scale.

$$t^* = \frac{tU_{ref}}{L}$$

This relationship relates model time to full-scale time, since t* will be the same on the model as at full scale. In modeling parlance the term "prototype" is often used to denote full scale, coming from the days when a wind tunnel model or water tank model was used to study a prototype version of an aircraft of ship. Thus, using subscripts m and p to denote model and prototype quantities respectively, we have

$$\frac{t_m U_{ref,m}}{L_m} = \frac{t_p U_{ref,p}}{L_p}$$

This implies that the ratio of model time to full-scale time is

$$\frac{t_m}{t_p} = \left(\frac{L_m}{L_p}\right)\left(\frac{U_{ref,p}}{U_{ref,m}}\right)$$

Therefore, considering that the model has a scale of 1:60 and the ratio of full scale velocity to model velocity is 3,56, then model time will be full-scale time divided by 60 and multiplied by this ratio. It means that to simulate one hour of scale-wind it is necessary to sample for at least

$$t_m = \frac{3600}{60} * 4.48 = 268\ seconds$$

in the wind tunnel.

A similar relationship applies for model and full-scale frequency. A non-dimensional form for the frequency is

$$n^* = \frac{nL}{U_{ref}}$$

Therefore, using the same m and p subscripts for model and prototype quantities we have

$$\frac{n_m L_m}{U_{ref,m}} = \frac{n_p L_p}{U_{ref,p}}$$

Therefore the ratio of model frequency to full-scale frequency will be

$$\frac{n_m}{n_p} = \left(\frac{L_p}{L_m}\right)\left(\frac{U_{ref,m}}{U_{ref,p}}\right)$$

Hence, using the values already obtained before, then the model frequency will be 13 times full scale frequency. This is important when measuring pressures. This means that to be able to resolve all frequencies up 1 Hz at full scale then this implies our instrumentation in the wind tunnel must have sufficient frequency response to be able to resolve model frequencies up to 13 Hz.

For this work it has been decided to use a higher number of measurements, choosing a lower frequency equal to 64 Hz. This value, still using a velocity ratio of 4.48 leads to a value of $n_p = 4.47$.

The Wind Tunnel in Miramar gives the opportunity to measure up till 18432 data points for every test. This yields to a value of

$$t_{model} = \frac{18432}{64} = 288\ sec$$

It means that the wind tunnel test represent a real event of

$$t_p = \frac{t_m}{\left(\frac{L_m}{L_p}\right)\left(\frac{U_{ref,p}}{U_{ref,m}}\right)} = 3857\ sec$$

With these choices the prototype time is a little longer (7%) than the minimum one requested by the code.

At the end we should have all the scale factors (length scale, speed scale and time scale). Also we paid attention to the reference values of the code (ASCE, the American code) in order to compare the values we will find with the code restrictions.

There are other secondary restriction to take care of, which are linked to parameters of the flow (Strouhal, Reynolds and Froude number). These relationships are less important and we mention Reynolds condition, which says that length scale factor times speed scale factor should be close to one. But it is very useless and undoable; on the other hand the Reynolds number is meaningful for cylindrical or curved shape and in this case with a clear separation of the flow because of the edges, we school consider the forces not dependent on Reynolds number.

Defining the time scale factor and the frequency scale factor:

$$\lambda_f = 13{,}39$$

$$\lambda_t = 0{,}07$$

4.3 Rotation

Tests were conducted at 10 degree angles intervals by rotating the model against clockwise. There is a platform under the model and the model is screwed in the middle of it just over a big hole where all the tubes could be gathered together. In this way it is possible to simulate the wind coming from all the possible directions around the box and so it is possible to study and find the worst situation. In this way it is possible to create all the different situation of wind exposure for each direction using symmetries and the combination as the following **Errore. L'origine riferimento non è stata trovata.** and Figure 44 show.

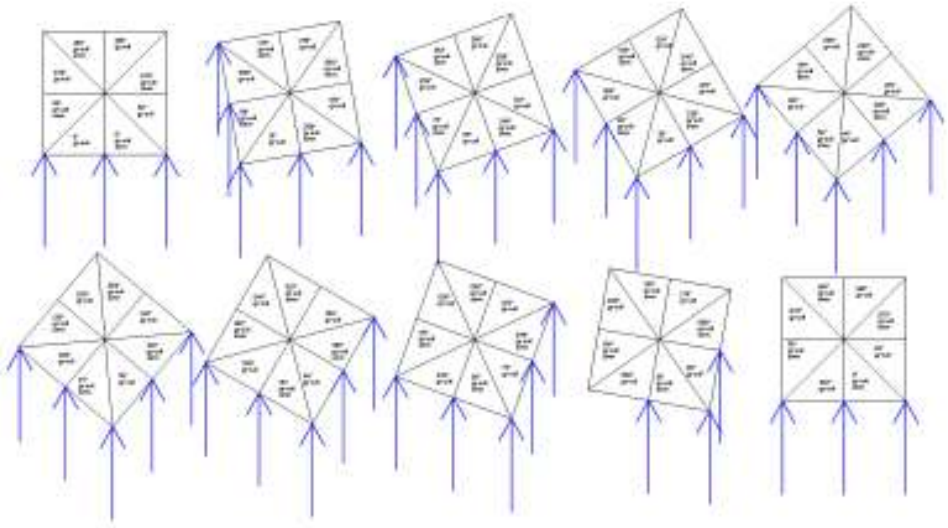

Figure 43 - Symmetry combinations and all the rotation

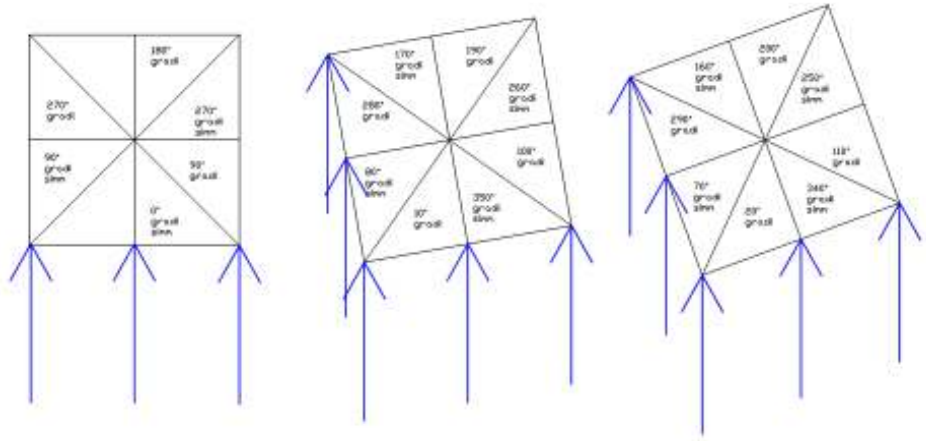

Figure 44 - Zoom on symmetry combinations and all the rotation

It is possible rotate the rotated cube to have the cube and the direction of the wind changing. It is very clear from the next Figure 45.

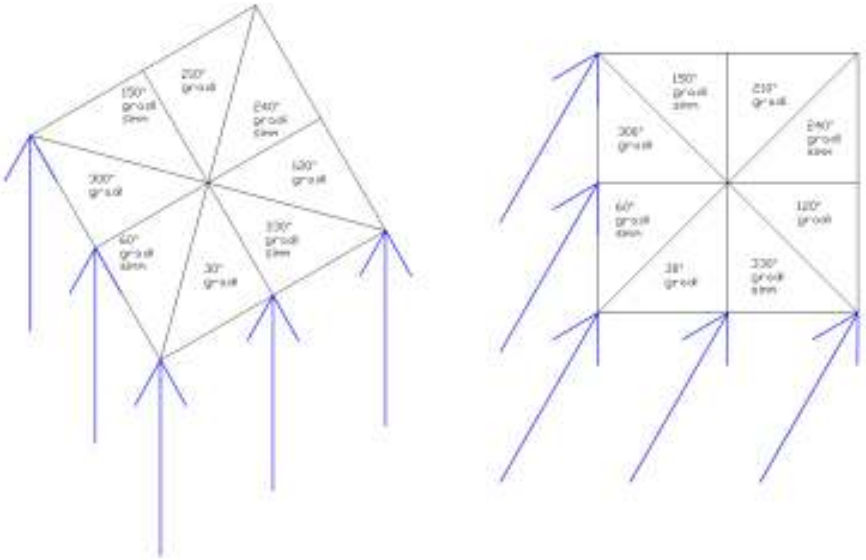

Figure 45 - Combination of the different wind directions

4.4 Pressure coefficients

The data test are interpreted using pressure coefficients, C_p and GC_p.

4.4.1 Pressure coefficients C_p

The C_p is obtained from the peak recorded suction p_{max} as follows:

$$C_p = \frac{p_{max}}{p_{30}}$$

Where p_{30} is the mean reference pressure recorded at the height of the roof of the building (h=30 meters full scale).

During the test only the pressure at the Pitot tube mounted in the wind tunnel at the height of 60 inches (91 meters full-scale) was measured. For this reason, using the following proportion

$$\frac{p_{90mean}}{{v_{90mean}}^2} = \frac{p_{30mean}}{{v_{30mean}}^2}$$

It is possible to rewrite the C_p expression with known variables:

$$C_p = \frac{p_{max}}{p90}\left(\frac{V90mean}{V30mean}\right)^2$$

The calculations yields to

$$C_p = \frac{p_{max}}{p90} * 1.35$$

4.4.2 Pressure coefficients GC_p

The ASCE (American Society of Civil Engineering) uses the pressure coefficient GC_p. This coefficient is obtained from the C_p but it also takes into account the gust effects.

$$GC_p = \frac{p_{max}}{p90}\left(\frac{V90mean}{V30mean}\right)^2\left(\frac{V30mean}{V30gust}\right)^2$$

Where V30gust is the 3 second gust speed at 30m height (roof height) in m/s.

The relationship between the mean velocity and the 3 second gust velocity can be calculated as (ASCE and Irwin)

$$\frac{V_{z,mean}}{V_{gust}} = \frac{1}{(1+gI)}$$

Where g is the durations of the gust, and I is the intensity of the turbulence at height z.

This yields to the final expression of GC_p:

$$\mathrm{GC_p} = \frac{\mathrm{p_{max}}}{\mathrm{p90}}\left(\frac{\mathrm{V90mean}}{\mathrm{V30mean}}\right)^2 \frac{1}{(1+gI)}$$

For the current study g=3sec. The intensity of the turbulence at 30 meters is taken from the Wind Profile in the Wind Tunnel (model scale height of 0.5 m) and has a value of I=0.102. Finally, using the mean velocities from the Profile (Graph 1), Eq. (XXX) reduces to,

$$\mathrm{GC_p} = \left(\frac{\mathrm{p_{max}}}{\mathrm{pitot}}\right)(0.795)$$

Actually, the proper definition of the pressure coefficients should depend on the height where the coefficient is calculated. In this work the coefficients were also calculated considering the changing reference height for the positive pressures at the frontward side. For the suctions, on the other way, the roof height is still the reference height for the coefficients.

The coefficients are now calculated taking in account the changing height of reference:

$$\mathrm{C_p} = \frac{\mathrm{p_{max}}}{\mathrm{p90}}\left(\frac{\mathrm{V90mean}}{\mathrm{Vzmean}}\right)^2$$

$$\mathrm{GC_p} = \frac{\mathrm{p_{max}}}{\mathrm{p90}}\left(\frac{\mathrm{V90mean}}{\mathrm{Vzmean}}\right)^2 \frac{1}{(1+gI(z))}$$

4.5 Cladding studies - measurements' problems

One of the most common applications of the wind tunnel method is the determination of the design wind pressures for cladding. This is done usually at a scale in the range 1:200 to 1:500, with 1:400 being most typical. In this work a major scale was used in order to obtain more precision on the edge (which are in the most problematic zone). The models are instrumented with pressure taps that are connected via tubing to solid-state pressure transducers. The tubing is necessary for space reasons: there is insufficient space in the model to mount transducers directly on the surface. The tubing system does introduce distortion of the pressure signal in going from the tap to the transducer but this can be removed by special signal processing methods (e.g. the inverse transform method, Irwin and Cooper) or is sometimes controlled by maintaining short tube lengths and/or inserting special restrictors in the tubes. Typically the model of a tall building is instrumented with between 500 and 1000 pressure taps. On very large structures the number may go as high as 2000. In this model, as already described, 504 taps were used.

The pressure signal from each tap is typically sampled for the equivalent of about one hour at full scale which, as indicated above, scales to about 288 seconds typically at model scale. Figure 46 shows typical pressure signals in the form of pressure coefficient on a windward wall and a side wall. Signals such as these are recorded typically for 36 directions at 10 degree intervals. Figure 47 shows an example of the variations with wind direction of mean, RMS and peak pressure coefficients from a pressure tap.

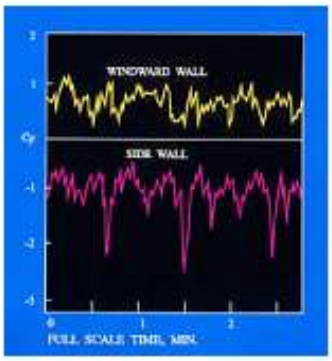

Figure 46 - Typical pressure signals on windward and side wall (from Irwin research)

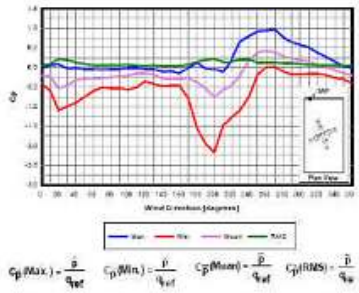

Figure 47 - Example of pressure coefficient variation with wind direction (from Irwin research)

4.5.1 Tube Transfer Correction

The pressure recorded by the transducers was corrected for tube transfer by using the procedure recommended by Irwin. The data obtained for each test was separated into 18 blocks of 1024 points. FFT analysis was conducted on each block of data and the tube transfer correction was applied in the frequency domain. The corrected frequency response was then inverted to obtain the corrected pressure time history.

The procedure was repeated for all the 18 blocks of data to obtain the complete pressure-time history. The corrected and the uncorrected pressure-time histories for the first second are shown in Fig.XXX for the corner tap tested with an approach angle θ=330 degrees. The difference in magnitude and the phase shift between the corrected and uncorrected data can be noticed.

In measurements of time-varying pressures on building models, it is common practice to measure the pressure via lengths of tubing connecting the surface pressure taps to a scanivalve which contains a pressure transducer (Figure 48). This approach makes economical use of pressure transducers, since the surface pressure can be measured at many locations in sequence by a single transducer. The alternative method of using flush mounted transducers is expensive and is hampered by space limitations in small models.

Figure 48 - Scanivalve which contains the pressure transducer device

In the present study, run in the RWDI Wind Tunnel of Miramar, we stuck to their common practice to use the first method because it is more practical for the complex geometry with which they usually have to deal. As described earlier, the five hundred and four taps were connected to the scanivalve through tubes fixed on the surface of the model (Figure 49).

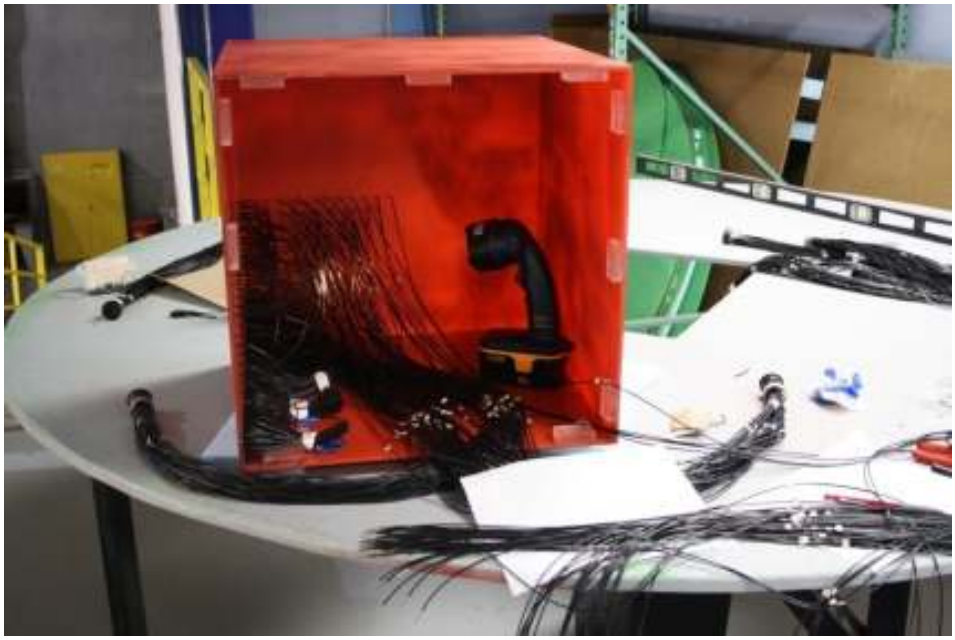

Figure 49 – Connections between the tubes on the surfaces and the pressure transducers

However, the use of tubing systems and scanivalve always introduces distortion of the pressure fluctuations, depending on the tube length and diameter, on the geometry of the scanivalve internal passageways and on the transducer internal volume.

There are many methods of minimizing distortion that have been used in past studies. In the present work a is used a digital method (reference).

The pressure signal is corrected digitally for distortion effects using the inverse of the tubing system transfer function. The method is applied to some typical pressure signals and is shown to virtually eliminate distortion both of amplitude and phase. It allows considerably longer tube lengths and a higher frequency response to be obtained than with the other methods.

Irwin, Cooper and Girard (1979) compared this method with other two methods that do not require computer aid. The first alternative method consists in inserting restrictors in tubing systems: this is evaluated and found to reduce the distortion to acceptable levels for the short tube lengths and retains the advantage of not requiring a computer. On the other hand, this method does not eliminate phase distortion. The second alternative method is even simpler and is just to keep the tube length and transducer as small as possible.

Tubes of 1 millimeter of diameter and 1 meter (?) of length were connected to the model.

Taking in account that nowadays the use of a computer to apply the correction is not an issue, the digital correction using the inverse of the tubing system transfer function has been chosen.

Referring to the simple pressure system shown in Figure 50 consisting of a pressure tap leading to a pressure transducer, it is clear that the system is characterized by the tube length, its internal diameter and the transducer volume.

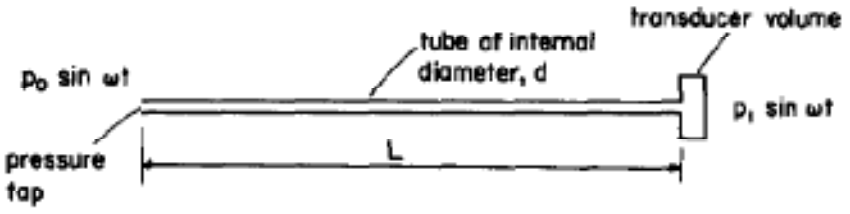

Figure 50 - Tubing system

Let the fluctuating pressure at the pressure tap be P0(t). Using a Fourier Transform it can be written as

$$P_0 = \sum_{n=-\infty}^{+\infty} A_n e^{in\omega t}$$

Where A_n are complex Fourier coefficients and $i = \sqrt{-1}$. Similarly, the pressure at the pressure transducer can be written as

$$P_1 = \sum_{-\infty}^{+\infty} B_n e^{in\omega t}$$

Where B_n are complex Fourier coefficients. Let T_n be the tubing system transfer function, then

$$B_n = A_n T_n$$

Thus, the Fourier coefficients of the desired pressure $P_0(t)$ can be calculated from

$$A_n = \frac{B_n}{T_n}$$

It means that, starting from the distorted signal at the transducer $P_1(t)$, the undistorted signal $P_0(t)$ can be obtained by computing the Fourier transform B_n of the measured pressure. After that, computing A_n using Equation XXX (Bn/Tn) and finally computing the inverse Fourier Transform $P_0(t)$ of A_n.

Of course, the transfer function T_n has to be known.

In the present study the problem was to compute the Fourier Analysis for a large amount of data: each one of the 36 angles has 512 (504 + 8 Pitot tubes) pressure histories in 18432 instants of time. With the aid of MathCad a program was made that,

using the recorded values as an input, could recursively compute the Fourier analysis and give as an output the corrected pressures. The transfer function was given from the RWDI company.

In the program the data are divided in 36 blocks in time of 512 acquisitions each, and the correction is applied on every block separately. Graph 3 shows the difference of the data before and after the correction for tap number 6 at 10 degrees.

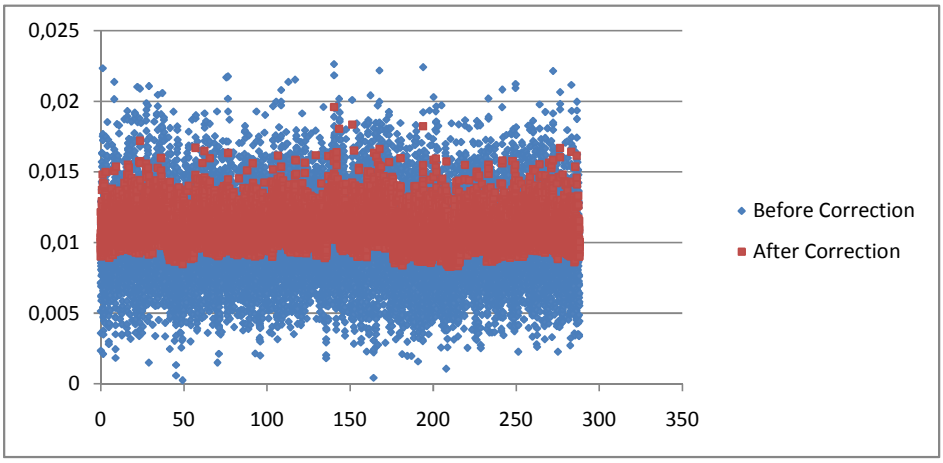

Graph 3 - Data before and after corrections

From this graph it is clear how the scattering of the data is reduced, but the pattern and the peaks are maintained.

In Appendix X can be found a copy of the program wrote in Mathcad to perform the tube transfer correction.

4.5.2 Fisher Tippet correction

In order to predict the cladding wind loads for a given return period, the wind tunnel results are integrated with the wind climate model. There are two methods typically used by RWDI to perform this integration. In one method, the historical (or simulated

as is the case with hurricanes or typhoons) wind record is used to determine the full-scale cladding wind pressures for each hour, given the recorded wind speed and direction and the wind tunnel predictions for that direction. By stepping through the wind speed and direction data on an hour-by-hour basis, a time history of the resulting peak pressure is generated. Then, through the use of extreme value fitting techniques, statistically valid peak responses for any desired return period are determined.

The second method is the Upcrossing Method as described Irwin and Sifton. Anyway this method will not be used for the present work

As a result of the analysis design pressures for a given return period, usually 50 years, can be mapped on the surface of the building. Typically these would include an allowance for internal pressures but there is no need to take them into account in the present work.

Much of wind engineering is about risk and optimization of structures for wind. This means that the probability of various events occurring needs to be estimated. Examples are:

- The maximum 3-second gust wind speed expected in 50 years at a site.
- The maximum wind pressure on cladding in 50 years at a point on a building.
- The maximum expected horizontal acceleration on the top floor of a high-rise building over a period of one year.
- The percent of time that gust speeds are expected a given value in a pedestrian plaza

To tackle these types of problem knowledge of the theory of probability and statistic is needed. However, for practical applications a few basic tools are very helpful, as well as some understanding of the thought processes that have led to some of the important results.

The interest is concentrated on the extreme value, or peak factor, so we couldn't analyze data only looking to normal or Gaussian distribution. The new distributions to know are

the extreme value distributions. In many cases in civil engineering we are interested in rare extreme events. In statistical language this means that we need to answer the question: what is the probability that all of m samples from a parent population are less than X. For example, if we have wind records for 50 years and we separate out the highest recorded speed from each year (m=50), what is the probability that all will be less than X. We can call this probability Pm(X). If we imagine repeating the process and determining the probability of not exceeding X in either of two collections of m samples each, it would be Pm(X)2. If it were repeated n times the probability of none od the mn examples exceeding X would be Pm(X)n. But we also can say that this probability must be the same as given by the function P for mn samples rather than n, i.e. by Pmn(x) but with the value of x shifted or rescaled as illustrated in Fig… Fisher and Tippet argued that the limiting form of the probability for extreme values could be deduced from the functional relationship

$$P(x)^n = P(a_n x + b_n)$$

Where an and bn are constants.

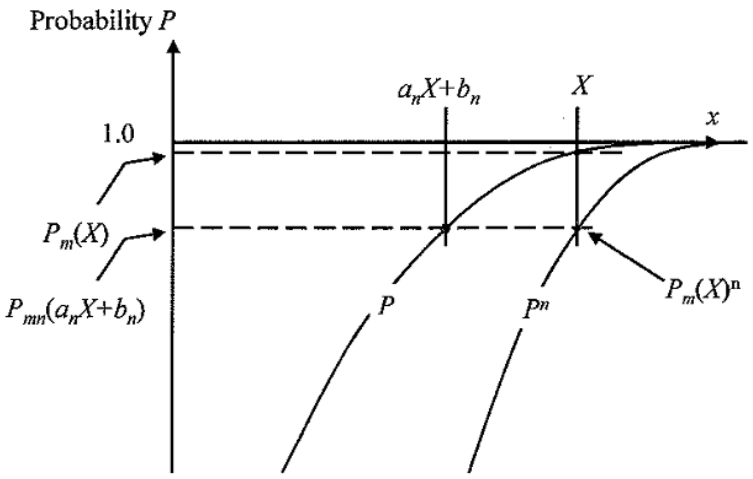

Figure 51 - Asymptotic behavior of probability of extremes

From this they concluded there are three possible limiting forms, one for an=1 and two others for an not equal to 11. The Fisher Tippet Type I form follows form the assumption that an=1, ie. That the matching of the values of Pn with P occurs through a simple shifting of the value of x by the constant bn, and is

$$P(X) = e^{-e^{-a(X-U)}}$$

Where a and U are constants, 1/a being called the dispersion and U being the mode of distribution. This equation is also often called the Gumbel distribution after Gumbel, who wrote extensively on extree value theory. Since P(X) is the probability of X not being exceeded, the probability Q(X) of X being exceeded is

$$Q(X) = 1 - P(X) = 1 - e^{-e^{-a(X-U)}}$$

The probability density is

$$p(X) = ae^{-y}e^{-e^{-y}} \; con \; y = a(X-U)$$

Figure 52 shows this function plotted for a=1.

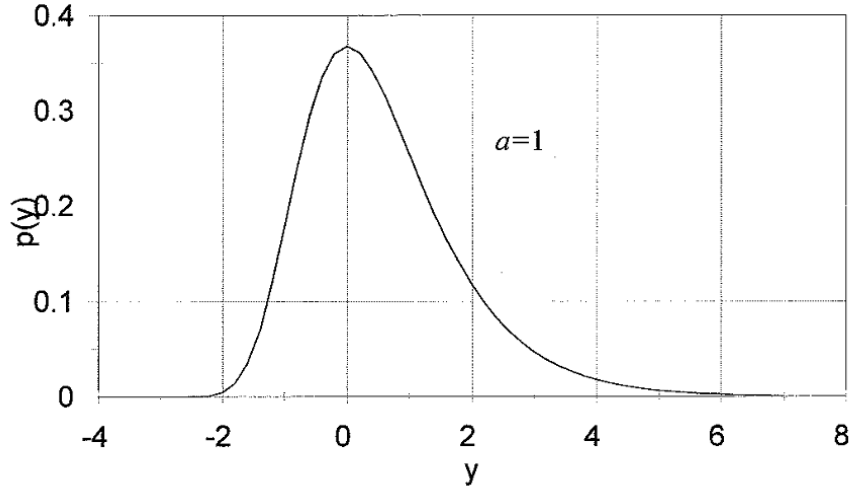

Figure 52 - Probability density of Fisher Tippet Type I distribution

There is also the Fisher Tippet Type II, but we'll only focus on Type I.

The return period T of wind velocity X is defined in terms of the probability Q(X) of the velocity X being exceeded in a particular year.

$$T = \frac{1}{Q(X)}$$

Thus if Q= 0,02 then T=50 years. Since P(X)=1-Q(X) we can also deduce that

$$P(X) = 1 - \frac{1}{T}$$

Therefore, assuming the Fisher Tippet Type I distribution applies and that we have determined the values of a and U for that distribution we can calculate the wind velocity V for any selected return period from

$$V = U - \frac{1}{a}\ln\left(-\ln\left(1 - \frac{1}{T}\right)\right.$$

4.5.3 Fitting the Fisher Tippet Type I

An example of fitting the Fisher Tippet Type I distribution is given in Table I. it shows the annual highest gust wind speeds measured at Conception, Chile over a period of 18 years. The values of wind speed have been ordered from lowest to highest and an estimate of the probability P(V) has been made by dividing the order number m by (M+1), where M is the total number of records (48 in this case). Then-ln(-lnP) has been computed. Finally a straight line is fitted to the plot of wind speed versus data –ln(-lnP) in order to evaluate U and a the line was fitted using least squares regression, with V as the dependent variable and –ln(-lnP) as the independent variable, and the values U=48,9 knots and 1/a=6,15 knots were obtained. The 50 year wind speed can be found from using the equation with T=50. Since –ln(-ln(1-1(50))=3,902 we can calculate that the 50-year-return-period wind speed is 48,9+6,15*3,902=72,8knots.

The use of least squares regression has been criticized because it places equal weight on all the extreme wind data, yet the accuracy of the estimate of probability has increasing uncertainty as order number increases. Therefore, Leibein, based on placing different weights that depend on the level of uncertainty, has proposed improved fitting methods. There are considerable other uncertainties in wind records, including spurious readings from faulty instrumentation or human error, and in the end some judgment is required as to what is the best way of fitting the data. It has been argued by Cook that ii is better to fit Type I distribution to wind speed squared rather than to wind speed, on the basis that the approach of the probability distribution of the extremes is faster in theory for pressures rather than velocities. It is true that quite often a better looking fit to Type I is obtained for pressures, but not always. Therefore again engineering judgment is required in deciding which fit to use.

4.6 Background

What is the topic which will be explained in this thesis, it is just been introduced. About pressures and suctions on buildings, in literature manifold papers exist about effects on roofs and cladding in general. About those, it is necessary to quote this paper: “Effect of roof-edge parapets on mitigating extreme roof suctions” (2010), written by Wimal Suaris and Peter Irwin; in this text there is a precise, full of details and update elaboration of the study of pressures on a low-rise building. It is referred to previous text made by Banks (2000), Baskaran and Stathopoulos (1988), Cheung et al. (1997), Ho et al. (2004), Holmes (2007). Irwin and al. (1979), Kopp et al. (2005), Surry and Lin (1995) and Wu (2000). All these and other articles are used to explain better the background and the contemporary researches about this topic.

At first it is important to underline that the researches on high-intermediate buildings are insufficient; so to understand the study of pressure it is useful to refer to low-rise buildings because of their rigidity. Also because, as we have said before, the main problem for high building is not the peak pressure, but vibrations and displacements. In this section, we try to have an overview on the background literature about peak pressure on roof (mainly corner zone), edge and ridge, the most critical zones.

Other deciding papers in the study which is being carried out, are several research works of Texas Tech University about the comparison between full-scale and model-scale (1:50 and 1:100) and they started at the end of the eighties. The conclusions of one of this paper (1992) are very interesting and they say that the coherence between full and scale model is guaranteed for taps centrally located, lots of differences could be noticed for edge and corner tap data (model study underestimates the extreme peak suctions by up to a factor of two, considering the most critical wind direction). This paper ends with this three questions: do the higher frequency vortex flows and separated shear layers play a more significant role in the full-scale than is being modeled in the wind-tunnel? Is the high frequency response of the pressure tubing systems currently in use really essential? The wind tunnel is deficient in transverse flow fluctuation (i.e., the

magnitude of azimuth fluctuations). Will active vertical vanes improve the extreme pressure data?

During the same years, another paper said that the first reliable full-scale data provide interesting comparison. For winds nearly normal to the ridge, the model and full-scale data are in very good agreement, particularly when their differing frequency responses are accounted for on the magnitudes of peaks. For winds oblique to the ridge, the data indicate significant differences in the peak coefficients, although this may be attributable to markedly different gust-to-mean ratios in these storms or to non-stationarity. Extensive comparisons, including wind and pressure spectra, will be made in the future, as more full-scale data become available.

It is interesting to find out the best link between the wind tunnel-test and CFD programs. In the following paper, referred to the same group of researchers, there are some suggestions for the way of meshing. The large-scale structures of the roof corner vortex generated by a quartering wind over the TTU building are resolved successfully. The mean values generally agree well with the wind-tunnel data and field test. By applying three different mesh sizes, which represent three-level filter scales, it is found that finer fluctuations can be resolved with a finer mesh system. Since only the resolvable values can be obtained in the computation, it is difficult to compare the computed pressure fluctuations with wind tunnel and field data. However, the computed results show that if the mesh is fine enough, the resolvable solution could catch all scale levels of the fluctuating eddies and the computation will be closer to the wind-tunnel and field test data. It would be interesting to try to use a grid size comparable to the size of measuring instruments and compare the results on equal size basis.

This paper describe in detail the analysis of the suctions in the corner area. In comparison with the results found by other investigators for a comparable model configurations, the agreement is generally good in the inner area if the approaching flow characteristics are similar, but there are still not sufficient data from different laboratories for comparison for the extreme corner area. Here, arguing that the

characteristic length for normalizing the roof coordinates, x and y, should be the height, H, the pressure distribution Cp(x/H,y/H) over the corner area is studied in detail. For all the models investigated, of varying height and planform, and in two types of flow, a radial pattern of pressure distribution induced by vortices emanating from the windward corner is observable for cornering winds. Suction are very high near the corner and decrease rapidly with the distance from the corner. A pressure distribution and its variation with the angle are described. It is shown that the area-averaged suctions significantly decrease with increasing averaging area embracing the corner since the extreme high suctions are very localized in the corner region.

Going deeply into the analysis and studying the reliability of scale model test, there are some studies about it, comparing different scale model with full scale.

The results of the full scale model are compared with those from the wind tunnel flow simulations at a geometric ratio of 1/50. The four simulations were achieved with the standard spire-roughness method and with three modifications of this technique. The final evaluation of each simulation is based on full/model-scale comparison of the extreme suction pressures observed on the roof near the leading edge for normal and oblique angles of attack. At the end, the CSU RII simulation, which included the addition of inclined horizontal vanes far upstream of the model location, achieved better duplication of the turbulent stress distribution and closer geometric scaling of streamwise turbulent integral scale, while apparently being deficient in the small-scale turbulence content. Based on these results all indications are that flow simulations for the purpose of predicting winds loads on roofs should pay special attention to the duplication of the turbulence intensities of the horizontal velocity components and their small-scale content.

The last papers presented are attempts to solve the discrepancies between model scale and reality, but just before the studies of TTU, it could be possible to focus on this problem highlighting that the problem is in the way of creating turbulence in the tunnel. The generation of large negative peak pressures in separated/reattaching flows is related

to an unstable process involving the intermittent roll-up of separated shear layers. The magnitude of these negative peaks increases with sigmau/usegnato and Lx/D. The results demonstrate the need to accurately model turbulence levels when conducting wind tunnel studies of surface pressures on buildings.

The problem of reproduce the turbulent flow in the wind tunnel is the main problem and every papers try to find out what is the way to have better results. Recent experiments have revealed that the standard spire-roughness technique for simulation of the incident flow and the resulting extreme pressures is still inadequate. These discrepancies are attributed to the inadequate simulation of the lateral velocity fluctuations and of the small-scale turbulence intensity for both the streamwise and lateral turbulence components. Therefore, a new technique is introduced whereby small spires are placed directly upstream of the model location. Preliminary results of these experiments are quite encouraging considering the simulation if the extreme corner pressures. However, additional investigation of the incident turbulence will be required to assess more definitely the effect of the increased lateral intensity and the increased small-scale turbulence on these pressure distributions. At the end: better simulation of the lateral turbulence intensity and small-scale turbulence has lead to a reduction of the discrepancies between the model and the full-scale pressure coefficients along the edges and near the corners

Concluding remarks of another paper is interesting and lead to the same conclusion. Modeling a thick ASL (atmospheric surface layer) in a boundary-layer wind tunnel has been made possible ly insertion of two sets of horizontal vanes at the test-section entrance. Mean wind speed and turbulence intensity distributions in the modeled ASL are in good agreement with corresponding data measured at the TTU field site when the model scale is taken to be 1:100. Integral length scales of the longitudinal turbulence component for the modeled ASL agree with field-site scales up to a height of about 20 m.

In the last ten years other studies have been carried on, and what before was a hypothesis, now it is more clear and there are conclusions confirmed by lots of experiments. It is interesting also making a comparison with the ASCE 7-02 specifications, as we'll do in the wind tunnel test. Comparisons with full scale TTU data show that the wind tunnel tests match the full-scale reasonably well, but cannot reproduce the largest of the peak point suctions near roof edges. (…) it is found that the wind tunnel simulation cannot reproduce the larger rms and peak values for taps near the edges of the roof. This finding is consistent with earlier comparisons between full scale and model test results of the TTU building. It is encouraging that the wind tunnel simulation is able to envelope the lower range of the full-scale data however. The comparison between the current data set and the ASCE 7-02 specifications suggests that the ASCE point pressure specifications may be lower, while the area loads match well for the lower eaves heights.

Another way is to change the Reynolds number. Wind-tunnel tests on a large (1/10 scale model of the Texas Tech experimental building have been described. The mean and RMS pressure coefficients obtained from the model for critical corner tappings for oblique wind directions, are in excellent agreement with the corresponding full-scale values. The largest minimum pressure coefficients for these tappings are approximately 20% less in magnitude than the corresponding full-scale values. However, this is a considerable improvement from previous wind-tunnel tests at smaller geometric scaling ratios (1/100 scale), in which no artificial increase in the longitudinal turbulence intensity was made. The increased Reynolds number for the present test series in believed to play a significant part in the greatly improved agreement obtained. The present results reinforce the good agreement obtained elsewhere when large-scale models have been used.

5 Particle Image Velocimetry (PIV) Analysis

Particle image velocimetry (PIV) is an optical method that has developed in the last 20 years. It consist of fluid visualization and it is very well known in research. This technique can provide an accurate quantitative measure of the instantaneous flow velocity and related properties field across a planar area of a flow field.

The fluid is seeded with tiny, neutrally buoyant particles – so called “tracers” – e.g. oil or water aerosols in air and solid particles in fluid or flames which, for the purposes of PIV, are generally assumed to faithfully follow the flow dynamics. It is the motion of these seeding particles that is used to calculate velocity information of the flow being studied.

Using a light sheet, formed by passing a double pulsed laser beam through an optical arrangement including cylindrical lenses, the particles in the flow are illuminated twice with a small time separation between. The displacement of particles in the time between the laser pulses is recorded as wither a single image exposed twice or as a pair of two single exposure images. The recorded particle displacement field is measured locally across the whole field of view of the images, scaled by the image magnification and then divided by the know pulse separation to obtain flow velocity at each point. A camera positioned typically perpendicular to the plane of the light sheet is shuttered to capture the light scattered from the particles. Depending on the flow velocity and the factor of magnification of the camera lens the delay of the two pulses have to be chosen such that adequate displacements of the particle images on the CCD are obtained. From the time delay between the two illuminations and the displacement of the tracers velocity vectors can be calculated (Figure 53).

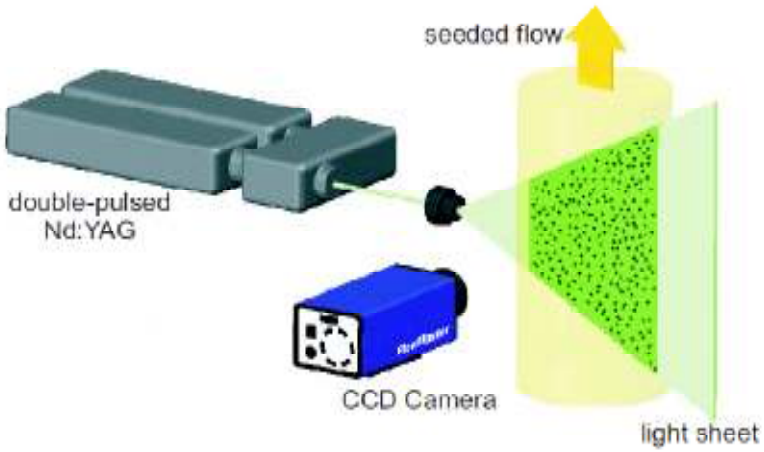

Figure 53 - Setup of a 2D PIV system

For the evaluation of the particle images it is assumed that the tracers follow the flow into the local flow velocity between the two illuminations. The (digital) PIV recording is divided in small subareas – so called "interrogation windows". Using statistical correlation techniques one local displacement vector is determined for each interrogation window. For this reason the size of the interrogation cell is selected such that all particles within this area have moved homogeneously in the same direction and the same distance. For good results the number of particles within one interrogation cell should be at least ten.

The evaluation of the particle images depends on the way these images have been recorded by the used camera. One possibility is to record the scattered light of both illuminations in one frame what is called "single frame/double exposure". These pictures can be evaluated by auto-correlation. The other possibility is to record the scattered light from the first illumination in one frame and the scattered light from the

second illumination in another frame. This is called “double frame / double exposure”. These double frame images can be evaluated by cross-correlation.

In the present work the “double frame / double exposure” options has been chosen.

5.1 Cross correlation (double frame / double exposure)

The scattered light from first and second exposure of the particles is recorded in two different images. The complete image is subdivided in interrogation windows and each window is evaluated by cross correlation (Figure 54).

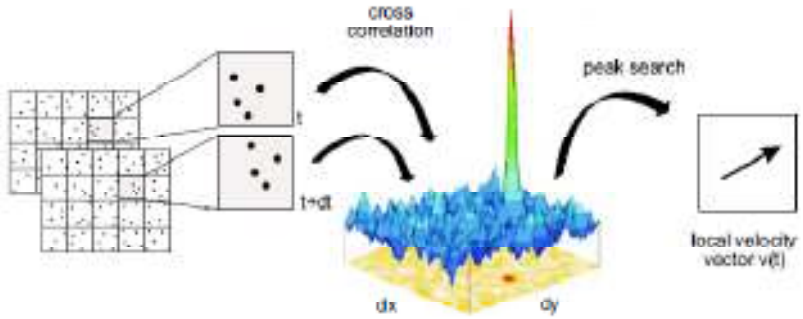

Figure 3.4: Evaluation of PIV recordings using Cross-Correlation

Figure 54 - Evaluation of PIV recordings using Cross-Correlation

5.2 Test

In the present work the aid given by the PIV is really important.

The main reason why is that the object of this work is a flow that has many separations and vortexes, therefore it is fundamental to be able to compare the results from the Wind Tunnel and from the CFD with a flow visualization that helps to understand the real behavior of the flow.

Of course, there are already many papers that describe the behavior of the flow of the wind around a cubic obstacle, but none of them deepen in the detailed behavior at the corner zones. Anyway, those papers have been really useful to start the test with an idea of what to expect.

The simulation has been done in the Wind Tunnel of the University of Miami, Dept. of Mechanical Engineering, under the supervision of PhD Professor Bertrand Dano.

5.3 Set Up

The experiment has been done using a scale model of a cubic building, with a smaller scale than the one used for the Wind Tunnel test in Miramar. The model was built using the same procedure as described earlier in Chapter 3. To help the software to visualize the particles, the cube was painted with black acrylic.

This smaller model had a scale of 1:150, with a 8inches (0.2 meters) edge length. The wind tunnel was set up with an inlet wind speed of 10 m/s.

The model was placed in the Wind Tunnel fixing it to a side of the tunnel so that it was possible to choose different angles thanks to a circular rotating panel (Figure 55). The precision was guaranteed thanks to an electronic level placed on the top of the model before every test.

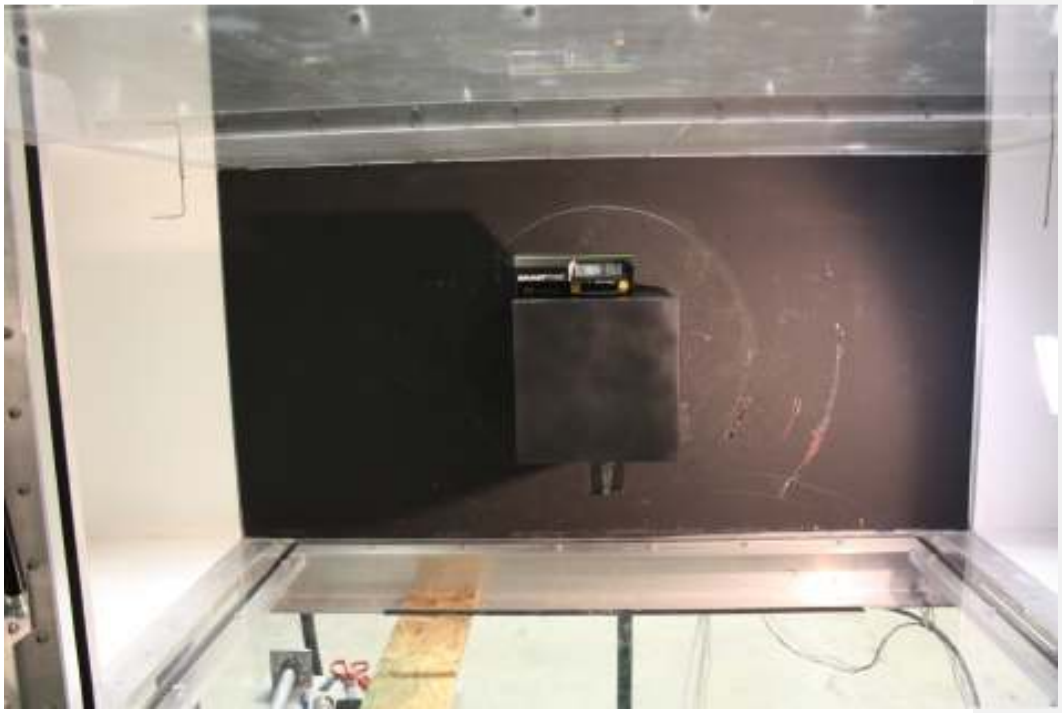

Figure 55 - A cube model set down in the small wind tunnel for the PIV study

5.4 Calibration

After a few tests done just to depict the most interesting planes to monitor, a calibration was run before the proper test. For the spatial calibration of a camera image the known separation between points in the object plane have to be specified ()Figure 56.

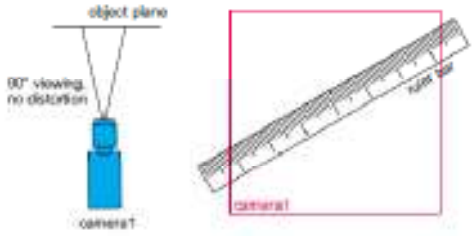

Figure 56 - Calibration

For the present test a linear calibration was run, simply using a ruler bar in the corresponding distance to the camera. The linear scaling can be used in this case because the camera viewing was perpendicular to the object plane and there was no image distortion (Figure 57).

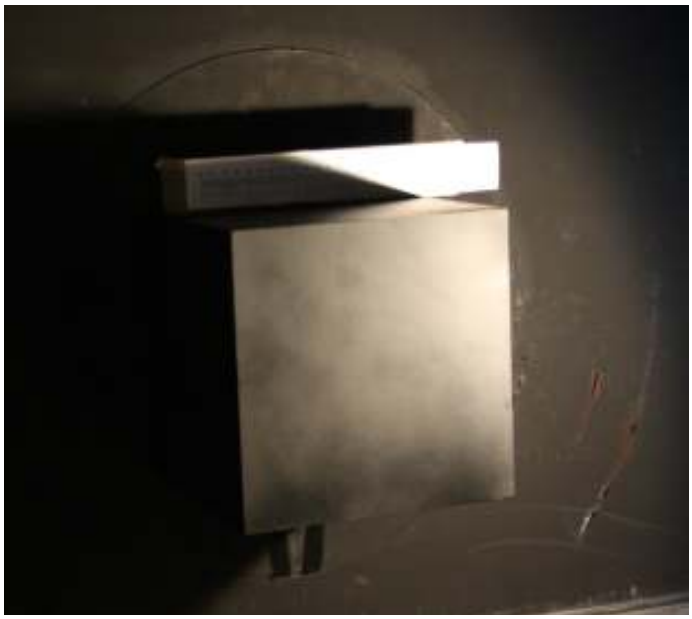

Figure 57 - Calibration during the PIV test

5.5 Measurements

Unfortunately in this Wind Tunnel it was not possible to represent the boundary layer. Anyway the data can still be useful for the porpoise of this work. The pattern of the flow, in fact, is really complex and tough to predict. This is the reason why a test like this is really helpful to be more aware of the behavior of the wind, in particular in relation with suctions and vortexes, even if only from a qualitative point of view.

Moreover, it is good to notice that in the Wind Tunnel Test in Miramar was chosen a profile with a really low roughness: supposing that the profile of the wind was comparable with the ASCE profiles it would mean that the test profile had an equivalent roughness of z_0=0.0012. This roughness is really low, therefore, still being aware of the fact that it was not possible to develop any kind of boundary layer, the difference is still low enough to appreciate the data.

During the test the room was completely obscured to allow the camera to take all the pictures in the best conditions of contrast. For the present test a LaVision Digital Particle Image Velocimetry (DPIV) system with a Litron Nano Nd:YAG was used to monitor and acquire the velocity field surrounding the box.

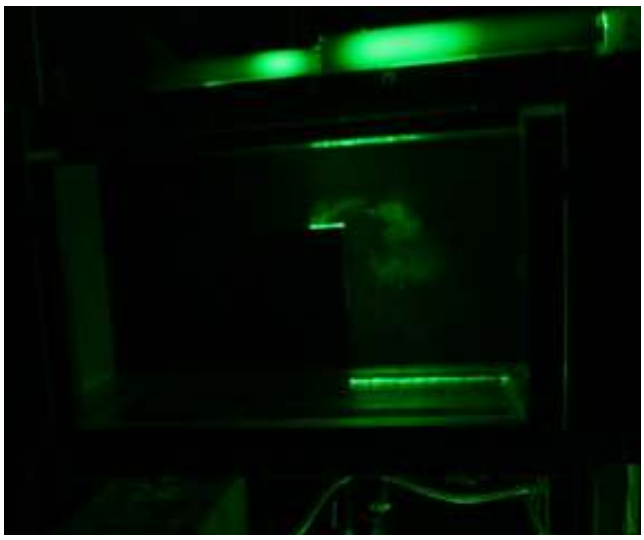

Figure 58 - Running the PIV test

For every test 50 pictures were taken at a frequency of 200 mJ/pulse (Figure 58). 18 tests were carried out to map the behavior of the wind from every direction. After the acquisition of the data, run with the aid of DaVis 7.1, analysis were carried out with the aid of a MatLab code that allowed to calculate the mean flow velocity, the vorticity and the turbulent kinetic energy.

PIV produces two dimensional vector fields, therefore it was chosen to monitor the particle flow at a certain height for a plane parallel to the floor. A plane at ¾ of the height of the building was chosen because it is close enough to the roof to be able to show the effects of the vortices and it is not too close to the roof where the 3D effects causes the PIV to be difficult to interpret.

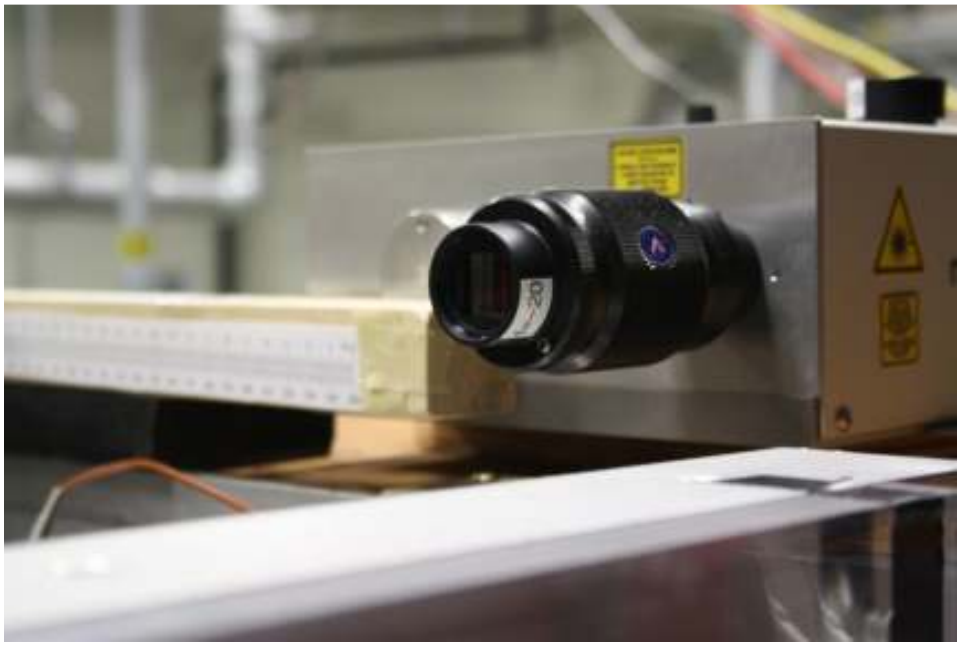

Figure 59 - Laser device

An adaptive 32x32 to 16x16 pixel with 0% overlap cross-correlation analysis method was used. Of course, it is necessary not to take into account the parts of the picture with the building: to do this it is enough to mask the building over. A median filter for post processing was used. A customized flow seeder using the same particles for PIV tracers was used for flow visualization.

5.6 Analysis

The data processing was done with a very useful software by Lavision was used. Thanks to some particular Matlab functions, moreover, it is also possible to run the analysis without the Lavision software, calculating all the necessary values. In particular it is possible to draw velicity fields, intensity of turbulence, and turbulent kinetic energy. With some other Matlab functions it is also useful to draw streamlines.

6 Computational Wind Engineering

6.1 Introduction

Computational wind engineering (CWE), as a branch of Computational Fluid Dynamics (CFD), has been developed rapidly over the last three decades to evaluate the interaction between wind and structures numerically. It has become one of the most important application fields for researchers on CFD, where numerical models are specially designed to simulate wind effects over civil structures, such as long-span bridges and buildings. The determination of such effects has been traditionally performed using experimental techniques developed in wind tunnels to reproduce natural wind flows, since analytical models are unable to describe complex problems accurately. However, with the increasing advance in computer technology and the great reliability reached by the present numerical methods, numerical simulation has become a very attractive way to analyze wind engineering problems.

The potential of the CWE is out of any doubt, but today it is still really important to be also aware of the risks. Any Computational Fluid Dynamic program, in fact, gives results that cannot be taken for true beforehand. All the results obviously rely on the models that are behind them and on the capabilities of the calculators.

All the CFD analysis are performed by means of the following steps:

1) Definition of the physical problem
   - Basic equations
   - Turbulence models
2) Definition of the computational domain
   - Domain size
   - Geometrical representation of details
   - Boundary conditions
3) Definition of the computational grid
4) Definition of the numerical approximations
5) Solution
   - Iterative convergence

- Grid dependence of the solution

In time researchers developed many different theories and models to be applied with the aid of the computers. Today there are different techniques for practical applications: in this work we will focus mainly on two of them: the Reynolds Averaged Navier-Stokes Equations (RANS) Model, and the Large Eddy Simulations (LES).

6.2 Equations and theory of fluids

The fundamental basis of almost all CFD problems are the Navier–Stokes equations, which define any single-phase fluid flow.

Those equations represent mathematical statements of the conservation laws of physics:

- The mass of a fluid is conserved
- The rate of change of momentum equals the sum of the forces on a fluid particle (Newton's second law)
- The rate of change of energy is equal to the sum of the rate of heat addition to and the rate of work done on a fluid particle (first law of thermodynamics)

The fluid will be regarded as a continuum and his behavior will be described in terms of macroscopic properties (velocity, pressure, density and temperature) and their space and time derivatives.

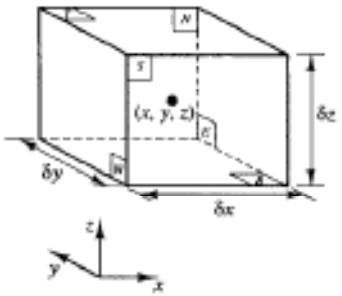

Figure 60 - Fluid element for conservation laws

The complete mathematical procedure used to obtain the equations can be found on any Fluid Dynamic book, but it has been chosen to go back over the fundamental steps leading to the equations.

6.2.1 Mass conservation

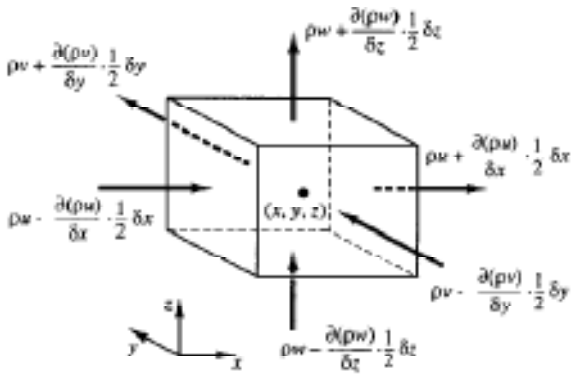

Figure 61 – Mass flows in and out of fluid element

The mass conservation leads to the following equilibrium:

Rate of increase of mass in fluid element	=	Net rate of flow of mass into fluid element

In three dimensions it yields to the following equation:

$$\frac{\partial \rho}{\partial t} + \frac{\partial (\rho u)}{\partial x} + \frac{\partial (\rho v)}{\partial y} + \frac{\partial (\rho w)}{\partial z} = 0 \qquad (6.1)$$

Or in more compact vector notation:

$$\frac{\partial \rho}{\partial t} + div(\rho \mathbf{u}) = 0 \quad (6.2)$$

that is the unsteady, three-dimensional mass conservation or continuity equation at a point in a compressible fluid.

6.2.2 Momentum conservation

Newton's second law states that

Rate of change of momentum of fluid particle	=	Sum of forces on fluid particle

The balance of forces in the x-direction on the elemental volume of the fluid can be easily understood considering the following figure (Figure 62):

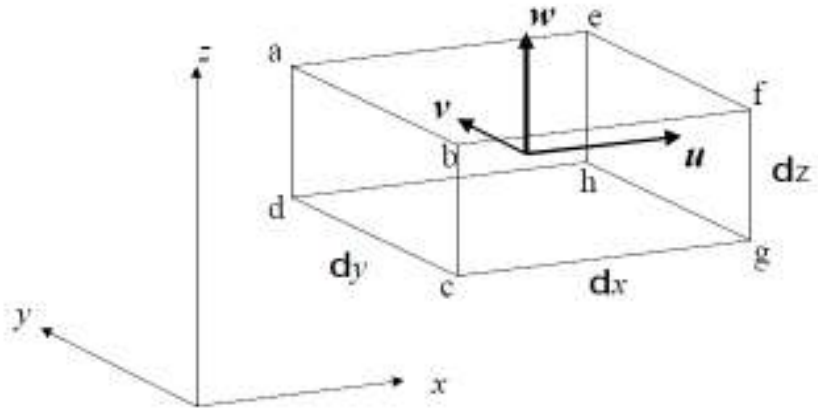

Figure 62 - Fluid element for momentum conservation

The net force in the x-direction caused by the difference in the pressure on the faces *abcd* and *efgh* is equal to:

Force due to pressure$= -\frac{\partial p}{\partial x}\delta x\delta y\delta z$ (6.3)

The rate of change in momentum will be also given by the flow of momentum bearing air across the surfaces of the volume. Considering again the x-direction the mass flow of air across the surface *abcd* is given by $\rho_1 u_1 \delta y\delta z$ where u_1 is the average x-component velocity across *abcd*, ρ_1 is the average density and each unit of mass has x-momentum u_1. Therefore the flow rate of x-momentum across *abcd* will be $\rho_1 u_1^2 \delta y\delta z$. Similarly the outflow rate of x-momentum across *efgh* will be $\rho_2 u_2^2 \delta y\delta z$.

The net flow of x-momentum across the volume will be given by

$(\rho_1 u_1^2 - \rho_2 u_2^2)\delta y\delta z$ (6.4)

This can be expresses as

$(\rho_1 u_1^2 - \rho_2 u_2^2)\delta y\delta z = \frac{\partial \rho u^2}{\partial x}\delta x\delta y\delta z$ (6.5a)

Similar analysis can be done for the other faces, obtaining:

$(\rho_1 u_1 w_1 - \rho_2 u_2 w_2)\delta x\delta y = \frac{\partial \rho uw}{\partial z}\delta x\delta y\delta z$ (6.5b)

and

$(\rho_1 u_1 v_1 - \rho_2 u_2 v_2)\delta x\delta z = \frac{\partial \rho uv}{\partial y}\delta x\delta y\delta z$ (6.5c)

Finally, the total rate of change of momentum for the considered volume is given by:

$\frac{\partial \rho u}{\partial t}\delta x\delta y\delta z$ (6.6)

It is now possible to combine those equations, yielding to:

$$\frac{\partial \rho u}{\partial t}\delta x\delta y\delta z = -\frac{\partial p}{\partial x}\delta x\delta y\delta z - \frac{\partial \rho u^2}{\partial x}\delta x\delta y\delta z - \frac{\partial \rho uv}{\partial y}\delta x\delta y\delta z - \frac{\partial \rho uw}{\partial z}\delta x\delta y\delta z$$

or

(6.7)

$$\frac{\partial \rho u}{\partial t} + \frac{\partial \rho u^2}{\partial x} + \frac{\partial \rho uv}{\partial y} + \frac{\partial \rho uw}{\partial z} = -\frac{\partial p}{\partial x}$$

Total rate of change of x-momentum	=	Pressure	+	Net inflows of x-

6.2.3 Rate of change of Energy

The energy equation is derived from the firs law of thermodynamics which states that the rate of change of a fluid particle is equal to the rate of heat addition to the fluid particle plus the rate of work done on the particle.

Rate of increase of energy fluid particle	=	Net rate of heat added to fluid particle	+	Net rate of work on fluid particle

The equations, not necessary for the present case, can be found on Versteeg and Malalasekera (1995).

6.2.4 Further hypothesis

Some physical assumptions concerning the fluid/flow behavior are now introduced. In the field of CWE wind flows are usually characterized with the following assumptions:

1- Natural wind streams are considered to be within the incompressible flow range
2- Natural wind streams are considered to be within the turbulent flow range
3- Wind is always flowing with constant temperature (isothermal process)
4- Gravity forces are neglected in the fluid field
5- Air is considered mechanically as a Newtonian fluid
6-

Mass Equation:

Referring to the first statement in wind engineering the velocity of air remains a small fraction of the speed of sound and the compressibility of the air has negligible effect on airflows as long as the velocity remains below about one third of the speed of sound. This implies that in wind engineering the air density ρ can for practical purposes be treated as a constant at any given elevation.

Therefore the Eq. 6.1 reduces to

$$div\ \mathbf{u} = 0 \qquad (6.8)$$

Or in longhand notation

$$\frac{\partial u}{\partial x} + \frac{\partial v}{\partial y} + \frac{\partial w}{\partial z} = 0 \qquad (6.9)$$

6.2.5 Momentum equation

Moreover, also the equation obtained from the momentum equations can be simplified as follow:

$$\frac{\partial u}{\partial t} + \frac{\partial u^2}{\partial x} + \frac{\partial uv}{\partial y} + \frac{\partial uw}{\partial y} = -\frac{1}{\rho}\frac{\partial p}{\partial x} \qquad (6.10)$$

The term $\frac{\partial u^2}{\partial x}$ can be written as $2u\frac{\partial u}{\partial x}$. Also $\frac{\partial uv}{\partial y} = u\frac{\partial v}{\partial y} + v\frac{\partial u}{\partial y}$ and $\frac{\partial uw}{\partial z} = u\frac{\partial w}{\partial z} + w\frac{\partial u}{\partial z}$.

Substituting these into Eq. 6.9 it is possible to obtain

$$\frac{\partial u}{\partial t} + u\frac{\partial u}{\partial x} + v\frac{\partial u}{\partial y} + w\frac{\partial u}{\partial z} + u\left(\frac{\partial u}{\partial x} + \frac{\partial v}{\partial y} + \frac{\partial w}{\partial z}\right) = -\frac{1}{\rho}\frac{\partial p}{\partial x} \qquad (6.11)$$

We see that the term in the brackets on the left hand side is zero by the continuity relationship, Eq. 6.9. Thus the x-momentum equation becomes

$$\frac{\partial u}{\partial t} + u\frac{\partial u}{\partial x} + v\frac{\partial u}{\partial y} + w\frac{\partial u}{\partial z} = -\frac{1}{\rho}\frac{\partial p}{\partial x} \qquad (6.12a)$$

Similarly the y-momentum and z-momentum equations can be shown to be

$$\frac{\partial v}{\partial t} + u\frac{\partial v}{\partial x} + v\frac{\partial v}{\partial y} + w\frac{\partial v}{\partial z} = -\frac{1}{\rho}\frac{\partial p}{\partial y} \quad (6.12b)$$

$$\frac{\partial w}{\partial t} + u\frac{\partial w}{\partial x} + v\frac{\partial w}{\partial y} + w\frac{\partial w}{\partial z} = -\frac{1}{\rho}\frac{\partial p}{\partial z} \quad (6.12c)$$

6.2.6 Shear stress term

In wind engineering it is really important to be able to describe turbulences. In fact in air, viscosity gives rise to shear stresses in turbulences and those terms have a very significant effect.

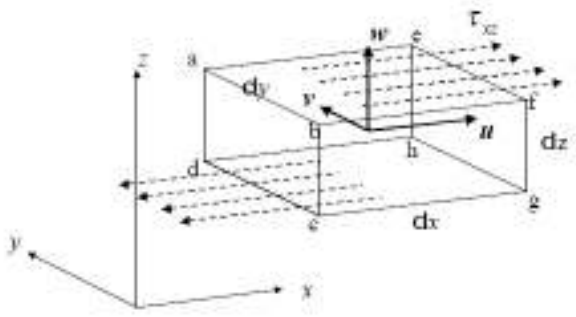

Figure 63 - Inclusion of shear stress term

Considering Figure 63 when a fluid parcel undergoes a shearing deformation, in which the fluid at surface *aefb* moves in the x-direction relative to the fluid at surface *dhgc*, this causes a shear stress in the x-direction on a plane normal to the z-direction. This shear stress will be denoted by τ_{xz} . Likewise, for shear deformations in which the fluid at surface *aehd* moves in the x-direction relative to the fluid at surface *bfgc*, there is a shear stress in the x-direction on a plane normal to the y-drection. This is denoted by τ_{xy}. Also, when the fluid parcel undergoes a rate of extension in the x-direction, this

causes a normal stress τ_{xx} on a plane normal to the x-direction. The net force on the volume element in Figure 63 due to these deformation related stresses is

$$\text{Net x-direction force} = \frac{\partial \tau_{xx}}{\partial x}\delta x\delta y\delta z + \frac{\partial \tau_{xz}}{\partial z}\delta x\delta y\delta z + \frac{\partial \tau_{xy}}{\partial y}\delta x\delta y\delta z \qquad (6.13)$$

Hence the x-momentum equation, Eq. 6.12a, becomes

$$\frac{\partial u}{\partial t} + u\frac{\partial u}{\partial x} + v\frac{\partial u}{\partial y} + w\frac{\partial u}{\partial z} - vf = -\frac{1}{\rho}\frac{\partial p}{\partial x} + \frac{1}{\rho}\frac{\partial \tau_{xx}}{\partial x} + \frac{1}{\rho}\frac{\partial \tau_{xy}}{\partial y} + \frac{1}{\rho}\frac{\partial \tau_{xz}}{\partial z} \quad (6.14a)$$

Similarly Eqs. 6.12b and 6.12c become

$$\frac{\partial v}{\partial t} + u\frac{\partial v}{\partial x} + v\frac{\partial v}{\partial y} + w\frac{\partial v}{\partial z} + uf = -\frac{1}{\rho}\frac{\partial p}{\partial y} + \frac{1}{\rho}\frac{\partial \tau_{yx}}{\partial x} + \frac{1}{\rho}\frac{\partial \tau_{yy}}{\partial y} + \frac{1}{\rho}\frac{\partial \tau_{yz}}{\partial z} \quad (6.14b)$$

and

$$\frac{\partial w}{\partial t} + u\frac{\partial w}{\partial x} + v\frac{\partial w}{\partial y} + w\frac{\partial w}{\partial z} = -\frac{1}{\rho}\frac{\partial p}{\partial z} + \frac{1}{\rho}\frac{\partial \tau_{zx}}{\partial x} + \frac{1}{\rho}\frac{\partial \tau_{zy}}{\partial y} + \frac{1}{\rho}\frac{\partial \tau_{zz}}{\partial z} \qquad (6.14c)$$

6.2.7 Viscous effect

The air, in common with other gases and fluids, is viscous and the viscosity gives rise to stresses when there is a rate of deformation of fluid particles. Fluids differ from solids in that the deformation-related stresses depend on rate of deformation, rather than the deformation itself.

The governing equations contain as further unknowns the viscous stress components τ_{ij}. The most useful forms of the conservation equations for fluid flows are obtained by introducing a suitable model for the viscous stresses τ_{ij}. In three-dimensional flows the local rate of deformation is composed of the linear deformation rate and the volumetric deformation rate.

The rate of linear deformations are denoted by the symbol e_{ij}. There are three linear elongating deformation components

$$e_{xx} = \frac{\partial u}{\partial x}$$

$$e_{yy} = \frac{\partial v}{\partial y} \qquad (6.15)$$

$$e_{zz} = \frac{\partial w}{\partial z}$$

And six shearing linear deformation components

$$e_{xy} = e_{yx} = \frac{1}{2}\left(\frac{\partial u}{\partial y} + \frac{\partial v}{\partial x}\right)$$

$$e_{xz} = e_{zx} = \frac{1}{2}\left(\frac{\partial u}{\partial z} + \frac{\partial w}{\partial x}\right) \qquad (6.16)$$

$$e_{yz} = e_{zy} = \frac{1}{2}\left(\frac{\partial v}{\partial z} + \frac{\partial w}{\partial y}\right)$$

The rate of volumetric deformations is given by

$$\frac{\partial u}{\partial x} + \frac{\partial v}{\partial y} + \frac{\partial w}{\partial z} = div\ \mathbf{u} \qquad (6.17)$$

As mentioned, in a Newtonian fluid the viscous stresses are proportional to the rates of deformation. The three-dimensional form of Newton's law of viscosity for compressible flows involves two constants of proportionality: the dynamic viscosity of air μ (to relate stresses to linear deformation) and the second viscosity λ to relate stresses to the volumetric deformation.

The nine viscous stress components (only six of them are independent) are:

$$\tau_{xx} = 2\mu\frac{\partial u}{\partial x} + \lambda\ div\ \mathbf{u} \qquad (6.18a)$$

$$\tau_{yy} = 2\mu\frac{\partial v}{\partial y} + \lambda\ div\ \mathbf{u} \qquad (6.18b)$$

$$\tau_{zz} = 2\mu\frac{\partial w}{\partial z} + \lambda\ div\ \mathbf{u} \qquad (6.18c)$$

$$\tau_{xy} = \tau_{yx} = \mu\left(\frac{\partial u}{\partial y} + \frac{\partial v}{\partial x}\right) \qquad (6.18d)$$

$$\tau_{xz} = \tau_{zx} = \mu\left(\frac{\partial u}{\partial z} + \frac{\partial w}{\partial x}\right) \quad (6.18e)$$

$$\tau_{yz} = \tau_{zy} = \mu\left(\frac{\partial v}{\partial z} + \frac{\partial w}{\partial y}\right) \quad (6.18f)$$

For gases is generally considered $\lambda = 2/3\mu$ as a good approximation (Schlichting, 1979).

Since the stress terms involving τ_{ij} in Eqs. 6.14 all involve $1/\rho$ it is convenient also to use the kinematic viscosity ν, rather than the viscosity μ, and express the stress divided by the air density as

$$\frac{\tau_{ti}}{\rho} = \nu\left(\frac{\partial u_i}{\partial x_j} + \frac{\partial u_j}{\partial x_i}\right) \quad (6.19)$$

where

$$\nu = \frac{\mu}{\rho} \quad (6.20)$$

Substituting the viscous stress in the Eqs. 6.14, also using the continuity relationship, yields to:

$$\frac{\partial u}{\partial t} + u\frac{\partial u}{\partial x} + v\frac{\partial u}{\partial y} + w\frac{\partial u}{\partial z} = -\frac{1}{\rho}\frac{\partial p}{\partial x} + \nu\left(\frac{\partial^2 u}{\partial x^2} + \frac{\partial^2 u}{\partial y^2} + \frac{\partial^2 u}{\partial z^2}\right) \quad (6.21a)$$

$$\frac{\partial v}{\partial t} + u\frac{\partial v}{\partial x} + v\frac{\partial v}{\partial y} + w\frac{\partial v}{\partial z} = -\frac{1}{\rho}\frac{\partial p}{\partial y} + \nu\left(\frac{\partial^2 v}{\partial x^2} + \frac{\partial^2 v}{\partial y^2} + \frac{\partial^2 v}{\partial z^2}\right) \quad (6.21b)$$

$$\frac{\partial w}{\partial t} + u\frac{\partial w}{\partial x} + v\frac{\partial w}{\partial y} + w\frac{\partial w}{\partial z} = -\frac{1}{\rho}\frac{\partial p}{\partial z} + \nu\left(\frac{\partial^2 w}{\partial x^2} + \frac{\partial^2 w}{\partial y^2} + \frac{\partial^2 w}{\partial z^2}\right) \quad (6.21c)$$

These are the fundamental *Navier-Strokes* equations that govern nearly all the air motions of interest in wind engineering. The only effect missing are those due to thermal effects, moisture and heat transfer but, for most wind engineering applications these effects have only an indirect bearing on the problem at hand. The case of this study can be well described by those equations.

Those equations are really useful because they are able to describe the behavior of fluids, wind in particular, very well. Unfortunately, despite their wide range of practical uses, the existence and the smoothness of the three-dimensional solution has not been proven yet.

The reason of this problem is that the Navier-Stokes equations are nonlinear partial differential equations in almost every real situation.

One of the most difficult behavior to model is the turbulence, which is the time dependent chaotic behavior. The numerical solution of the Navier-Stokes equations for turbulent flows is very difficult, and the attempt to solve turbulent flow using a laminar solver typically result in a time unsteady solution, which fails to converge appropriately. To counter this, researchers have developed in time different types of equations, as the result of new models on the behavior of the wind.

6.2.8 RANS Reynolds-Averaged Navier-Stokes equations

For practical purposes, many times engineers need computational procedures which can supply adequate information about the turbulent processes, but which avoid the need to predict effects of each and every eddy in the flow. For this reason, it is common practice to be satisfied with information about the time-averaged properties of the flow. This approach makes the equation much more simple and the solution can be found.

The Navier-Stokes equations for an incompressible flow with constant viscosity, in their most compact form, are:

$$div\ \mathbf{u} = 0 \qquad (6.22)$$

$$\frac{\partial y}{\partial t} + div(u\mathbf{u}) = -\frac{1}{\rho}\frac{\partial p}{\partial x} + \nu\ div\ grad\ u \qquad (6.23a)$$

$$\frac{\partial v}{\partial t} + div(v\mathbf{u}) = -\frac{1}{\rho}\frac{\partial p}{\partial y} + \nu\ div\ grad\ v \qquad (6.23b)$$

$$\frac{\partial w}{\partial t} + div(w\mathbf{u}) = -\frac{1}{\rho}\frac{\partial p}{\partial z} + \nu\ div\ grad\ w \quad (6.23c)$$

To describe a turbulent flow it is useful to divide the flow variables $\mathbf{u}$ and p into the sum of a mean and a fluctuating component. The upper case symbols will denote the time-averaged values and the fluctuations will be denoted by the primed symbols.

$$\mathbf{u} = \mathbf{U} + \mathbf{u}' \quad (6.24a)$$

$$u = U + u' \quad (6.24b)$$

$$v = V + v' \quad (6.24c)$$

$$w = W + w' \quad (6.24d)$$

$$p = P + p' \quad (6.25)$$

Considering that by time-averaged we mean integration over time interval T followed by division by T, like

$$U = \frac{1}{T}\int_0^T u dt \quad (6.26)$$

By definition the derivatives

$$\frac{\partial U}{\partial t} = \frac{\partial V}{\partial t} = \frac{\partial W}{\partial t} = \frac{\partial P}{\partial t} = 0 \qquad (6.27)$$

And the time averaged of fluctuating parts are zero. Therefore

$$\frac{1}{T}\int_0^T u' dt = \frac{1}{T}\int_0^T v' dt = \frac{1}{T}\int_0^T w' dt = \frac{1}{T}\int_0^T p' dt = 0 \qquad (6.28)$$

Substituting Eqs. 6.24 for u, v, w in Eqs. 6.23, taking the time average and with the aid of Eqs. 6.27 and 6.28, one can obtain the following expressions

$$div(U\mathbf{U}) = -\frac{1}{\rho}\frac{\partial P}{\partial x} + \nu\ div\ grad\ U + \left[-\frac{\partial \overline{u'^2}}{\partial x} - \frac{\partial \overline{u'v'}}{\partial y} - \frac{\partial \overline{u'w'}}{\partial z}\right] \qquad (6.29a)$$

$$div(V\mathbf{U}) = -\frac{1}{\rho}\frac{\partial P}{\partial y} + \nu\ div\ grad\ V + \left[-\frac{\partial \overline{u'v'}}{\partial x} - \frac{\partial \overline{v'^2}}{\partial x} - \frac{\partial \overline{v'w'}}{\partial z}\right] \qquad (6.29b)$$

$$div(W\mathbf{U}) = -\frac{1}{\rho}\frac{\partial P}{\partial z} + \nu\, div\, grad\, W + \left[-\frac{\partial \overline{u'w'}}{\partial y} - \frac{\partial \overline{v'w'}}{\partial y} - \frac{\partial \overline{w'^2}}{\partial z}\right] \qquad (6.29c)$$

Al the passages necessary to obtain Eqs. 6.29 are not included for brevity, and are reported in Irwin

The time-average values are denoted in Eqs. 6.29 by the over-bar.

Examining the first of the three equations we see that the term $\partial\overline{u'^2}/\partial x$ is similar to changing the local mean pressure P by the amount of $\rho\overline{u'^2}$. Therefore $\partial\overline{u'^2}/\partial x$behaves like a pressure gradient term.

Comparing terms $\partial\overline{u'v'}/\partial y$ and $\partial\overline{u'w'}/\partial z$ in Eq. 6.29a above with Eq. 6.14a it can be seen that for the mean flow they are exactly like the shear stress terms $\frac{1}{\rho}\frac{\partial \tau_{xy}}{\partial y}$ and $\frac{1}{\rho}\frac{\partial \tau_{xz}}{\partial z}$.

They are therefore called the turbulence shear stress terms.

$\tau_{xx} = -\rho u'^2$ (6.30a)

$\tau_{yy} = -\rho v'^2$ (6.30b)

$\tau_{zz} = -\rho w'^2$ (6.30c)

$\tau_{xy} = \tau_{yx} = -\rho u'v'$ (6.30d)

$\tau_{xz} = \tau_{zx} = -\rho u'w'$ (6.30e)

$\tau_{yz} = \tau_{zy} = -\rho v'w'$ (6.30f)

Averaging the equations leads to throw away all details concerning the state of the flow contained in the instantaneous fluctuations. It can be noticed that this produces nine (six independent) additional unknowns that are extra turbulent stresses.

Those nine new terms are called Reynolds stresses.

6.3 Turbulence models

The previous discussion showed that the instantaneous continuity and Navier-Stokes equations, even in their averaged version, could not be solved directly. For this reason (closure problem) there is the need of turbulence modeling to develop computational procedures of sufficient accuracy and generality for engineers to predict the Reynolds stresses and the scalar transport terms.

6.3.1 Turbulence model: $k-\varepsilon$

In wind engineering there are many models for turbulences. Among the classical models, it has been recognized that the widely used standard $k-\varepsilon$ model can predict the general wind conditions reasonably well. This model is based on the presumption that there are analogies between the action of viscous stresses and Reynolds stresses on the mean flow.

We have already seen (Eqs. 6.18) that for an incompressible flow:

$$\tau_{ij} = \mu e_{ij} = \mu\left(\frac{\partial u_i}{\partial x_j} + \frac{\partial u_j}{\partial x_i}\right) \quad (6.31)$$

Boussinesq (1877) proposed that Reynold stresses could be related to mean rates of deformation:

$$\tau_{ij} = -\rho\overline{u'_i u'_j} = \mu_t\left(\frac{\partial U_i}{\partial x_j} + \frac{\partial U_j}{\partial x_i}\right) \quad (6.32)$$

μ_t=turbulent or eddy viscosity.

The $k-\varepsilon$ model focuses on the mechanism that affects the turbulent kinetic energy. It is useful to define the instantaneous kinetic energy as

$$k(t) = K + k \quad (6.33)$$

Considering that

$$K = \frac{1}{2}(U^2 + V^2 + W^2) \qquad (6.34)$$

and the turbulent kinetic energy

$$k = \frac{1}{2}(u^2 + v^2 + w^2) \qquad (6.35)$$

the components of the rate of deformation e_{ij} and the stresses τ_{ij} in tensor form:

$$e_{ij} = \begin{pmatrix} e_{xx} & e_{xy} & e_{xz} \\ e_{yx} & e_{yy} & e_{yz} \\ e_{zx} & e_{zy} & e_{zz} \end{pmatrix} \qquad (6.36)$$

and

$$e_{ij} = \begin{pmatrix} \tau_{xx} & \tau_{xy} & \tau_{xz} \\ \tau_{yx} & \tau_{yy} & \tau_{yz} \\ \tau_{zx} & \tau_{zy} & \tau_{zz} \end{pmatrix} \qquad (6.37)$$

As in the averaging process, it is possible to decompose the rate of deformation of a fluid element in a turbulent flow into a mean and a fluctuating component

$$e_{ij}(t) = E_{ij} + e'_{ij} \qquad (6.38)$$

After a fair amount of algebra it can be demonstrated that the time-average equation governing the mean kinetic energy of the flow is as follows (Tennekes and Lumley, 1972):

$$\frac{\partial(\rho K)}{\partial t} + div(\rho K \mathbf{U}) = div\left(-P\mathbf{U} + 2\mu \mathbf{U} E_{ij} - \rho \mathbf{U}\overline{u'_i u'_j}\right) - 2\mu E_{ij} \cdot E_{ij} + \rho \overline{u'_i u'_j} \cdot E_{ij} \qquad (6.39)$$

which means:

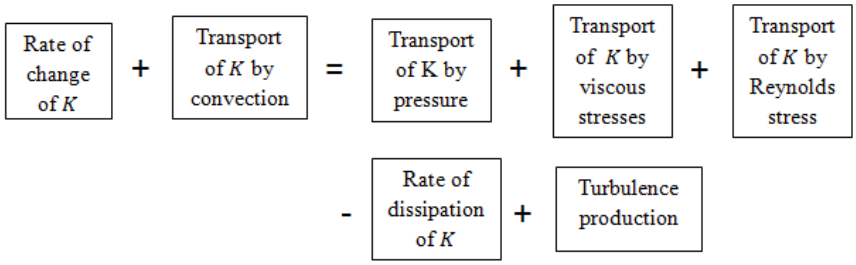

Similarly, the governing equation for the turbulent kinetic energy k is:

$$\frac{\partial(\rho k)}{\partial t} + div(\rho k\mathbf{U}) = div\left(-\overline{p'\mathbf{u}'} + 2\mu\overline{\mathbf{u}'e'_{ij}} - \rho\frac{1}{2}\overline{u'_i \cdot u'_i u'_j}\right) - 2\mu\overline{e'_{ij} \cdot e'_{ij}} - \rho\overline{u'_i u'_j} \cdot E_{ij} \quad (6.40)$$

(II) (II) (III) (IV) (V) (VI) (VII)

In words, for the turbulent kinetic energy k, we have

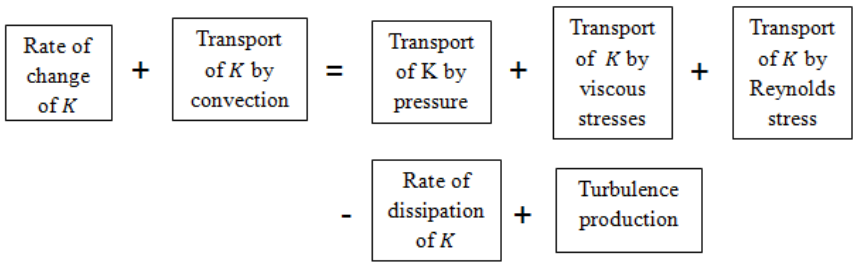

The viscous dissipation term (VI) in Eq. 6.40 gives a negative contribution

$$2\mu\overline{e'_{ij} \cdot e'_{ij}} = -2\mu\left(\overline{e'^2_{11}} + \overline{e'^2_{22}} + \overline{e'^2_{33}} + 2\overline{e'^2_{12}} + 2\overline{e'^2_{13}} + 2\overline{e'^2_{23}}\right) \quad (6.41)$$

The rate of dissipation per unit per mass $[\mathrm{m}^2/\mathrm{s}^3]$ is really important in the study of turbulence dynamics and is defined as

$$\varepsilon = 2\nu\overline{e'_{ij} \cdot e'_{ij}} \quad (6.42)$$

See Versteeg and Malalasekera (1995) for further details.

The exact $k-\varepsilon$ equations would contain many unknown and unmeasurable terms. The standard $k-\varepsilon$ model (Launder and Spalding, 1974) has two model equations, one for k and one for ε, based on the best understanding of the relevant processes causing changes to these variables.

k and ε are used to define velocity scale ϑ and length scale l representative of the large scale turbulence as follows:

$$\vartheta = k^{1/2} \qquad (6.43)$$

$$l = \frac{k^{3/2}}{\varepsilon} \qquad (6.44)$$

Applying the same approach as in the mixing length model, the eddy viscosity is specified as follows:

$$\mu_t = C\rho\vartheta l = \rho C_\mu \frac{k^2}{\varepsilon} \quad (6.45)$$

where C_μ is a dimensionless constant.

The standard model uses the following transport equations used for k and ε:

$$\frac{\partial(\rho k)}{\partial t} + div(\rho k\mathbf{U}) = div\left[\frac{\mu_t}{\sigma_k} grad\ k\right] + 2\mu_t E_{ij}\cdot E_{ij} - \rho\varepsilon \quad (6.46)$$

$$\frac{\partial(\rho \varepsilon)}{\partial t} + div(\rho \varepsilon\mathbf{U}) = div\left[\frac{\mu_t}{\sigma_\varepsilon} grad\ \varepsilon\right] + C_{1\varepsilon}\frac{\varepsilon}{k}2\mu_t E_{ij}\cdot E_{ij} - C_{2\varepsilon}\rho\frac{\varepsilon^2}{k} \qquad (6.47)$$

In words the equations are

Rate of change of k or ε	+	Transport of k or ε by convection	=	Transport of k or ε by diffusion	+	Rate of production of k or ε	-	Rate of destruction of k or ε

The equations contain five adjustable constants C_μ, σ_k, σ_ε, $C_{1\varepsilon}$, $C_{2\varepsilon}$. The standard $k-\varepsilon$ model employs values for the constants that are arrived at by comprehensive data fitting for a wide range of turbulent flows:

$$C_\mu = 0.09;\ \sigma_k = 1.00;\ \sigma_\varepsilon = 1.30;\ C_{1\varepsilon} = 1.44;\ C_{2\varepsilon} = 1.92 \qquad (6.48)$$

The Reynold stresses with this model can be computed with an extended Boussinesq relationship:

$$-\rho\overline{u'_i u'_j} = \mu_t\left(\frac{\partial U_i}{\partial x_j}+\frac{\partial U_j}{\partial x_i}\right)-\frac{2}{3}\rho k\delta_{ij} = 2\mu_t E_{ij}-\frac{2}{3}\rho k\delta_{ij} \quad (6.49)$$

Where δ_{ij} is the Kronecker delta (δ_{ij}=1 if $i=j$ and δ_{ij}=0 if $\neq$i).

The boundary conditions have to be added and can be found in Chap. 3 of Versteeg and Malalasekera (1995)

6.3.2 RANS and $k-\varepsilon$

RANS equations are used very frequently by the most common programs, like Fluent. The diffusion of those equations, for practical purposes and for research, spread out in the last decades thanks to its good results. This turbulence model has been validated by many studies, and has achieved notable success in calculating a wide variety of thin shear layer and recirculating flows. The model performs really well in confined flows where the Reynolds shear stresses are most important.

However, in many cases, the $k-\varepsilon$ model is known to be inefficient. This is the case of unconfined flows.

Moreover, this model gives really good results in the case of flow around streamed line objects, but flow around sharp edged bluff-body involves many difficulties as pointed out by Murakami (1998) and Stathopoulos (1997).

In this work the focus is on bluff-bodies, therefore this model is expected to give results that are not enough adherent to reality. In literature there are plenty of examples describing the behavior of wind around a cubic obstacle. The main issue is, of course, the behavior of the stream close to the sharp corners. In CFD, those points are kind of singular points, therefore there are not better results even with a really fine grid. (Murakami, 1998). Intensive studies have been done on the suitability of various turbulence models (Murakami and Mochida 1989; Murakami 1998; Castro and Graham 1999; Saha and Ferziger 1996,1997). RANS has been used in wind engineering application due to their simplicity in modeling and reduced computational cost.

As pointed out many times in literature (Murakami 1993, Murakami 1997) one of the main issues of the $k-\varepsilon$ model is the overproduction of turbulent energy k at impinging region, as show in Figure 64.

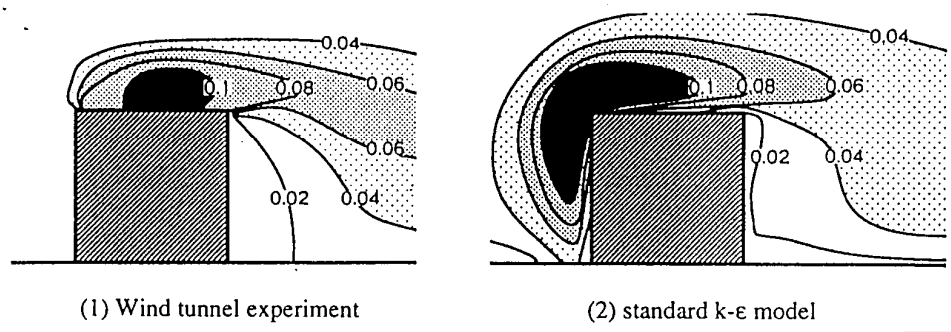

Figure 64 - Over-production of turbulent energy k by the standard $k-\varepsilon$ model

The reason of this lies, of course, in the equations and it is very well explained by Murakami (1993). As soon as researchers have been aware of this problem they started developing improvements for the $k-\varepsilon$ model with several ad-hoc modifications of the model as a remedy.

Murakami (1993) presented a short review of them : LK model, MMK model, three equation model (keFI) by Kawamoto. Those models successfully corrected the overproduction of k at the impinging region. Among them, MMK gives the best results in terms of pressure, too.

On the other hand, these modifications lead to worse predictions of the velocities, especially in the wake of obstacles.

All linear eddy viscosity models suffer from the assumption of isotropy of the normal Reynolds stresses. Therefore non-linear models, which are able to deal with anisotropy, should perform better in wind engineering.

As an intermediate summary it can be stated that the standard $k-\varepsilon$ model should not be used in the simulation of wind engineering problems in general. The main factors causing problems applying CFD to wind engineering can be summarized as:

1- Large Reynolds number
2- Impinging at the front wall
3- Sharp edges of the bluff body
4- Remaining effect of flow obstacle at outflow boundary

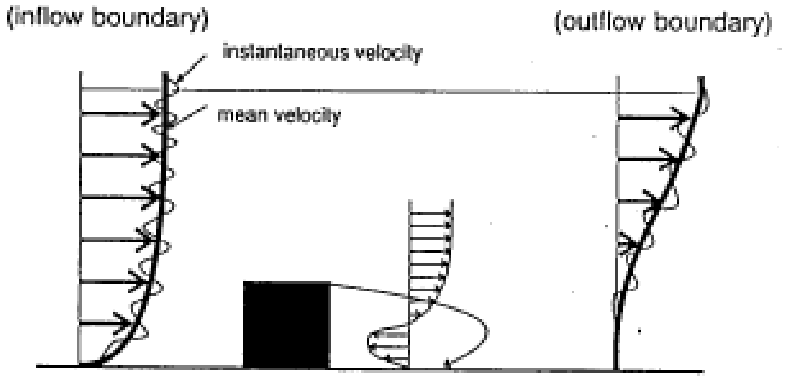

Figure 65 - Effect of flow obstacle remaining at outflow boundary

7 Data analysis

7.1 Extreme values

As already mentioned, the test was run for 360 degrees every 10 degrees. The reason why is that, of course, a different behavior of pressures is expected with different wind directions and the highest values are expected to be shown when the wind does not impact the surface perpendicular to the windward face.

Anyway, it is really helpful to interpret the following results with a constant comparison with the literature. Many studies have been done on the flow of the wind across a cubic obstacle, and the flow pattern is expected to be like the one shown in Figure 66.

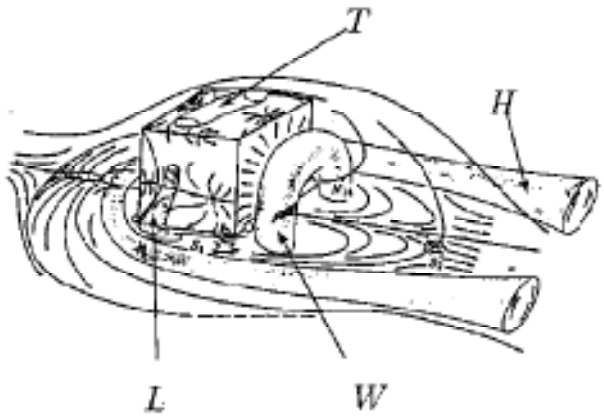

Figure 66 - Schematic representation of the flow features by Martinuzzi and Tropea

The aim of the present work is to describe the pressure behavior, but it is fundamental to compare and interpret the results comparing them with the wind flow. Unfortunately in literature most of the studies on the cubic obstacle focus only on the 0 degrees case. This is the reason why, for the present work, PIV techniques were used to help to interpret the results.

The first interest result is to look for the highest pressure and suction coefficients in every tap, changing the wind angle. To present this work it has been chosen to stick to the C_p coefficients, with reference pressure changing with the height.

Starting from the suctions, Graph 4 - Pressure coefficients of corner tap number 132 shows the maximum negative C_p values for tap 132. To understand the results it is important to remind that Tap. 132 is the first tap in the upper corner on the edge of the wall. The results are shown as raw data, with the Tube Transfer Correction, and also with the Fisher Tippet analysis. The final results to be considered are the green line.

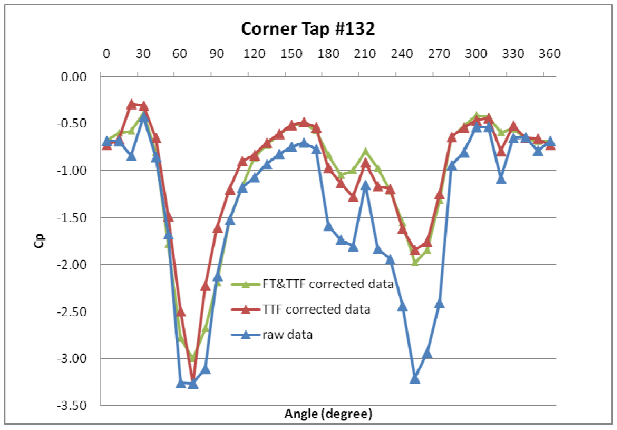

Graph 4 - Pressure coefficients of corner tap number 132

This graph shows in first place the mitigation of the peaks generated by the corrections. In particular the reduction is accentuated for the angles around 250 degrees. The other peak is shown around 60/70 degrees. This is somehow what was expected, because the higher suctions occurs when the wind comes from an inclined direction and does not impact perpendicular to the windward side. Because of it the flow is highly asymmetric and characterized by big flow separations.

For this tap the highest suction value is C_p=3.00 and is reached for 70 degrees.

Figure XXX shows the maximum values of the same tap .

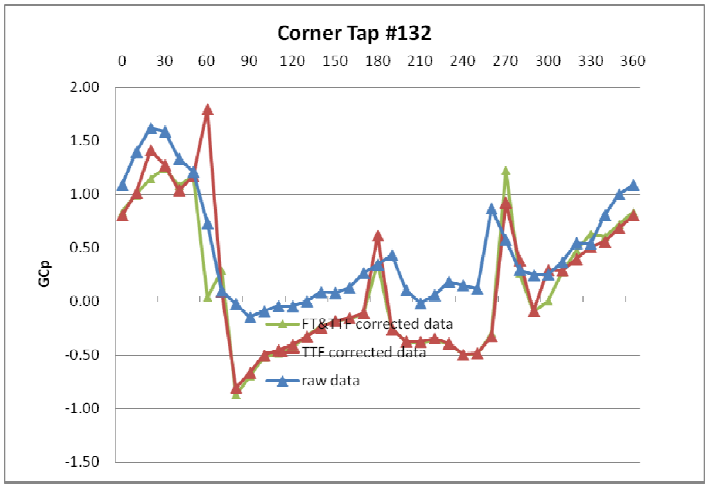

Graph 5 - Gust Pressure coefficient of the corner tap number 132

It can be noticed that the effect of the correction is analogous but that the positive values are much smaller. Of course, between 90 and 270 degrees there are no positive values because the tap. is always in the suction zone.

On the roof the most interesting values are the suctions. Graph 6 shows the C_p results on the roof, for Tap. 10.

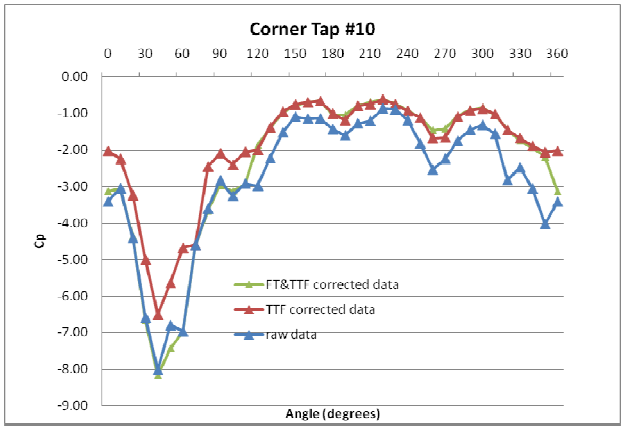

Graph 6 - Pressure coefficient of the corner tap number 10

It is very clear that there is a very high peak for 40 degrees where the C_p reaches a value of - 8.17. It is important to notice that suctions on the roof are much higher than those on the sides. Again, the higher values occur when the wind is not perpendicular to the windward face but when the asymmetry causes really big suctions and vortices.

Of course, the highest values and the correspondent angle will change tap by tap, and a clearer more synthetic view will be presented later with the aid of level curves.

7.2 Pressure level curves

After all the corrections and the calculation of all the pressure coefficients for every single tap, it is possible to combine them to have a complete view of the pressure patterns on the cubic building.

For this representation the C_p values will be plotted, and all of them are calculated related to their reference height. At first, it is interesting to focus on the minimum values for the reference pressures, because those values are expected to show in the best way the behavior and the effects of the turbulences around the building.

0 degrees

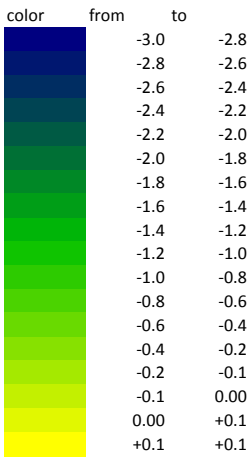

Figure 67 - Pressure levels curves of 0 degrees wind flow

From the contours of Figure 67 all the main characteristics of the wind flow are shown. At the windward face the pressure is almost constant and is very low. This happens because those contours show the minimum values while this face is mainly interested by positive pressures. At the windward side there is, in the center of the face, the stagnation

point, while moving to the side sides and to towards the roof some suctions appear because of the vortexes.

Figure 68, obtained with the PIV test for flow visualization, shows the stagnation point at the front and the vortexes in the lower part of the building.

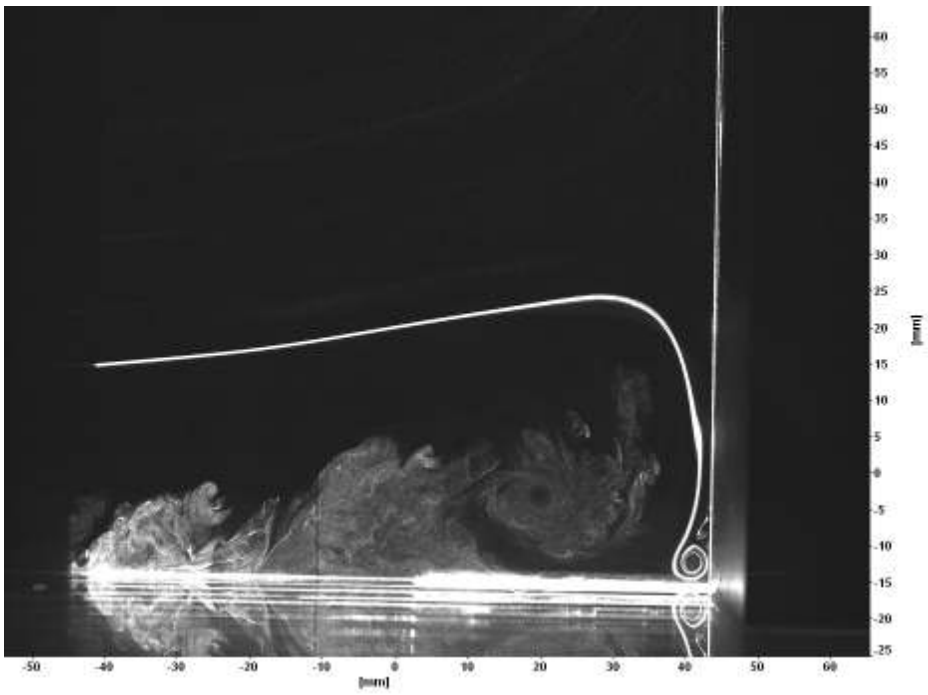

Figure 68 - Smoke visualization in the front side

Focusing on the sides, the big flow separations are shown. As expected, the biggest suctions are right after the edge of the sides with the windward face, and the bigger values are at the corners (C_p close to - 2). As the wind tries to reattach to the sides the suction gradually decreases till values of C_p smaller than - 1.

The leeward side is interested by very big suctions and all the values are negative. Thanks to the symmetry the patterns is quite constant with a range of values from 0 to -0.75.

The most interesting part is the roof. The front corners of it present the biggest suctions of the whole structure, reaching values up to C_p=-3. The behavior in the back part is analogous to what happens on the sides: the suctions decrease gradually as the flow tries to reattach.

It is really interesting and helpful at the same time interpret those results in light of the PIV analysis and the literature, too.

Figure 66 by Martinuzzi and Tropea resume really well the complex wind flow around the building. This study has the porpoise to focus on the pressures, but those results match really well with the flow given by Figure 66, in fact Figure 67has suctions where Martinuzzi and Tropea indicated flow separation.

With the aid of the PIV analysis run in the Wind Tunnel of the university of Miami, it is also possible to interpret the pressure contours with the pattern obtained from the wind particle velocity analysis.

Figure 69 shows the wind speed in magnitude and direction, at an height of ¾ of the total height of the building. The wind speed slowdown in front of the building, and his acceleration at the edges where the separation occurs. It can be noticed that where a really low speed is measured with the PIV a really high negative pressure coefficients are measured with the wind tunnel test.

In particular at the leeward side the speed vectors show how the air is sucked in by the suction and recirculates back to the sides.

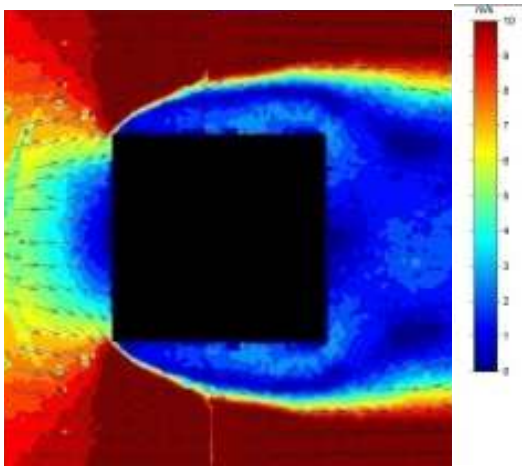

Figure 69 - PIV visualization for wind coming perpendicular to the front surface

Of course, it has to be noticed that the pressure map is based on the minimum values, while the PIV analysis presents the mean values. It could be possible to show the minimum values for the PIV, too, but it would be less significant to interpret the general behavior of the wind.

7.3 Comparison with ASCE

One of the porpoises of the present work is to compare the results obtained from the wind tunnel test with the codes. First of all a comparison with the ASCE code is fundamental, for many reasons.

The first reason is that the ASCE does not explicit the source of the results that presents, and this test is a very good chance to validate them. Moreover, it has to be noticed that the model of the present test is characterized by a really high number of taps and the pressure contours are really detailed. It has never been done a test on a similar structure with so many pressure taps.

The ASCE, on the contrary to what it has been chosen to take as a reference in this work, refers to the GC_p coefficients, which means to take in account of the gust speed as already detailed explained in Chapter 4.

The ASCE, for a building with a flat roof, focuses on the edges and on the corner of the roof for a strip with *a* as width (Figure 70).

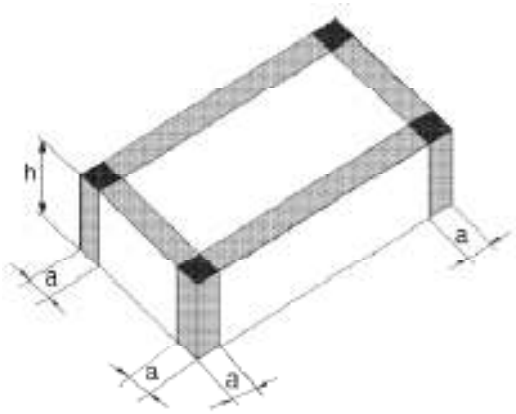

Figure 70 - ASCE scheme for wind pressure

a is defined as the 10 percent of least horizontal dimension, but not less than 3 ft (0.9 m).

In the present work

$$a = \frac{L}{10} = \frac{0.508}{10}[m] = 5[cm]$$

In real scale it means a width of 3 meters.

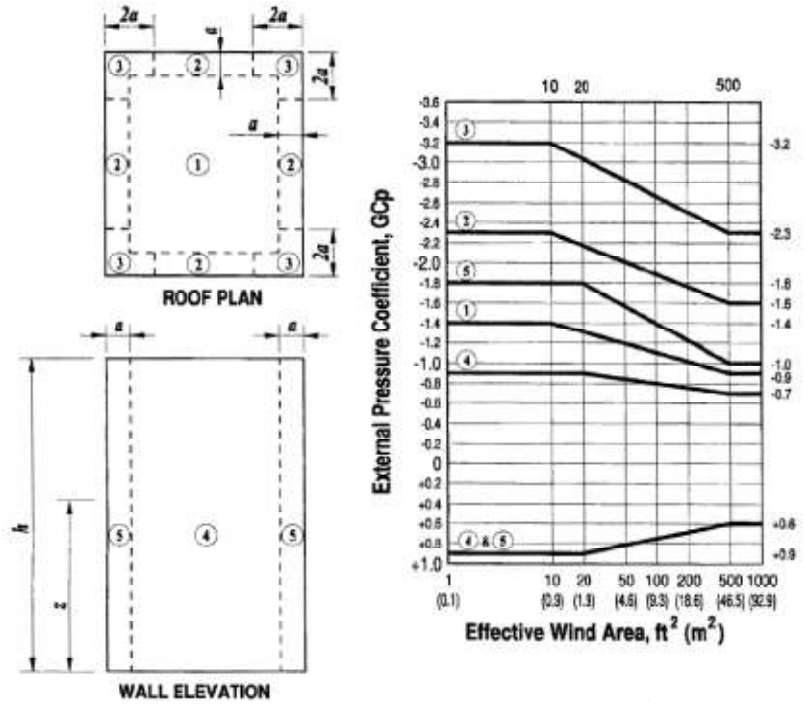

Figure 71 - ASCE scheme for building higher than 60 feet

The ASCE, as shown in Figure 71, starting from the just mentioned strips, considers different zones. The zone with the highest pressures are the corners, for a length of *2a*. To make a reasonable comparison between the test cube and the code it is necessary to see the same areas' division on our model, like in the Figure 72. And there it is possible to notice the same 5 areas.

Commento [F2]: The solo se metto code…
Mettere solo ASCE senza articolo

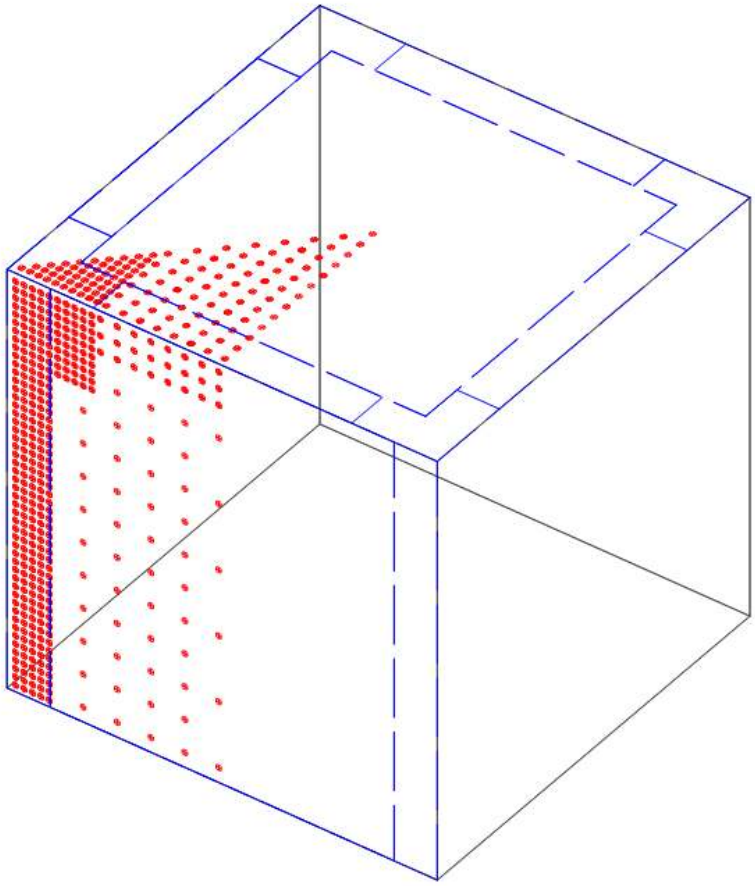

Figure 72 - ASCE effective areas on the cubic model

To be able to compare the results from the Wind Tunnel test with the code it is necessary to plot the maximum negative values. Considering the envelope of the pressures with the different angles it is possible to plot the results only for one octave of the structure. For a better visualization the roof pressures are mirrored on the diagonal to show one quarter of the total area of the roof. Taking into account the symmetry of the cubic structure it is enough to compare it with the code.

From the Wind Tunnel tests the following GC_p pattern was found:

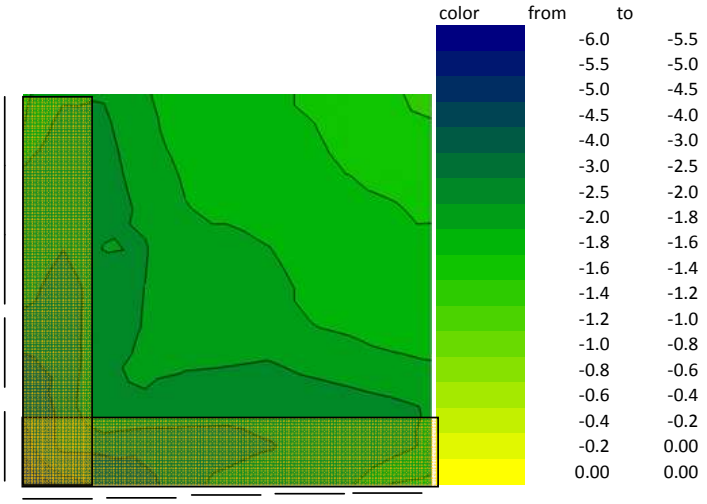

Figure 73 – ASCE effective areas on the roof surface of the cubic model

On Figure 73 the highlighted part corresponds to the strip of width *a* from the code.

The first comment is that the really high density of the pressure taps allows to have contours much more precise than in the code. But even more than that: the taps density allows to measure values at the corners that are much higher than the ones in the code, that are probably the outcome of the average on the corner zone.

To show the effective area it is clear from the next figure what the meaning of effective area for the code is. At first we use effective area for a smaller zone attached to the corner of the edges, making an exact average among the values, each of them calculated in relation on its own effective area.

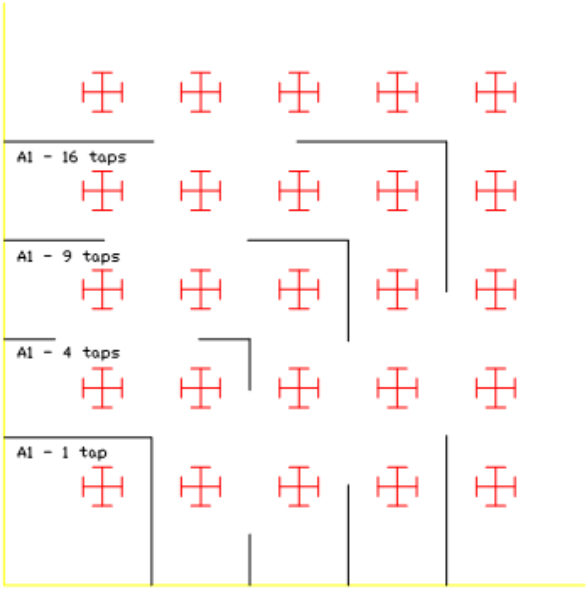

Figure 74 - Effective area increasing calculation

Of course we use another time the symmetry to find the values all over the flat surface of the roof.

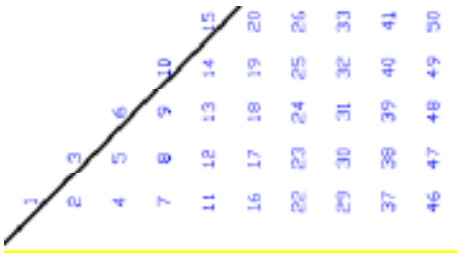

Figure 75 – Using symmetry to calculate the average pressure in the effective area

Using this code and this areas' division we should make a graph with the different areas we consider to check whether the GC_p values are always lower of what the code says. In

fact we have a great number of taps and it is very interesting to check if in the corner zone we have the value as the code says.

From a simple calculation the average results to be equal to $GC_{pcorner}$= -2.49.

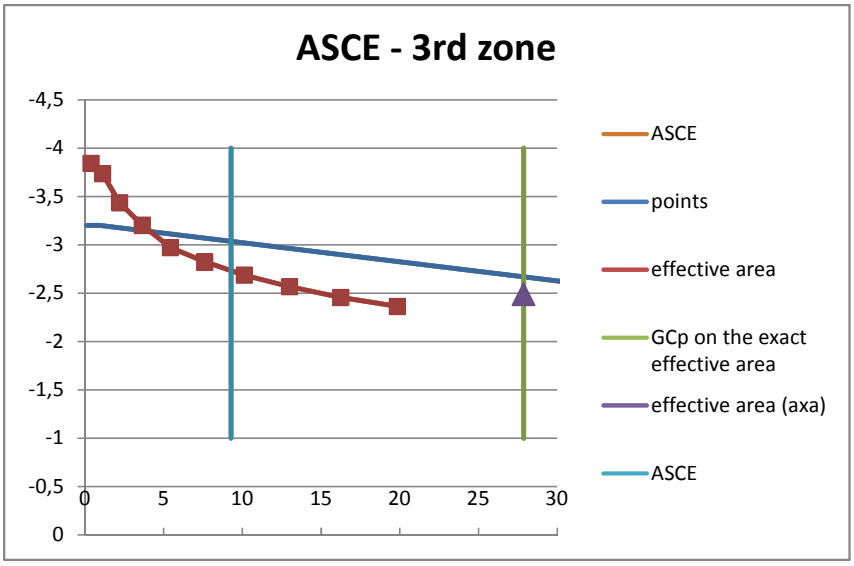

Graph 7 - ASCE 3rd zone (roof corner zone)

In this graph (Graph 7) it is clear that the corner zone closest to the edges are over the GC_p values of the code. The ASCE curve is the code extreme values, the points curve is the values from the test averaging on squared areas increasing from the corner; then we have the limit for the real corner zone a x a and the limit for the corner zone according to the code and scaled to our real test. The triangular value is the peak negative value of the suctions in the zone 3.

The meaning is that the code doesn't deal with the peak negative pressures in the corner zone. Practically the cladding loads in that zone are higher then what the code says and if the designer has to project a cladding items for the very external zone close to the corner, he has to know that the suctions are higher.

Considering that the area of the corner in the present work can be calculated as

$$2a^2 + a^2 = 0.0077\ m^2(model\ scale) = 27.87091\ (real\ scale)$$

The following figures (Figure 76 - side min z and Figure 77 – side min h), considering the roof at first, it is clear how the results are well comparable with the ASCE code. In fact, the maximum negative pressure coefficients are at the corners and along the edges, gradually decreasing moving to the center of wall.

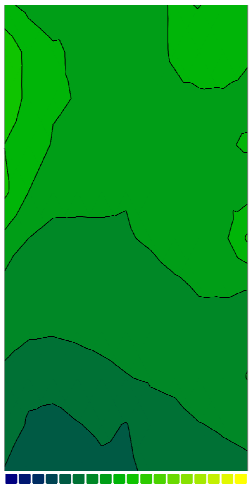

Figure 76 - side min z

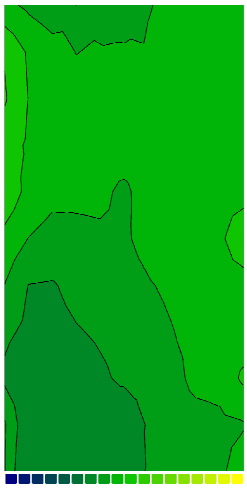

Figure 77 – side min h

Along the height of the side walls the same reasoning could be followed, but this time the code and the test show the same values.

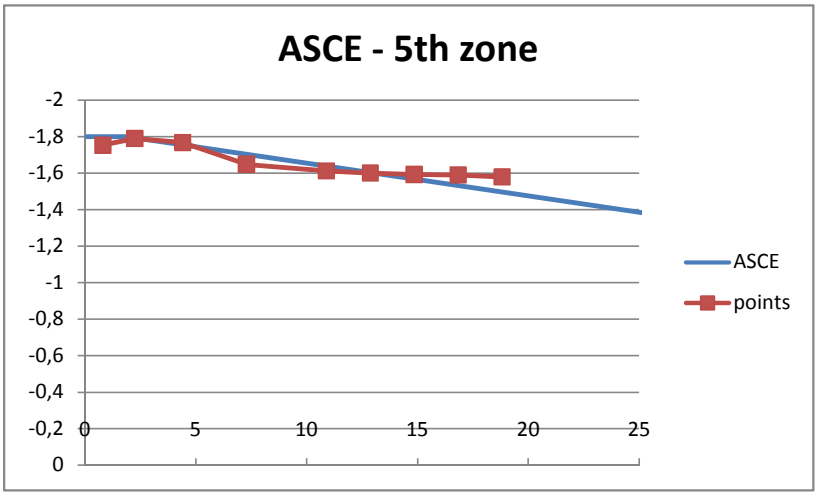

Graph 8 - ASCE 5th zone (wall edges)

It is interesting to underline that according to our data the decreasing of the GC_p values are less fast than the code says.

7.4 C_l, C_d and C_m

For each strip of the data around the model all the mean aerodynamic coefficients were calculated, at first referred to the body axes and then to the wind directions. There is a focus on the variation with the height of these coefficients. 12 horizontal strips were chosen to describe this variation. It is necessary to define exactly the strips to integrate the pressures and calculate the coefficients.

$$C_{\bar{F}_{x,j}} = \frac{\bar{F}_{x,j}}{q_j B H_j}$$

$$C_{\bar{F}_{y,j}} = \frac{\bar{F}_{y,j}}{q_j B H_j}$$

$$C_{\bar{M}_{z,j}} = \frac{\bar{M}_{z,j}}{q_j B^2 H_j}$$

$$C_{\bar{F}_{x,j}} = \frac{\bar{F}_{k,j}}{q_j B H_j}$$

$$C_{\bar{D}_j} = \frac{\bar{D}_j}{q_j B H_j}$$

$$C_{\bar{L}_j} = \frac{\bar{L}_j}{q_j B H_j}$$

Where $\bar{F}_{k,j}$ is the mean force in the j strip in k direction, q_j is the pressure due to mean wind at the height of the j strip ($q_j = \frac{1}{2}\rho V_m^2$), B is the dimension of the box and H is the height of the strip.

The first issue is to calculate all the reference area for each measurement. In order to obtain this result it is necessary to use Autocad and look at the values of the areas we used to divided the total side surface as it is shown in the following (Figure 78 and Figure 79).

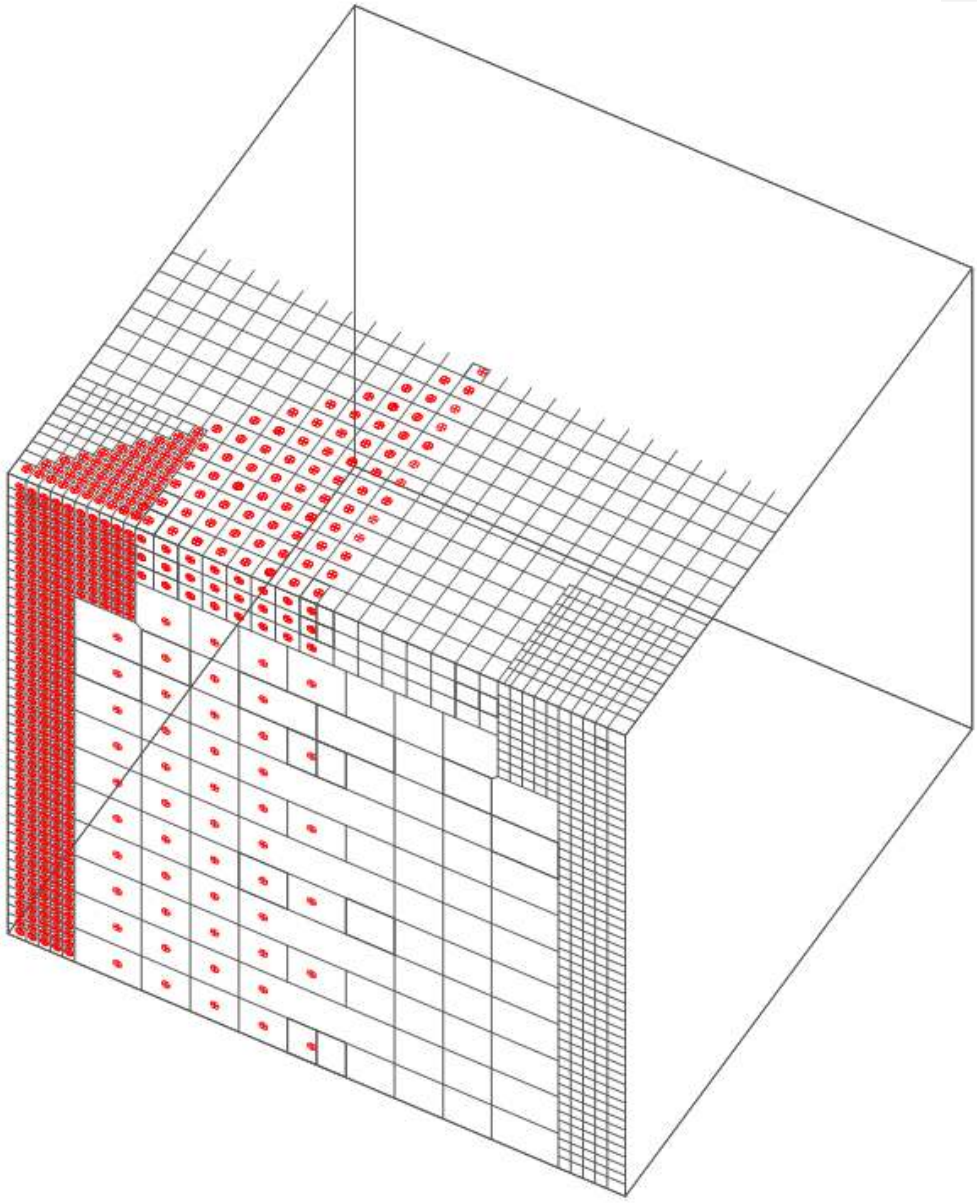

Figure 78 - Areas' division on the external surface of the cubic model

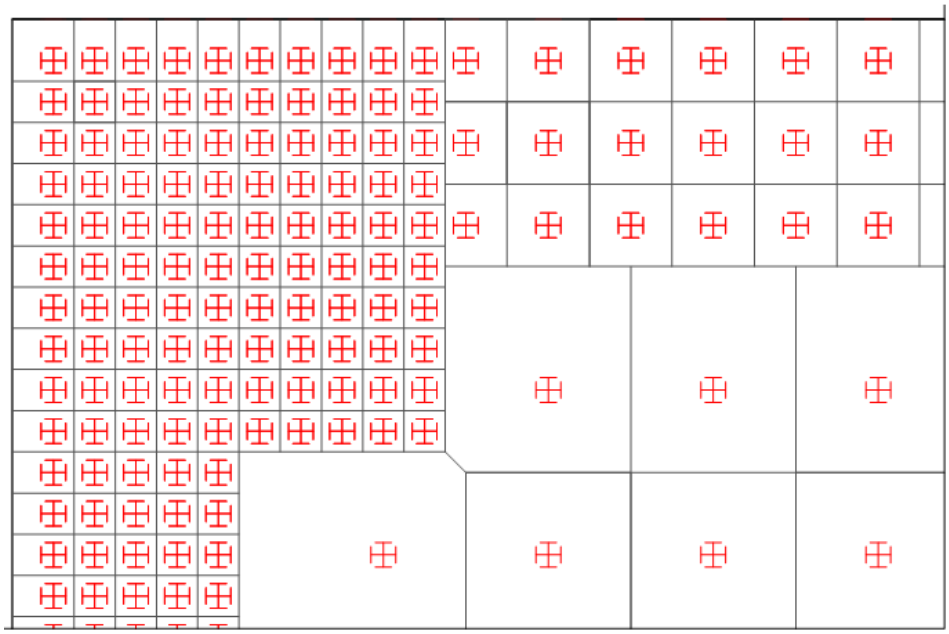

Figure 79 – Focus on the wall corner of the areas' division on the external surface of the cubic model

There are the graph of the development of the values of C_d with the different angle's exposition referred to the C_d of all the building and also referred to the middle strip. It is possible to translate the obtained graph to complete all the degree scale, but it should be the same because of the symmetry used to build and to measure the pressures. The worst situation is obviously when the diagonal of the square section is aligned with the wind direction (45° degrees). The value of the C_d corresponds on what it is written on the codes. Making a comparison with other works and paper, the values are reasonable and confirmed by other research works. In the comparison with the graphs on www.esdu.com the value are a bit more.

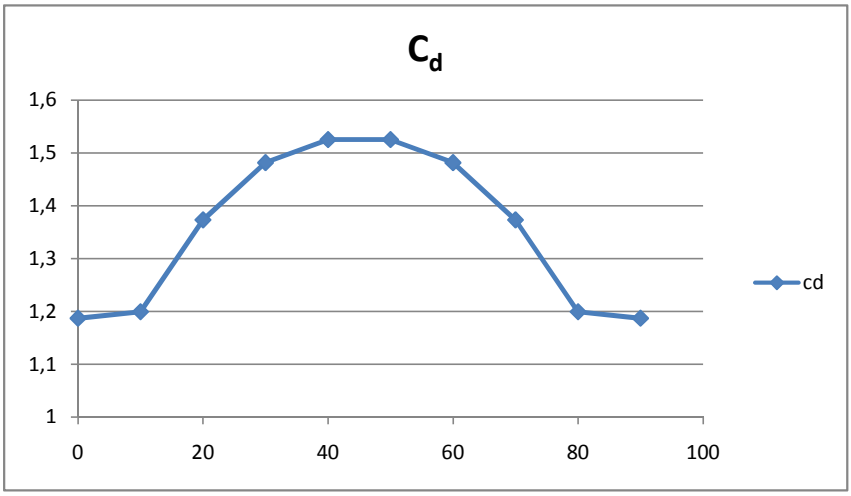

Graph 9 - C_d coefficient

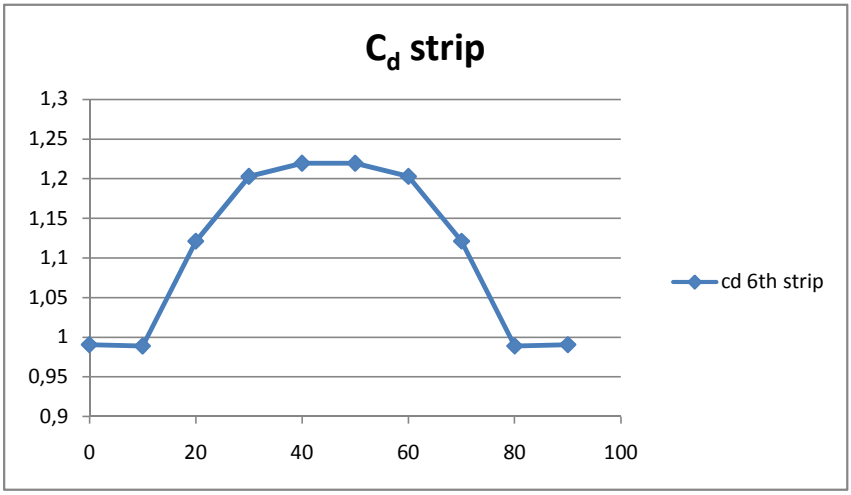

Graph 10 - C_d coefficient of the 6th strip

In the C_d coefficients of the cube (Graph 9 and Graph 10), obviously the maximum of the drag is when the wind is in the direction of the diagonal, as we said above; in fact in that direction we have two sides completely with positive pressure due to the wind

force. The maximum of the drag is around 2/3 of the height and we analyzed here the middle strip, so the drag coefficient is not as strong as the value referred to all the box.

In the next graph (Graph 11 - C_d) we have the C_d coefficient variable with the height and it is clear that the maximum force of drag is acting neither in the middle part neither in the top part. in the top part the wind flow away and surmount the box, so the maximum is a little lower than the top. In the bottom we have strong force, because of strange effects; in this part we have the pedestrians effect and it is very turbulent.

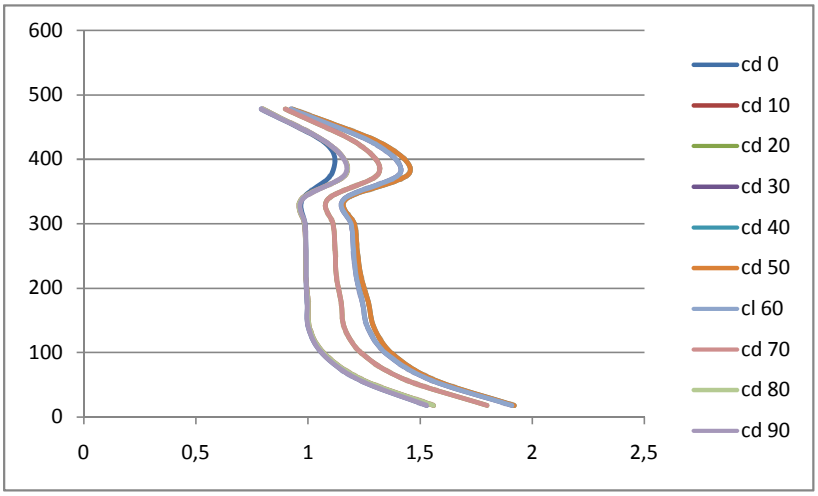

Graph 11 - C_d coefficient changing with the height

The C_l coefficient has a different period from C_d coefficient and its values are both negative and positive. It depends a lot from the wind directions (Graph 12, Graph 13 and Graph 14).

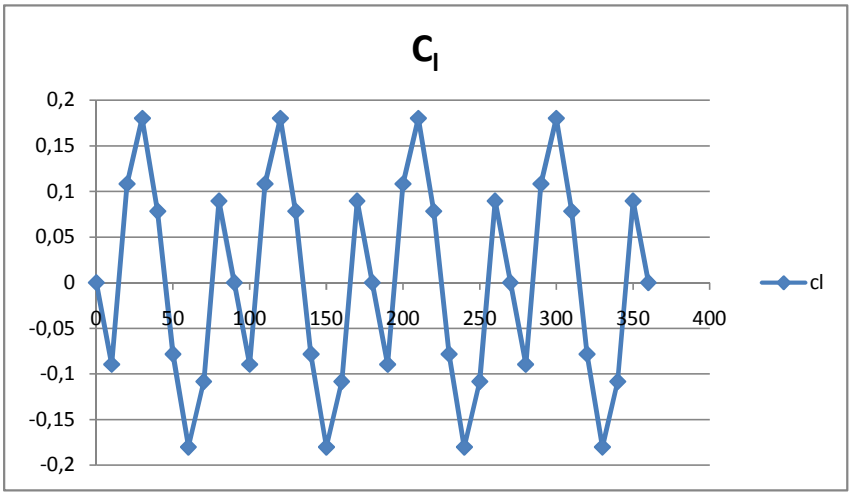

Graph 12 - C_l coefficient

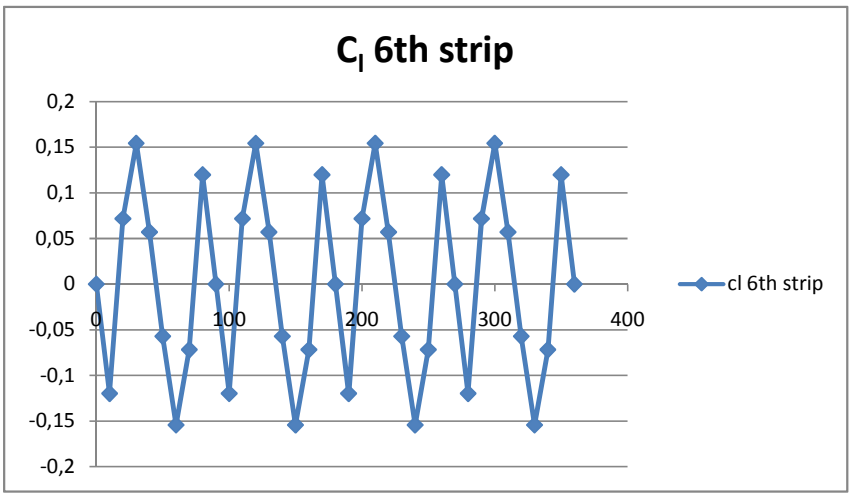

Graph 13 – C_l coefficient of the 6th strip

The values are zero when the wind is coming perpendicular to the front surface and more is the distant from two of this positions more is the values positive or negative.

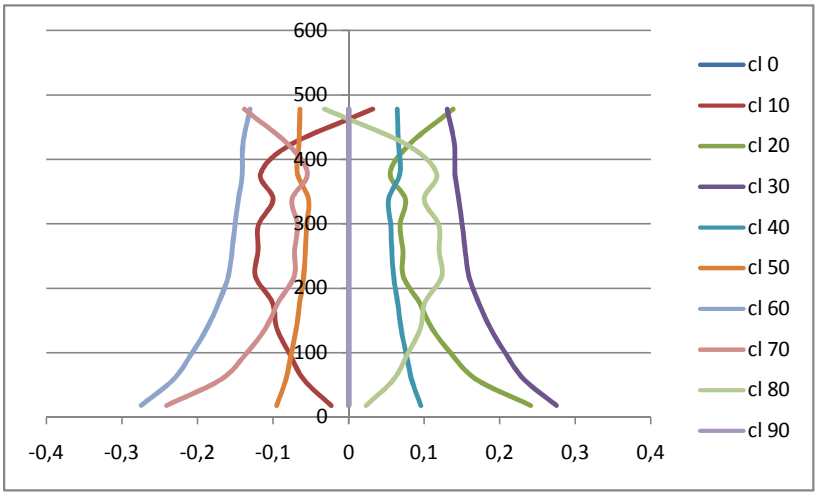

Graph 14 - C_l coefficient changing with the height

The following are the graphs of the momentum coefficients and they are congruent with the values in the literature. In fact we have positive and negative values and the range of the values is reasonable (Graph 15, Graph 16 and Graph 17).

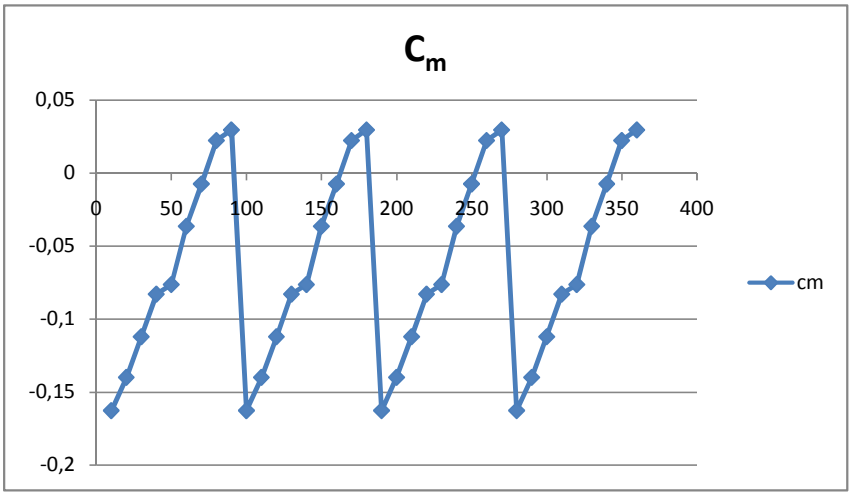

Graph 15 - C_m coefficient

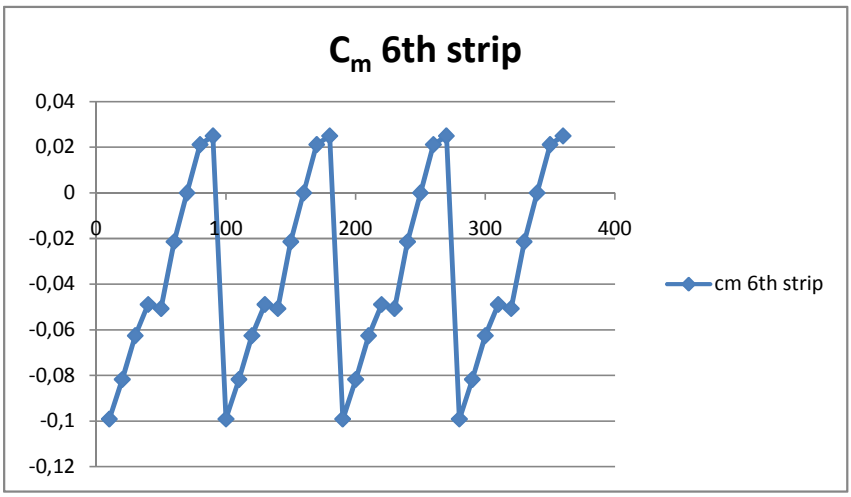

Graph 16 - C_m coefficient of the 6th strip

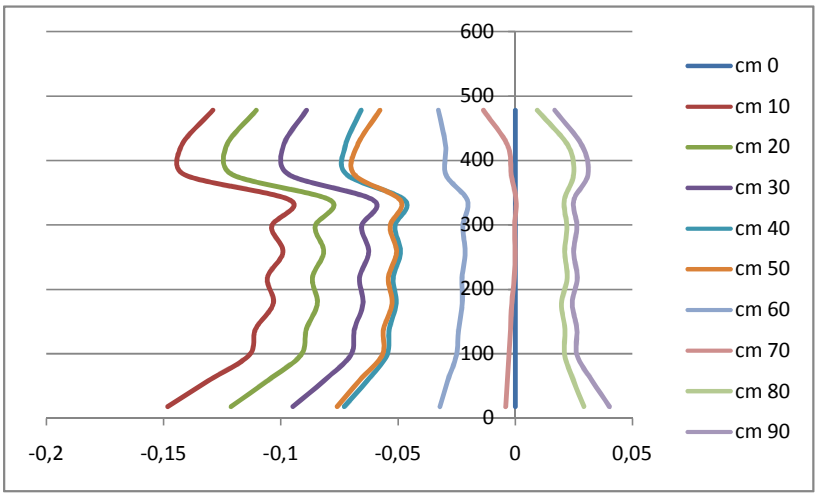

Graph 17 - C_m coefficient changing with the height

8 Conclusions

In conclusion, it is interesting to summarize the new acknowledgement reached thanks to this work, summarizing the results comparing them with the initial aims of the thesis.

The possibility to work in parallel with three different techniques (PIV analysis, CFD and Wind Tunnel Tests,) has been a strength point for the present work, showing the problem under different point of views. In fact, as shown in the first Chapters, wind behavior is difficult to predict and the constant comparison between the three different tests has helped the work to grow on a solid ground.

Of course, every different test showed and pointed out different elements of the final description given with this thesis.

PIV techniques are really effective, because directly related to the phenomena in all its complexity. The resolution of the detail shown from those tests is really high thanks to the modern cameras, and can lead to more complex analysis. In this case the main focus was on the particle flow and the velocity pattern around the structure. The choice to focus only on the qualitative behavior is that it is not possible to take for granted that the results from the Wind Tunnel Test in Miramar can be quantitatively the same as this PIV test. In fact, as already mentioned, not only the scale was different but also for the PIV test it was not possible to develop the same wind profile. Of course, the wind speed in the two tests were comparable. On the other hand, the data from this PIV test were perfect to notice flow separation and to be aware of all the vortex formation.

CFD is very difficult, also because of the mesh. And we didn't analyze all the possibilities the cfd programs have. In fact other model like first of all LES simulation could be interesting to be used, maybe in the next researches. The comparison between the measurements in the wind tunnel and the cfd results are interesting. (…)

The Wind Tunnel Test in Miramar was the most interesting part of this thesis. Of course, it lead the most complicated analysis. In fact, the level of detail of the analysis

required a really high number of taps and really heavy calculations. Anyway this yielded to really interesting conclusions in relation with the codes, even going beyond them.

In fact, this research shows the need of some codes to be updated, considering more detailed analysis and data such this one. The comparison with the ASCE has shown that in reality there are pressure peaks higher than the ones indicated in the codes, in particular in the corner zones where the separation (as the PIV and CFD results show) is very big.

Even if a designer is aware that most of the times it is enough to focus on the mean behavior of the wind, many times it is necessary to consider this extreme behavior to avoid problems such as those that happened during the construction of the "Palazzo Lombardia" in Milan.

It is impossible to answer to the beginning question about the substitution of the wind tunnel test by the cfd simulation program, because the knowledge of the cfd is bigger than we have at the end of this thesis and the case we studied is very easy. Anyways the comparison seems to be enough coherent. to answer to this questions more models and more knowledge need to be used. The experience with the wind tunnel and the PIV where the software we used were useful only for the analysis and they didn't used flow model, but they started form the observation of the data and the images obtained in the wind tunnel.

At the end it has to be pointed out that this research has shown how it is always fundamental to observe the real phenomena because of the complexity of the wind behavior. Of course, CFD sometimes can help to have a general idea before running heavy and costly tests such as the one done in Miramar.

9 Appendix A

Nonetheless in the real world there are also random excitements, which are non-deterministic, i.e. their value in a time t cannot be defined a priori but in probabilistic ways.

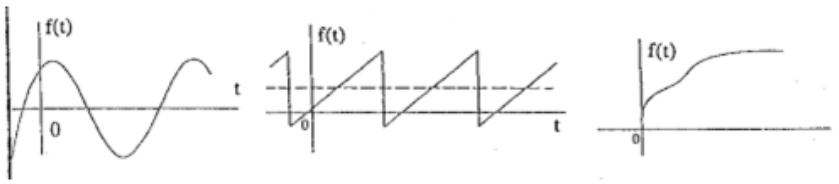

Figure 80 - Examples of deterministic forces

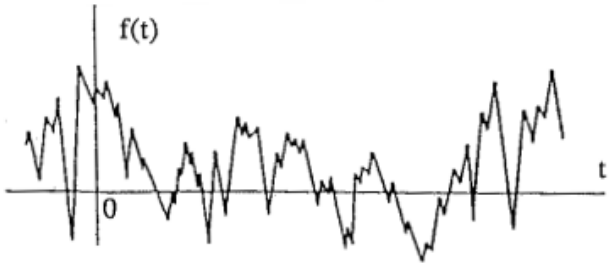

Figure 81 - An example of random force

Those excitements induce on the system a non-deterministic behavior of the structure. Wind (with its turbulence) , together with seismic phenomena, are the main causes of this type of forces.

Both of them, together with other situation bond to mechanical application, return on the system to movements, accelerations and therefore a solicitation status that has to be analyzed with precise techniques in order to define the system performance.

The study of random vibrations using stochastic process theory is a new engineering discipline in a remarkable growth in the last decade.

The problems arisen due to unpredictable excitations cannot be analyzed with the deterministic theory. It requires a probabilistic approach in which both the excitations and the mechanical results on the system are defined through statistical parameters.

Many random phenomena reveal a certain uniformity: it means that, even if in different time stories, average quantities remain constant.

In this case the excitement and the reaction can be considered as random process (or stochastic process) that can be described by few statistical parameters and by appropriate statistical functions such as the spectral power's density function.

However our attention is focused neither on the response nor on the effect, but on the force's characterization and on the solicitations' distribution (pressures and depression). We are not now going to deal with phenomena of vibrations, that are mostly related to slim structures.

We shall now consider a generic experiment of measurement of an unpredictable variable (the analyzed signal may represent a an applied force, or a given displacement, or a vibration calculated in a point of a mechanical system, ext...).

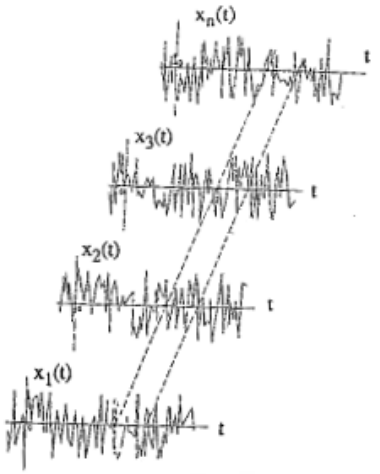

Figure 82 - Random process defined by different random variables

Let x1(t) be the registered temporal story (picture); it is possible to determine a second temporal story by measuring the same magnitude in similar conditions of proof: such temporal story will be different from the previous (the reason of such difference is usually difficult to find out since the factors that affect this phenomena are unknown).

Iterating the measurements (i=1,2,..N) (for example we make a registration with an anemometer at the same speed of the wind) it is defined as a random variable. On the other side all the temporal stories (the whole group of registration made in equal condition, for example same location, medium value and direction of wind) represent the random process or stochastic process.

Each observation (non-periodic) has a pattern altogether similar to others, but they are differentiated by few details. Of these dimensions, also called unpredictable and statistically regular, is possible to define some constant statistic parameters.

Generally a stochastic process could depend on time or space; in this work we will consider only time dependence.

Most of the time the general variable x1(t) is not representative of the entire process, except but in unpredictable process defined ad stationary and ergodic . In this case is possible to obtain statistic information of an entire process form the analysis of just one variable

For the analysis of the random process we define some significant statistical values, which characterize the entire process. Whenever this happens, we call the stochastic variable regular.

Before analyzing in a deeper way random phenomena, we want to introduce briefly the meaningful magnitudes in order to define statistically the characteristics.

Given a time story x(t) we define:

mean value (or static component):

$$\mu_x = E[x] = \lim_{T\to\infty} \frac{1}{T}\int_0^T x(t)dt$$

Quadratic mean value (or dynamic component):

$$\Psi^2{}_x = E[x^2] = \lim_{T\to\infty} \frac{1}{T}\int_0^T x^2(t)dt$$

RMS (root mean square), root square of quadratic mean value:

$$RMS = \sqrt{\Psi^2{}_x}$$

Variance:

$$\sigma^2{}_x = \lim_{T\to\infty} \frac{1}{T}\int_0^T (x(t)-\mu_x)^2 dt = \Psi^2{}_x - \mu^2{}_x$$

Standard deviation(a magnitude that define the fluctuations of the magnitude around the mean value):

$$\sigma_x = \sqrt{\sigma^2{}_x}$$

It is defined also as the auto correlation function:

$$R_{xx}(\tau) = \lim_{T\to\infty} \frac{1}{T} \int_0^T x(t)x(t+\tau)dt$$

This magnitude has the following properties:

$$R_{xx}(0) = \lim_{T\to\infty} \frac{1}{T} \int_0^T x(t)x(t)dt = \Psi^2{}_x$$

$$R_{xx}(\tau) = R_{xx}(-\tau)$$

$$R_{xx}(0) \geq |R_{xx}(\tau)|$$

The autocorrelation function is often defined in an a dimensional way:

$$\bar{R}_{xx}(\tau) = \frac{R_{xx}(\tau)}{R_{xx}(0)} = \frac{R_{xx}(\tau)}{\Psi^2{}_x} \rightarrow -1 < \bar{R}_{xx} < 1$$

Whenever the auto-correlation function is equal to 1 we have the maximum correlation. If it is equal to 0 we have no correlation, whereas if equal to -1 we still have the maximum correlation but we have the phase-shift.

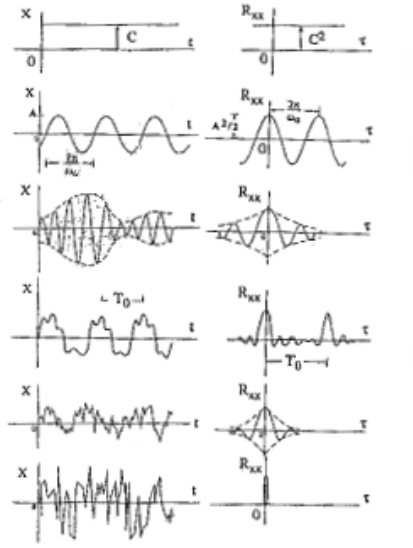

Figure 83 - Rxx(t) for some characteristic functions (constant, sine, beats, periodic, random and white rumor)

In the picture above we see the auto-correlation function for some characteristic functions.

Let us consider two different time-stories x(t) and y(t), we can define also the cross-correlation function:

$$R_{xy}(\tau) = \lim_{T\to\infty} \frac{1}{T} \int_0^T x(t)y(t+\tau)dt = -R_{xy}(\tau)$$

Whereas the auto-correlation function is an even function, this is odd:

$$R_{xy}(\tau) \neq R_{xy}(-\tau)$$

at the same time:

$$R_{xy}(\tau) = R_{yx}(-\tau)$$

if the cross-correlation, with any tau, is zero, the processes are statistically incoherent. Examples of this function follow:

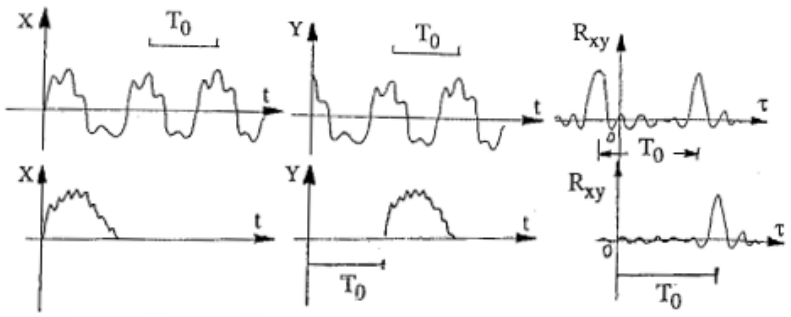

Figure 84 - Rxy(t) for some characteristic x(t) and y(t)

These values give information about the random process in time. From the picture, we particularly point out the delay of tau at which we have a high cross-correlation value, which correspond to the lateness of arrival to the two different measure point. This approach is used for identifying the spring in acoustic emission problems.

The auto-correlation defines the signal's characteristics in the time's domain, whereas the power spectral density function defines it in the frequency's domain.

The power spectral density function (also called one side auto-spectral function) is the autocorrelation's Fourier transform.

$$G_{xx}(f) = 2\int_{-\infty}^{+\infty} R_{xx}(\tau)e^{-i2\pi f\tau}d\tau$$

$$G_{xx}(\omega) = 2\int_{-\infty}^{+\infty} R_{xx}(\tau)e^{-i\omega\tau}d\tau \ con\ (\omega = 2\pi f)$$

This values has the following proprieties:

$$\int_0^{+\infty} G_{xx}(f)df = \int_0^{+\infty} G_{xx}(\omega)d\omega = \Psi^2{}_x = \sigma^2{}_x + \mu^2{}_x$$

i.e. the area underneath the power spectral function is the quadratic mean value. It immediately follows that:

$$G_{xx}(f)\Delta f = \Psi^2{}_x(f)$$

$$G_{xx}(\omega)\Delta\omega = \Psi^2{}_x(\omega)$$

If we have small frequency intervals, it represents the quadratic mean value associated to the frequency f.

The density spectral power function is a real, positive value.

Its inverse function is:

$$R_{xx}(\tau) = \int_0^{+\infty} G_{xx}(\omega)\cos(\omega\tau)\,d\omega = \int_0^{+\infty} G_{xx}(\omega)e^{i\omega\tau}d\omega = Re$$

In the picture there are some significant examples of "power spectral density function" for different signals, periodic or random. Those random processes characterized by a narrow peak (centered around the peak's frequency) are defined as narrow band. On the other hand those processes where a variable is characterized by significant value of power sensitivity in a wide range of frequency are called broad band process.

In extreme cases when only one harmonic is present (with random phase), the spectral power density is a Dirac delta function, while a spectral power density constant value defines the white noise.

If we analyze two different random process x(t) e y(t) it is possible to define:

- The cross-spectrum (also called "cross-spectral density function", this is a complex variable because the cross-correlation in not an even variable) defined as the Fourier transform of cross-correlation.

$$G_{xy}(f) = G_{yx}(f) = 2\int_{-\infty}^{+\infty} R_{xy}(\tau)e^{-i2\pi f\tau}d\tau$$

- The function of coherence (a real value),that is the non-dimensional cross-spectrum, defined by this relation:

$$\gamma^2{}_{xy}(f) = \frac{\left|G_{yx}(f)\right|^2}{G_{xx}(f)G_{yy}(f)} \; con \; 0 \leq \gamma^2{}_{xy}(f) \leq 1$$

The entire theoretical discussion is necessary to fully understand what happens studying wind's behavior. International regulations treat wind starting from this kind of statistical considerations.

Often this complex mechanism does not considerably change the characteristics in time. If we analyze the velocity registrations in time, the time stories are obviously different, though the statistical characteristics remain still. Therefore can assume this random phenomenon as a stationary one.

A phenomenon in which the statistical values do not change according with time passing, is called stationary phenomenon in the strict sense. It is not possible though to evaluate all the statistical value, so is never possible to verify if the process is stationary in the strict sense; analyzing a general random process, we define it stationary in the broad sense if:

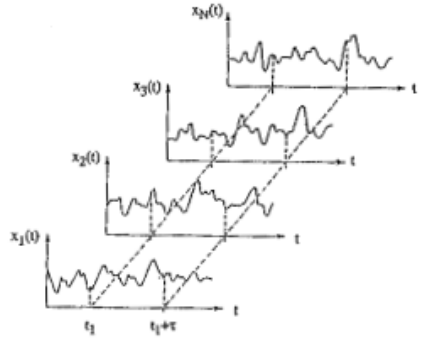

Figure 85 – Definition of random stationary and ergodic process

the mean value of the random process at a time t1:

$$\mu_x(t_1) = \lim_{N\to\infty} \frac{1}{N} \sum_{i=1}^{N} x_i(t_1)$$

The quadratic mean value (always at a time t1):

$$\Psi^2{}_x(t_1) = \lim_{N\to\infty} \frac{1}{N} \sum_{i=1}^{N} x_i{}^2(t_1)$$

The autocorrelation function is:

$$R_{xx}(t_1, \tau) = \lim_{N\to\infty} \frac{1}{N} \sum_{i=1}^{N} x_i(t_1) x_i(t_1 + \tau)$$

Analyzing a single random variable we only have one record xi(t) of a stationary process: in this case we will obviously valuate the stochastic quantity as the mean, whereas the correlation function through mean operations on the time story xi(t).

The same process is ergodic as well if the temporal mean, defined in the first part of this chapter, fit together with the formulas above. In this case one registration is enough in order to get the statistical values which define its characteristics.

The random values such as wind turbulence, are not stationary and ergodic. They are considered in such a way by defining the significant statistical values with a limited number of observations. In the practical applications, whenever the process is stationary it is usually taken as ergodic as well. In such a way is possible to define the statistical characteristic we need with a limited number or records.

10 Appendix B - PIV analysis

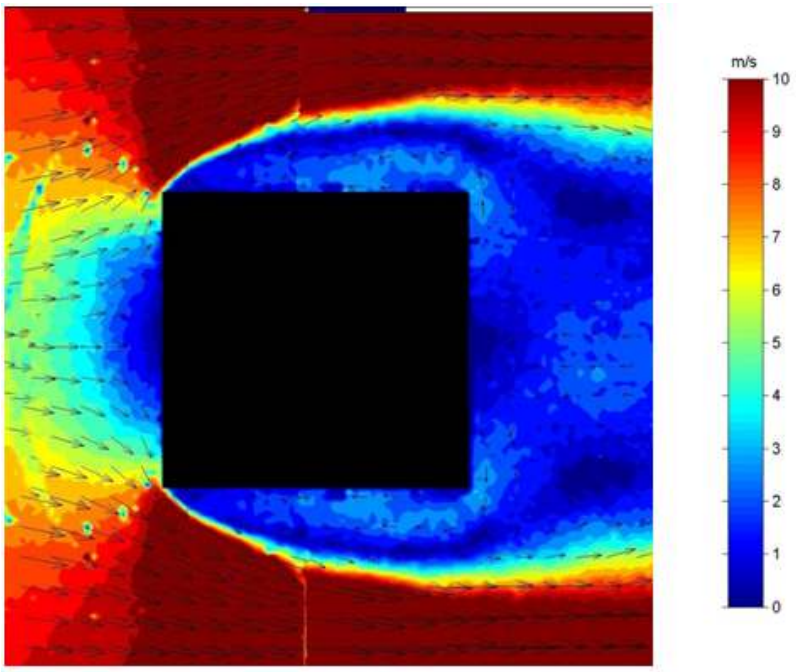

Figure 86 - 0° degrees

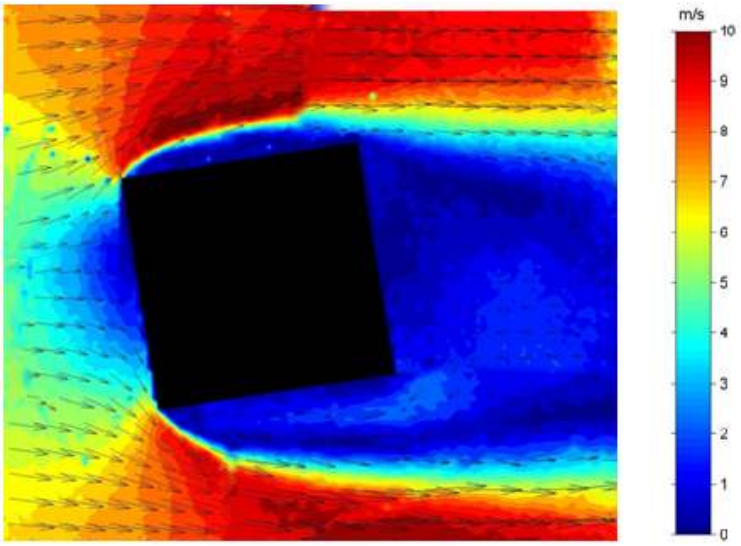

Figure 87 - 10° degrees

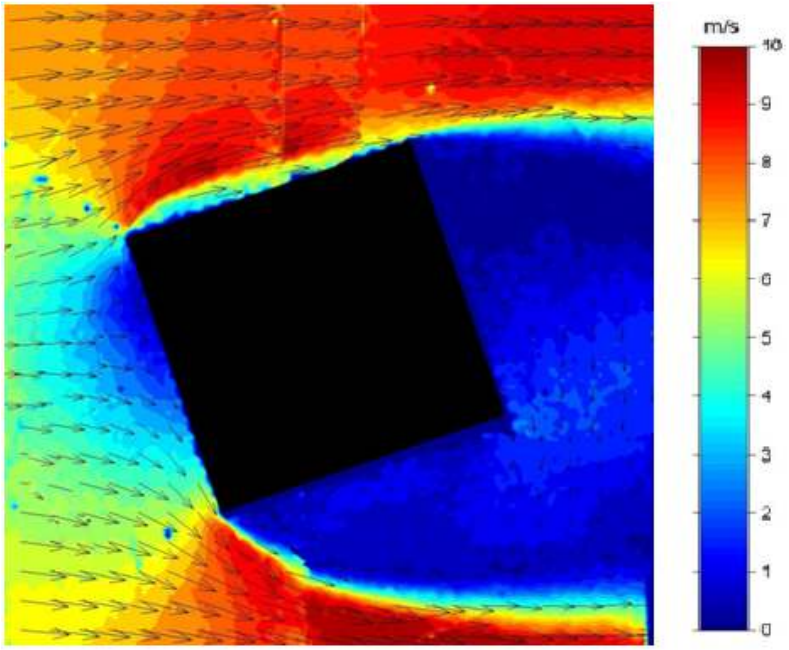

Figure 88 - 20° degrees

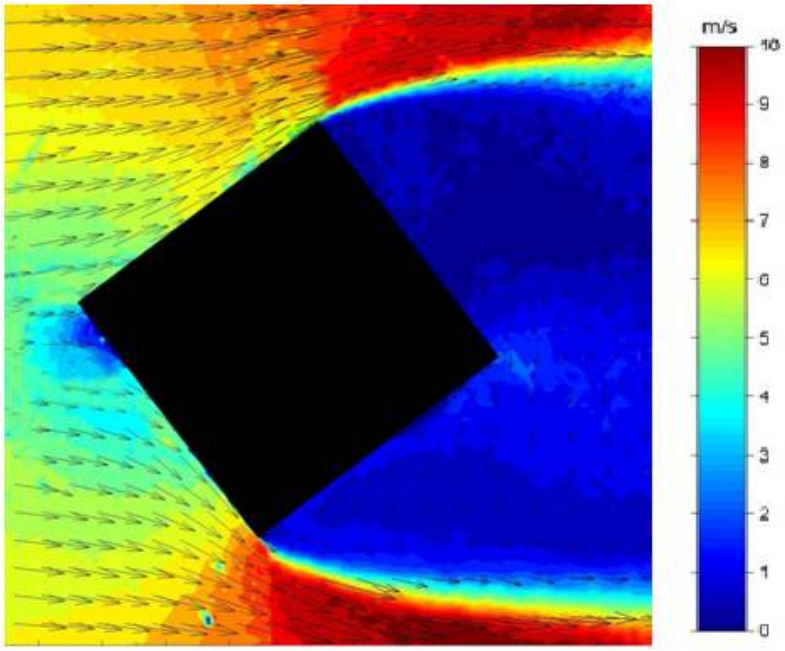

Figure 89 - 40° degrees

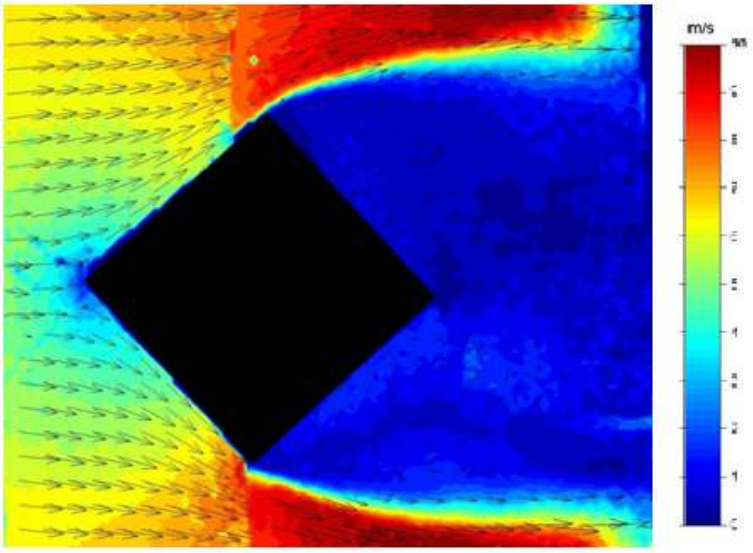

Figure 90 - 45° degrees

11 Appendix C

Mathcad program to be copied here.

Bibliography

Autore, titolo, pubblicato dove, quando

John D. Holmes , Wind Loading of Structure, 2001, reedited 2007

American Society ofCivil Engineers, 2005. Minimum Design Loads for Buildings and Other Structures. ASCE-7-05.